Identifying Key Structural Parameters for PET Foam Cores in Wind Turbine Blades Using Sandwich Failure Criteria and Non-Linear Buckling Analysis

Master's Thesis

Martin Kofod Christoffersen
Sander Fotland Tønnesen

Submitted: May 29th 2025

Design of Mechanical Systems

Aalborg University
Department of Materials and Production
Fibigerstræde 16, DK-9220 Aalborg

Title:

Identifying Key Structural Parameters for PET Foam Cores in Wind Turbine Blades Using Sandwich Failure Criteria and Non-Linear Buckling Analysis

Project:

Master's Thesis

Project period:

February 1st 2025 - May 30th 2025

ECTS:

30

Project group:

DMS4 - Group 3

Participants:

Martin Kofod Christoffersen
Sander Fotland Tønnesen

Supervisor:

Prof. Erik Lund (Aalborg University)

Contact Person:

Postdoc Sebastian M. Hermansen (Gurit)

Department of Materials and Production
Fibigerstræde 16
9220 Aalborg, Denmark

Martin Kofod Christoffersen

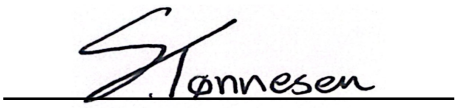

Sander Fotland Tønnesen

Report page count: 74
Appendix page count: 19
Date of submission: 29/05/2025

Summary

The increasing global demand for wind turbine blades (WTBs) has intensified the exploitation of balsa wood, a key core material sourced predominantly from the Amazon rainforest. In response, polyethylene terephthalate (PET) foam has emerged as a more sustainable alternative. PET foam has significantly lower stiffness and strength properties in the transverse direction compared to balsa wood, which results in an increased risk of instability and core failure in the sandwich structures. Therefore, incorporating PET foam as the core material in the sandwich structures of WTBs requires a complete redesign. This thesis contributes to the transition toward recyclable core materials by providing design-oriented insights for material developers such as Gurit.

A numerical analysis framework was developed to enable detailed structural assessment of PET foam in WTBs. The framework couples a non-linear buckling analysis created in ANSYS Parametric Design Language, first presented in [Tønnesen and Christoffersen, 2025], with a Fortran Post-Processing (FPP) routine for evaluating sandwich failure criteria, specifically face sheet wrinkling, shear crimping, and core failure. Moreover, the non-linear buckling analysis was extended to include laminate failure assessment and automatic analysis of multiple load cases. The buckling analysis utilizes a two-point approach wherein an eigenvalue problem based on linear perturbation is solved to detect global buckling after each load step. To capture local or stable post-buckling behavior, non-linearity factors are introduced. These factors are designed to detect non-linear behavior of elements, where the geometric non-linearity factors measure specifically non-linear bending. The constitutive modeling used to evaluate the sandwich failure criteria in FPP is based on First-Order Shear Deformation Theory (FSDT). FPP was verified against an analytical FSDT solution implemented into MATLAB, the commercial finite element tool Ansys Composite PrePost, and Aalborg University's in-house software MUlti Disciplinary Synthesis Tool. Five verification analyses were performed, comprising three different layups and four different load cases. FPP demonstrated strong agreement with the other analysis tools across the various load cases and laminate configurations.

A univariate parametric study was conducted on the full-scale Gurit98m WTB model under six representative load cases, consisting of two edgewise, flapwise, and mixed load cases. The effects of core thickness and the transverse shear moduli (G_{13} and G_{23}) were systematically evaluated. In the structural layup of the Gurit98m model, G_{13} is oriented along the blade in the spanwise direction, whereas G_{23} is along the hoopwise direction, around the cross-section. The Gurit98m model exhibited a substantial margin to buckling under the applied loading conditions. Consequently, little non-linearity was detected with the non-linearity factors across all configurations. Results show that the transverse shear modulus G_{13} has the most considerable impact on buckling and sandwich failure, while core thickness has a moderate effect, and G_{23} is largely inconsequential. These findings suggest that introducing anisotropy in the shear stiffness, specifically increasing G_{13} relative to G_{23}, could enhance structural performance, offering a promising direction for optimized PET foam development.

Preface

This document serves as the master's thesis for the Design of Mechanical Systems, Mechanical Engineering program at the Faculty of Engineering and Science at Aalborg University. The thesis aims to identify key structural parameters for replacing balsa wood with PET foam as core material in wind turbine blades, with composite failure criteria and non-linear buckling analysis. The research was conducted at Aalborg University from February 1^{st} to May 30^{th}, 2025.

Citations follow the Harvard method. In-text citations follow the format [Last name, Year], while section references are presented as [Last name, year, section]. References for figures and tables are provided within the respective captions.
All references are found in the bibliography, given before the appendices.

The nomenclature on the next page provides a non-exhaustive list of frequently used symbols and abbreviations. The report may introduce additional symbols. Indexing distinguishes symbols, e.g., X_n and X^n. The report uses punctuation (.) as a decimal separator. Vectors are indicated with { } and [ ] for matrices.

Tables and figures are sequentially numbered according to the corresponding chapter; for instance, 'Figure 3.2' indicates the second figure within Chapter 3.

An overview of the digital appendix can be found in Appendix A.

The generative artificial intelligence software ChatGPT has been utilized for more concise formulations and as a general *collaboration coach* in problem-solving [Sabzalieva and Valentini, 2023]. The artificial intelligence Grammarly has been used to support correct spelling, grammar, and sentence structure [Grammarly Inc.].

The authors would like to acknowledge the thesis supervisor, Professor Erik Lund, and Postdoc Sebastian M. Hermansen for their guidance and for facilitating the implementation of sandwich failure criteria into the Fortran-based post-processing routine.

Nomenclature

Abbreviations

AAU Aalborg University

APDL ANSYS Parametric Design Language

BC Boundary Condition

CFRP Carbon Fiber Reinforced Polymer

CLT Classical Laminate Theory

FEM Finite Element Method

FSDT First-order Shear Deformation Theory

GFRP Glass Fiber Reinforced Polymer

GNL Geometrically Non-Linear

LE Leading Edge

LS Load Step

NR Newton-Raphson

SGRE Siemens Gamesa Renewable Energy

TE Trailing Edge

TEP Total Elastic Potential

TN Truncation Number

UD Unidirectional

WTB Wind Turbine Blade

ACP ANSYS Composite PrePost

Material Properties

E_1	The Young's modulus in the stiffest direction	[Pa]

E_2	The Young's modulus perpendicular to the stiffest direction	[Pa]
E_3	Transverse Young's modulus	[Pa]
G_{12}	In-plane shear modulus	[Pa]
G_{13}	Transverse shear modulus	[Pa]
G_{23}	Transverse shear modulus	[Pa]
ν_{12}	In-plane Poisson's ratio	[-]
ν_{13}	Transverse Poisson's ratio	[-]
ν_{23}	Transverse Poisson's ratio	[-]
X	Lamina strength in material 1-direction	[Pa]
Y	Lamina strength in material 2-direction	[Pa]
e	Lamina strength (strain)	[−]

Linear & Non-linear Buckling

$[K_T]$	Global tangent stiffness matrix	[Pa]
$[K_0]$	Global initial stiffness matrix	[Pa]
$[K_\sigma]$	Global stress stiffness matrix	[Pa]
$\{D\}$	Global displacement vector	[m]
$\delta\{D\}$	Global incremental displacement vector	[m]
$\{F\}$	Global internal force vector	[N]
$\{R\}$	Global external force vector	[N]
λ_j	j$^{\text{th}}$ eigenvalue	[-]
$\{\phi\}_j$	j$^{\text{th}}$ mode shape	[-]

Non-linear Buckling Analysis

N_{max}	Total number of load steps	[-]
n	Current load step	[-]
n_{pert}	Current perturbation load step	[-]
i	Current sub-step	[-]
α^n	External load factor for load stepping	[-]
γ^n	Buckling load factor for load step n	[-]
ζ_{pert}	Perturbation load factor	[-]

η	External load factor for scaling $\{R\}$	[-]
$\{R\}^n$	Load at load step n	[N]
$\{R\}^n_{pert}$	Perturbation load at load step n_{pert}	[N]
$\{R\}^n_{buckling}$	Approximated buckling load at load step n_{pert}	[N]

Composite failure criteria

MUST	MUltidisciplinary Synthesis Tool
FPP	Fortran Post-Processing
FW	Face Sheet Wrinkling
SC	Shear Crimping
CF	Core Failure
RF	Reserve Factor
IRF	Inverse Reserve Factor
f	Failure Criterion Function
$[\hat{C}]$	Orthotropic stiffness matrix
$[\bar{C}]$	Transformed orthotropic stiffness matrix
$[T]$	Transformation matrix
ξ	Principal direction of maximum in-plane compression
ζ	Principal direction perpendicular to 12-plane (transverse direction)
η	Principal direction perpendicular to $\xi\zeta$-plane
θ_p	Principal angle

Contents

1 | Introduction

The primary function of a wind turbine is to convert the wind's kinetic energy into electrical power. This energy conversion is initiated by the Wind Turbine Blades (WTBs). Increasing the blade length is advantageous, as the power generated is proportional to the square of the rotor radius. As a result, WTBs are designed as weight-critical structures, where maximizing length while minimizing mass is essential. Due to their high specific bending stiffness and strength, sandwich structures with laminated composites are commonly employed to achieve high structural efficiency under these constraints. In WTBs, sandwich structures typically comprise Glass Fiber-Reinforced Polymer (GFRP) face sheets combined with lightweight core materials such as balsa wood or polymer foams.

The global demand for balsa wood has increased significantly in the last decade. In 2008, the global trade in sawn kiln-dried balsa wood was estimated to be worth USD$71 million [Midgley et al., 2010]. In 2020, the Asociación Ecuatoriana de Industriales de la Madera (AIMA) reported that Ecuador exported USD$ FOB 570 million worth of balsa wood [Zunino et al., 2022, p. 2]. This indicates an increase of over 703% in the global balsa wood trade. In 2022, Ecuador was responsible for around 90% of the exported balsa wood in the international market.

The substantial increase in demand for balsa wood can be primarily attributed to the wind energy industry. Specifically, the Chinese wind energy industry has experienced significant growth. In 2020 alone, the installed capacity of wind turbine blades increased by 60% in China [Zunino et al., 2022, p. 2]. Consequently, in 2022, China imported 50% of balsa wood in international trade. Moreover, the European market imported 20% in 2020. Denmark is the largest importer of balsa wood in Europe. In 2020 Denmark imported for USD$36 million representing a 95% increase since 2019 [Zunino et al., 2022, p. 2]. To meet the increased demand, Peru has been growing and exporting balsa wood to Ecuador since 2019. In 2022, Peru exported 40,000 $[m^3]$ to Ecuador, corresponding to 100% of the produced sawn balsa wood in Peru [Zunino et al., 2022, p. 3].

The regulatory bodies within the Peruvian government are not adequately equipped to handle the increased production of balsa wood. The government of Peru has focused on regulating the old-growth and high-value primary and natural forests. Figure 1.1 shows a steep increase in registered plantations with balsa wood in Peru's Amazon rainforest in 2021. The increase in plantations is suspected to be associated with operators registering balsa wood, which grows in secondary forests, as plantations rather than newly established industrial plantations [Zunino et al., 2022, p. 7]. Operators register balsa plantations as indigenous community land and private property. These types of plantations require less documentation compared with natural forests. Consequently, verifying the timber's legality is challenging for local law enforcement [Zunino et al., 2022, p. 10].

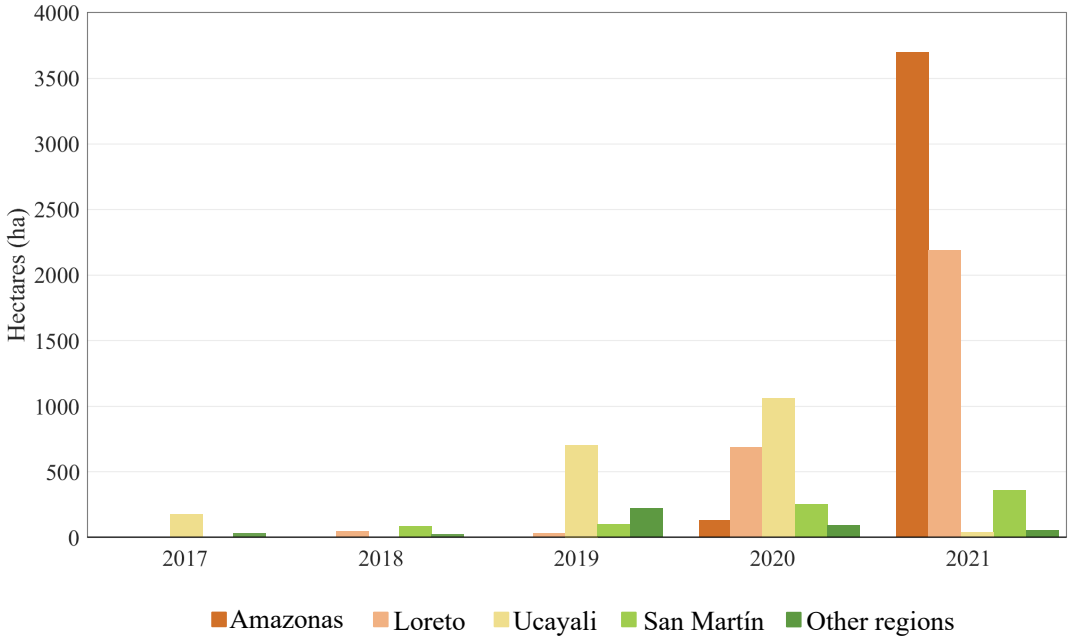

Figure 1.1: Hectares of balsa registered on plantations by region per year from 2017-2021. Data from and inspired by [Zunino et al., 2022, Fig. 1].

Ecuador and Peru have historically been associated with illegal logging. In 2006, the World Bank estimated that around 80% of Peru's and 70% of Ecuador's exported timber was of illegal origin [World Bank, p. 9]. In 2021, Peru is still associated with illegal logging, corruption, and land grabbing of indigenous territories in Peru's Amazon [Forest Trends, p. 1].

The socially and environmentally damaging deforestation of the Amazon rainforest in Ecuador and Peru does not align with the aim of the wind energy industry. In 2021, Vestas stated that they had significantly reduced the use of balsa wood in their wind turbine blades [Dalmases, 2021]. An alternative core material to balsa wood in the sandwich structures of wind turbine blades is Polyethylene terephthalate (PET) foam. LM Wind Power began implementing PET foam in their blades in 2014. In 2017, they produced their first 40+$[m]$ blade with full PET foam core instead of balsa wood [LM Wind Power]. PET foam is advantageous to balsa wood in terms of sustainability because it is a common thermoplastic that can be recycled. The wind energy industry is moving towards a circular economy in terms of material usage. This trend is evident in initiatives like DecomBlades and ZEBRA. DecomBlades aims to establish functional, sustainable value chains to handle end-of-life wind turbine blades. The latest news from DecomBlades comes from Siemens Gamesa Renewable Energy (SGRE), currently producing 115$[m]$ long WTBs with glass fiber from old WTBs. The blades will be installed in Ørsted's Greater Changhua 2b and 4 projects in Taiwan [Siemens Gamesa Renewable Energy, b]. Moreover, DecomBlades has developed the *Blade Material Passport* to support the circular value chain [DecomBlades]. The ZEBRA (Zero wastE Blade ReseArch) consortium, initiated in 2020, has produced two 100% thermoplastic blades of 62$[m]$ and 77$[m]$ [IRT Jules Verne, a,b,c]. The ZEBRA project demonstrated a closed-loop recycling process for thermoplastic wind turbine blades [Arkema].

The Chinese company SANY Renewable Energy holds the record for the longest wind turbine blade. The company launched the 131$[m]$ SY1310A on-shore WTB in 2024 [SANY Renewable Energy]. Vestas has produced the longest blade on the European market, closely followed by SGRE, with 115.5$[m]$ and 115$[m]$, respectively [Vestas][Siemens Gamesa Renewable Energy, a]. Advancements must be made to achieve 100% recyclable wind turbine blades made with thermoplastics at the current size, 130+$[m]$.

In pursuit of these advancements, Gurit has proposed a project. Gurit is a leading supplier of composite materials, kitting services, and manufacturing solutions for the global wind energy industry [Gurit, g]. The project is motivated by replacing balsa wood with sustainable PET foam recycled from plastic bottles. The project aims to highlight important considerations and key material parameters when replacing balsa wood with PET foam as the core material in state-of-the-art offshore WTBs.

The primary function of the face sheets in sandwich structures is to provide in-plane stiffness and strength, whereas the core material should carry the out-of-plane forces. The immediate challenge in replacing balsa wood with PET foam is the substantially decreased transverse stiffness properties. Table 1.1 presents an overview of the essential stiffness properties of balsa wood and PET foam used as core material in WTBs. Specifically, Balsaflex and Kerdyn from Gurit are presented [Gurit, d,e].

	$\rho\ [kg/m^3]$	$E_3[MPa]$	$G_{13}[MPa]$	$G_{23}[MPa]$
Balsaflex 150	155	3518	163	163
Kerdyn 150	150	142	43	39

Table 1.1: Essential material properties of Balsaflex and Kerdyn PET foam from Gurit [Gurit, d,e].

Here, ρ is the nominal density, and the subscripts are related to the directions in Figure 1.2. Notice that the 3-direction is in the negative transverse direction, i.e., E_3 is the compressive transverse modulus [Gurit, d].

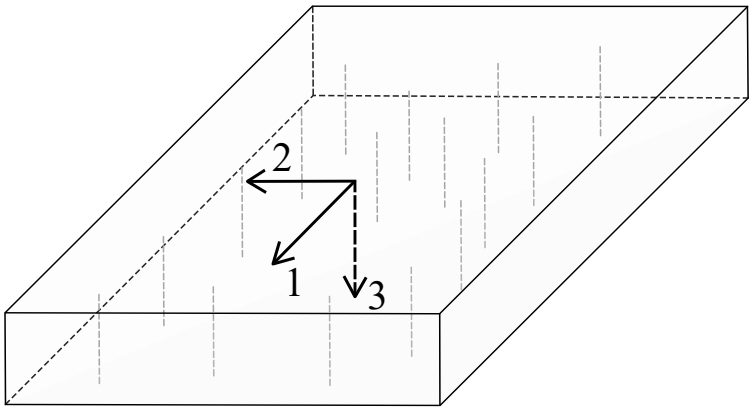

Figure 1.2: Material coordinate system for core material. Grey dashed lines indicate the cellulose fibers in balsaflex [Gurit, d].

Replacing the balsa wood core with PET foam will necessitate a complete redesign of wind turbine blades. Structural optimization is a key tool for accelerating the design process. However, identifying key parameters and accurately assessing failure is necessary before an efficient optimization scheme can be developed. One approach for identifying key parameters is to perform a parametric study. In a parametric study, several parameters are investigated by varying one parameter while keeping others fixed. Because only one parameter is varied at a time, a parametric study will not necessarily give an optimum design, but rather an indication of the effect of each parameter. However, creating a detailed, parameterized WTB model and implementing it in a structural optimization problem is a substantial and time-consuming task, especially when including constraints such as sandwich failure criteria. A parameter study will assess the effectiveness of implementing the model in a full-scale optimization scheme in a more time-efficient manner. The effect of varying a parameter can be quantified in several ways, such as cost, weight, or manufacturing time. However, the feasibility of replacing the core material must first be investigated in terms of its structural integrity. Therefore, the effects of varying

parameters must be measured in terms of values related to structural integrity, such as a failure index or buckling load factor.

Sandwich structures have multiple failure modes and mechanisms depending on loading, geometry, and layup [Zenkert, 2005]. The typical failure modes affected by the core of sandwich panels in WTBs are related to transverse stress and stability: core failure, face sheet wrinkling, shear crimping, and general buckling [Gurit, f, p. 9]. Changing the core material will affect the stress distribution in the WTB. Consequently, failure must also be assessed for the laminates throughout the WTB. Gurit has provided a 98$[m]$ WTB model named Gurit98m. This parameterized open-source model, created for optimization purposes, will act as a representative wind turbine blade model throughout the report.

To accurately assess the effect of replacing balsa wood with PET foam, the analysis must include non-linear effects. Therefore, the non-linear buckling analysis based on linear perturbation presented in [Tønnesen and Christoffersen, 2025] will be expanded to analyze the response of the Gurit98m wind turbine blade model. Moreover, both sandwich and laminate failure criteria must be incorporated into the analysis method to accurately predict composite failure. This leads to the following problem statement:

How can composite failure criteria be implemented to accompany a non-linear buckling analysis in identifying the key structural parameters relevant to replace balsa wood with PET foam as the core material in Gurit98m?

2 | Theory

A thorough theoretical foundation is required to support the structural evaluation and material substitution investigated in this thesis. The chapter begins with an overview of structural and material layout in WTBs. Fundamental principles and computational methods of buckling in composite structures are presented, with particular emphasis on geometrically non-linear buckling. Subsequently, failure modes relevant to sandwich structures are introduced, including face fracture, face wrinkling, shear crimping, core failure, and the corresponding failure criteria. These theoretical insights provide the foundation for implementing and verifying the failure criteria applied in this study and for understanding the results of the subsequent parametric study.

2.1 Structural Layout of Wind Turbine Blades

WTBs are designed with a trade-off between aerodynamic efficiency, weight, cost, and structural integrity, specifically stiffness and strength [Hansen, 2000]. The cross-section of a wind turbine blade typically resembles an airfoil, utilizing this shape to generate lift. When the wind meets the front of the blade, known as the leading edge (LE), the wind is separated and flows along the top and bottom surfaces of the WTB. The upper surface, the suction side, creates a low-pressure zone that pulls the blade. As air travels along the bottom of the blade, known as the pressure side, a high-pressure zone is created that essentially pushes the blade, generating lift. The back end of the blade is referred to as the trailing edge (TE) [Hansen, 2000, p. 14]. The chord is used as a reference to describe the cross-sectional directions. The chord is a straight line that connects the leading and trailing edges. The direction along the chord is called edgewise, and the perpendicular direction is called flapwise. The cross-sectional thickness of a WTB is the flapwise distance between the suction and pressure side surfaces. The cross-sectional directions of WTBs are visualized in Figure 2.1.

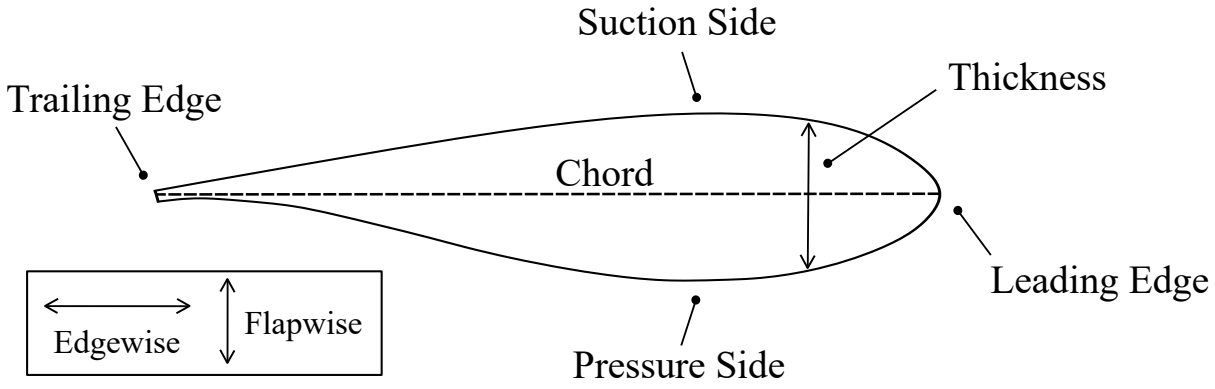

Figure 2.1: Cross-section of a typical wind turbine blade.

Although an optimum aerodynamic shape may provide maximum lift, such designs do not offer the structural integrity required to withstand the large forces experienced by WTBs. WTBs are designed as thin-walled hollow structures to maintain structural integrity while minimizing weight. A generic cross-section of a WTB is provided in Figure 2.2.

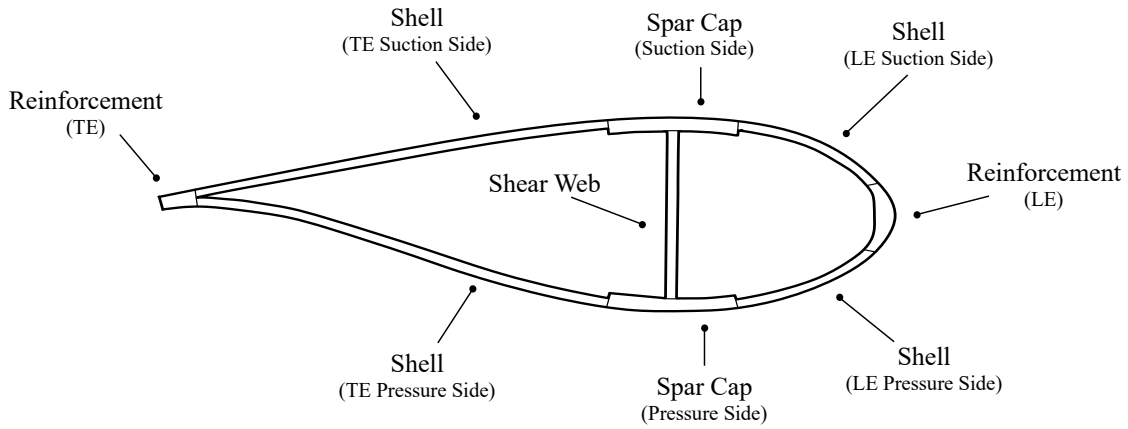

Figure 2.2: Generic WTB cross-section, shape inspired by the cross-sectional shape of the Gurit98m blade 50 [m] from the root.

The primary function of the spar caps is to carry the large tensile and compressive stresses caused by the flapwise bending moments. To enhance flapwise bending stiffness and strength, the spar caps are kept at a distance from each other by the shear web. The flapwise shear loads are carried mainly by the shear web, oriented perpendicular to the cord. Moreover, the shear web divides the cross-section, lowering the risk of buckling failure in the shells and spar caps. Only one shear web is included in Figure 2.2, inspired by a generic blade from SGRE. This design features a single shear web, made possible by their patented IntegralBlade® technology [Jensen, 2022]. The main purpose of the shells is to provide a closed structure and facilitate an aerodynamic shape [Gurit, b]. The shells also contribute to resisting torsional loads, transferring shear loads, stiffening and strengthening the spar caps, and providing some resistance to edgewise bending. Increasing the chord length increases the area of the shells, thereby increasing the moment of inertia with respect to edgewise loading [Overgaard et al., 2010a, p. 1106]. The trailing and leading edges typically feature reinforcements, as shown in Figure 2.2, to resist edgewise bending moment. Without TE and LE reinforcements, the shells would need to be considerably thicker, increasing both weight and cost. An illustration of a full WTB is provided in Figure 2.3.

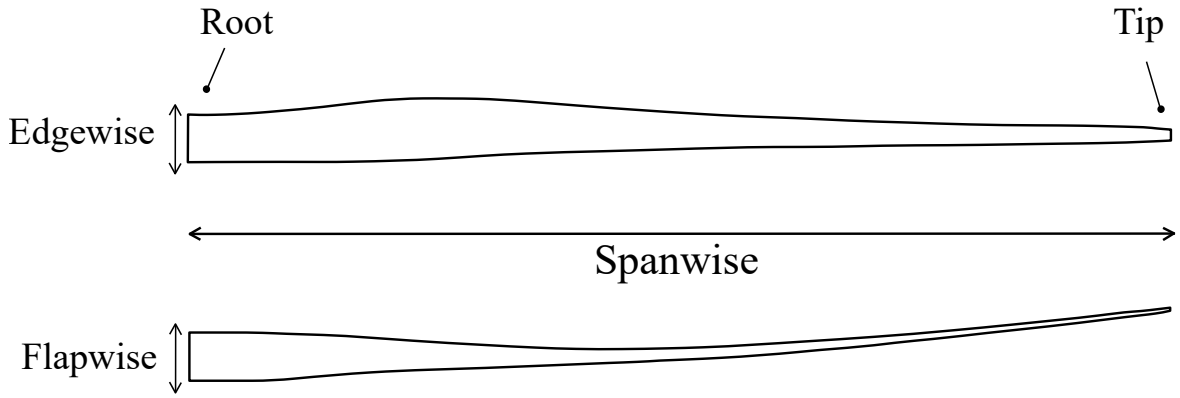

Figure 2.3: Full blade based on the Gurit98m model.

The direction along the length of the WTB is referred to as spanwise. Large edgewise- and flapwise bending moments originate from multiple sources, where the most significant arise from gravitational loading and the wind, respectively. As a result, structural integrity is more critical than aerodynamic efficiency at the root. Consequently, the cross-sectional and material thicknesses, chord length, and airfoil vary along the length of the blade [Gurit, a]. Prebend is a common feature in wind turbine blades, where the blade is molded with a bend outward from the tower, i.e., toward the pressure side. This increases the clearance between the tip and the tower, reducing the impact risk while allowing for greater flapwise deformation. As a result, the spar caps do not need to be as stiff, reducing material usage. However, too much prebend will induce unwanted torsional forces caused by edgewise loading. For this reason, finding the correct balance between prebend and stiffness is a delicate task.

2.1.1 Materials

Wind turbine blades are made from various materials based on factors such as stiffness, weight, strength, fatigue properties, and cost. Composite materials can be tailored for specific physical and chemical properties. The composite structures used in wind turbine blades are laminates and sandwich structures. A schematic overview of composite laminates and sandwich structures is provided in Figure 2.4.

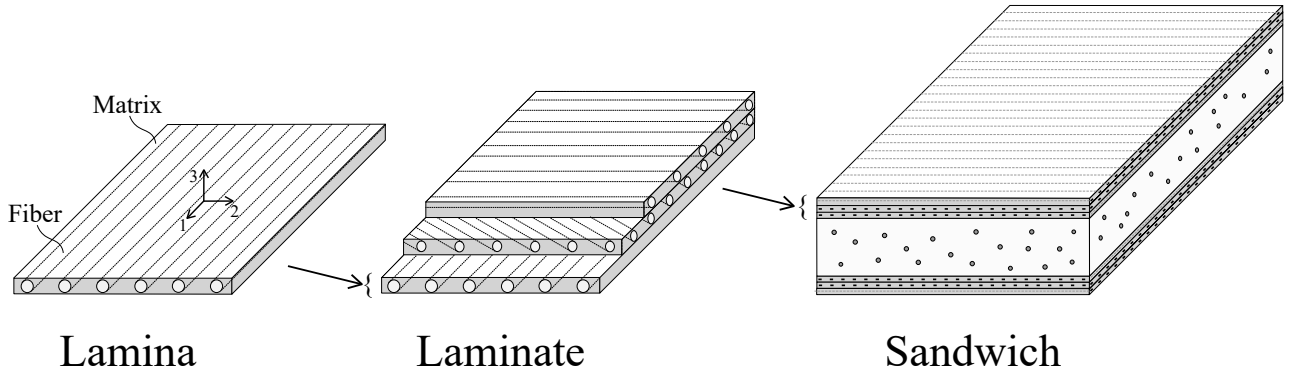

Figure 2.4: Lamina, laminate, and sandwich structure. The figure is inspired by Figure 2.6 in [Kettner, 2020].

The laminates used for wind turbine blades are created from Fiber-Reinforced Polymer (FRP) lamina and bonded sequentially to achieve the desired material properties. The fibers, made from materials with high tensile strength and modulus of elasticity, provide high in-plane strength and stiffness along the fibers [Gurit, h, p. 4]. The matrix binds the fibers, distributes loads, and is the dominant factor in through-the-thickness and transverse shear material properties. Additionally, the matrix has considerable influence on impact resistance and fracture toughness. The fibers are significantly stiffer and stronger than the matrix, so the resulting composite laminate is orthotropic in the material coordinate system. The 1−direction in Figure 2.4 denotes the stiffest direction in the material coordinate system. The 2−direction is the in-plane direction perpendicular to the 1−direction, and 3 represents the transverse direction, or out-of-plane. The most common lamina types in WTBs contain uniaxial, biaxial, and triaxial fibers. Depending on the sequence and orientation of the bonded lamina, couplings such as bending-extension, shear-extension, and bending-twist may be induced.

Carbon Fiber Reinforced Polymer (CFRP) and GFRP are the most common laminates used for WTBs [Gurit, h, p. 4]. These laminates utilize the high specific strength and stiffness of carbon and glass fibers, combined with a polymer-based matrix that offers good environmental resistance. CFRP is approximately three times stiffer, twice as strong, and 25% less dense than GFRP [Gurit, b, p. 10]. However, CFRP is approximately 5 times more expensive than GFRP, which limits its use for the spar

caps. There are several methods for describing laminate behavior, such as the Equivalent Single Layer (ESL) theories like the First Order Shear Deformation Theory (FSDT), which is used to formulate the shell elements in ANSYS [ANSYS, 2024c, p. 684].

Sandwich structures are low-weight composite structures with high bending strength and stiffness. Sandwich structures are created of two high-strength and high-stiffness face sheets, separated by a lightweight core. The core's primary function is to separate the face sheets while carrying transverse shear and through-the-thickness loads. Therefore, the core material should exhibit high transverse shear modulus and compressive stiffness and strength. A low-density material is used for the core to minimize the weight of the sandwich structure. The primary function of the face sheets is to provide in-plane stiffness, important for carrying the loads arising from bending, transverse shear, and torsion [Lund et al., 2024]. Additionally, the face sheets should provide environmental and impact resistance. Therefore, the face sheets are made from materials featuring high in-plane stiffness, strength, and impact resistance. Consequently, sandwich structures exhibit excellent bending stiffness and resistance to buckling failure. Classical Sandwich Theory (CST) can describe the behavior of sandwich structures, combining the assumptions of Classical Laminated Theory (CLT) and FSDT. A schematic overview of a WTB cross-section with different composite material types is provided in Figure 2.5.

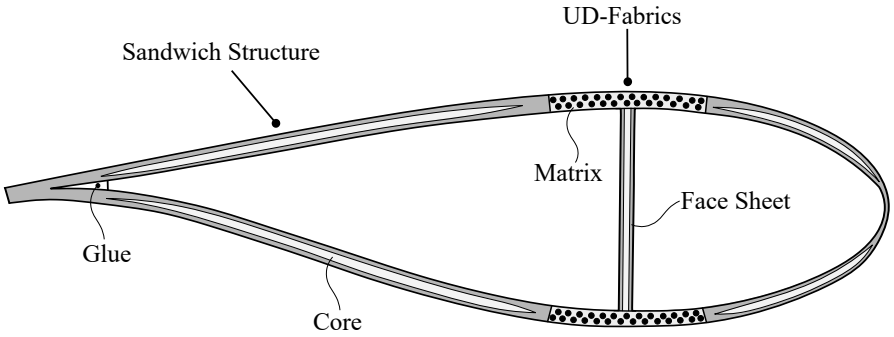

Figure 2.5: WTB cross-section material layup. This figure is representative, and the distribution of components is described for illustrative purposes only. Figure inspired [Hermansen et al., 2025].

The spar caps are primarily made from unidirectional (UD) fabrics, oriented along the spanwise direction [Gurit, b, p. 15]. This orientation is chosen because the spar caps are primarily loaded in flapwise bending. Typically, the spar caps also feature biaxial fibers, oriented $\pm 45°$ to the spanwise direction, incorporated with *Non-Crimp Fabrics* (NCFs). NCFs consist of UD fiber mats layered in different directions, stitched together before infusion, where the fibers are free of crimps. NCFs range from unidirectional to biaxial and multiaxial fabrics. Biaxial fibers help prevent through-thickness fracture, as the biaxial fibers assist the matrix in carrying in-plane loads perpendicular to the primary flapwise loading direction. Moreover, incorporating biaxial fibers helps reduce void content in the spar caps [Gurit, b,c]. The shear web contains biaxial fibers in the face sheets to provide in-plane shear stiffness. The shells have a high content of biaxial fibers, oriented diagonally to the spanwise direction for increased shear stiffness [Gurit, b]. This provides resistance towards torsional loading. Moreover, the shells have fibers along the spanwise direction to provide edgewise bending stiffness and strength. Parts of the shells are created as sandwich constructions to increase bending stiffness without adding much additional weight. This helps preserve the airfoil and enhance buckling resistance. The primary face sheet material used for the shells and the shear web is GFRP. Balsa wood and low-density rigid foam are the most commonly used core materials in WTBs [Gurit, c]. According to the Materials Passport, the cores used in the Vestas V47 and LM 37.3 P2 blades include balsa wood and polyvinyl chloride (PVC) foam [DecomBlades].

Balsa wood is transversely isotropic, with higher stiffness and strength oriented along the growth direction, corresponding to the direction of the cellulose fibers. Compared to polymer foam cores, balsa wood exhibits superior mechanical properties at an equivalent core density [Lund et al., 2024, Prt. 9,p. 20]. The balsa wood is cut into cubes and bonded together, with the fibers oriented perpendicular to the face sheets. This configuration is called end-grain balsa [Gurit, h, p. 44]. This helps mitigate issues with humidity, as water primarily spreads along the fibers. This is important, as the mechanical properties of balsa wood are significantly weakened when exposed to moisture [Lund et al., 2024].

A key benefit of using cellular polymer foam cores is that they are available in various densities and can be easily and cost-effectively manufactured. An increased interest in PET foam as a core material in WTBs is driven by its environmental sustainability and recyclability. PVC foam generally exhibits better mechanical properties than PET foam [Gurit, f, p. 3]. However, PVC is not recyclable, whereas PET is up to 100 % recyclable [Gurit, f].

2.2 Buckling

Thin-walled composite structures like wind turbine blades are prone to buckling failure. In [Overgaard and Lund, 2010, Overgaard et al., 2010a,b] a full-scale flapwise bending test was conducted on a 25$[m]$ WTB. The outcome of the test was a methodology for structural analysis of composite wind turbine blades under geometric and material-induced instabilities. The numerical framework included progressive interlaminar damage models within the geometrically non-linear finite element method. The aforementioned approach showed excellent results. The point of failure on the WTB was determined to be in a corner of the main spar near the root end. Comparison between the numerically determined point of failure and evolution of delamination matches well with the experimental results. The authors concluded that geometric instability is the initiating phenomenon of the delamination leading to complete structural collapse [Overgaard et al., 2010a, p. 1108]. The developed non-linear buckling method in [Tønnesen and Christoffersen, 2025] essentially detects the onset of failure by detecting geometric instabilities.

2.2.1 Definitions & Classification

Typically, buckling refers to a structure changing from a stable to an unstable configuration, like the classical axially loaded column. In [Jones, 2006], the definition of the *buckling load* is twofold. Firstly, it is defined as the load at which a structure changes from a stable to an unstable configuration. Secondly, it is the load at which a structure changes from its previous stable configuration to another stable configuration. The change of configuration may or may not be associated with large deformation or deflection [Jones, 2006, p. 5]. The buckling load may also be defined as the largest load for which stability of equilibrium of a structure exists in its fundamental equilibrium configuration [Lindgaard and Lund, 2011b, p. 1]. The two definitions have the same meaning, however, the second definition is a more general statement. The *configuration* of a structure refers to the geometric description of the material points that constitute the structure. In the context of FEM, the configuration of the structure is defined with the mesh. The *fundamental equilibrium path* is the kinematically admissible displacements and loading parameter, fulfilling stationarity of the total elastic potential $\delta\Pi(D_i,\Lambda) = 0$, from zero loading $\Lambda = 0$ and zero displacements $D_i = 0$ [Thompson and Hunt, 1973, p. 50].

A structure in a *stable* configuration will, under a small disturbance δD_i, always return to its original state after the disturbance. The deflection associated with the disturbance is also small [Jones, 2006, p. 2]. For a structure in an *unstable* configuration, a small disturbance results in a sudden change in deformation mode or a large deflection value without returning to its original configuration [Jones, 2006, p. 3]. The stability definition given in [Jones, 2006] can be related to the total elastic potential via the Lagrange-Dirichlet theorem [Bazant and Cedolin, 1991, Sec. 3.6]. The theorem states that the

equilibrium of a discrete, conservative mechanical system is stable if Π assumes a strict local minimum at this equilibrium [Bazant and Cedolin, 1991, p. 178]. A strict minimum of the total elastic potential is defined in terms of variations in the displacement field δD_i:

$$\Delta\Pi = \Pi(D_i + \delta D_i, \Lambda) - \Pi(D_i, \Lambda) > 0 \quad \textit{for all} \quad \delta D_i \neq 0 \tag{2.1}$$

A strict minimum of Π requires the tangent stiffness matrix, i.e., the second derivative, to be positive definite [Lindgaard, 2024, p. 75]. Positive definiteness of the tangent stiffness matrix $[K_T]$ can be decided using different methods, e.g., the eigenvalues, the determinant, or the eigenvectors. Figure 2.6 gives a visual representation of the buckling classifications.

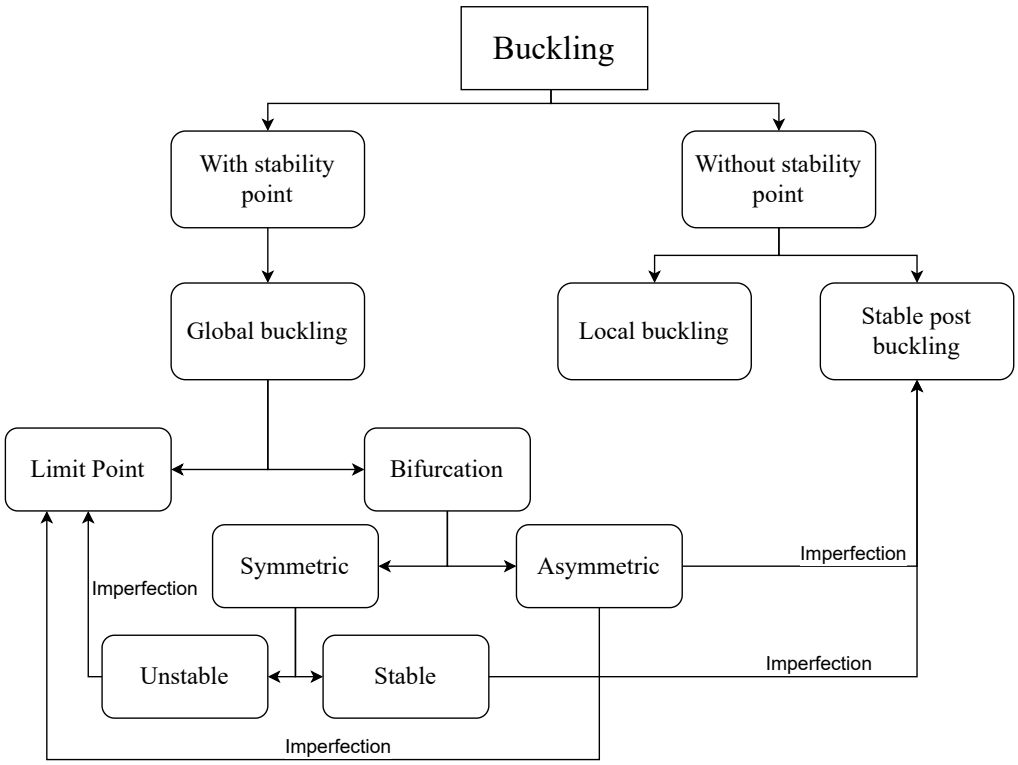

Figure 2.6: Classification of buckling behavior. Inspired by [Tønnesen and Christoffersen, 2025, p. 9] and [Lindgaard and Lund, 2011b, Fig. 1].

When a buckling load is present on the fundamental equilibrium curve of a structure, it is classified as buckling with a *stability point*. If the fundamental equilibrium curve reaches an extremum, the extremum point is referred to as the *limit point* [Cook et al., 2002, p. 642]. If a secondary equilibrium curve crosses the fundamental equilibrium curve, the point of intersection is the *bifurcation* point [Lindgaard and Lund, 2011b]. The subcategories under bifurcation buckling refer to the form of Π of the structure at the bifurcation point. If Π has an inflection point at the bifurcation point, the bifurcation buckling is asymmetric and the stability is directionally dependent like a ball on a saddle point [Jones, 2006, p. 21]. If Π only has one extremum, the bifurcation point is symmetric. Furthermore, the bifurcation buckling is stable if the extremum is a minimum. Conversely, if the extremum is a maximum, the bifurcation is unstable [Thompson and Hunt, 1973, p. 51-57]. The different types of buckling are illustrated in Figure 2.7. The classification of the type of bifurcation buckling is based on higher-order derivatives of Π [Thompson and Hunt, 1973, p. 130]. These derivatives are not readily available in FEM as a consequence of the shape functions. The stability of a bifurcation point can be analyzed considering imperfection sensitivity and using small load steps as shown in [Lindgaard and Lund, 2011a, Ch. 4].

The definition of buckling without a stability point is inspired by [Lindgaard and Lund, 2011b, p. 2]. In this study, buckling with no stability point includes imperfect structures with originally stable bifurcation, i.e., stable post-buckling, and structures with local buckling without bifurcation or limit point behavior. According to [Thompson and Hunt, 1973, p. 68], buckling of a stable post-buckling structure is indicated by a rapidly increasing deflection as the buckling load of the perfect structure is approached. When analyzing stiffened structures, such as WTBs, local buckling can be defined as the instability of panels between stiffeners. Whereas global buckling involves buckling of the panels and the reinforcing members [Singer et al., 2002, p. 955].

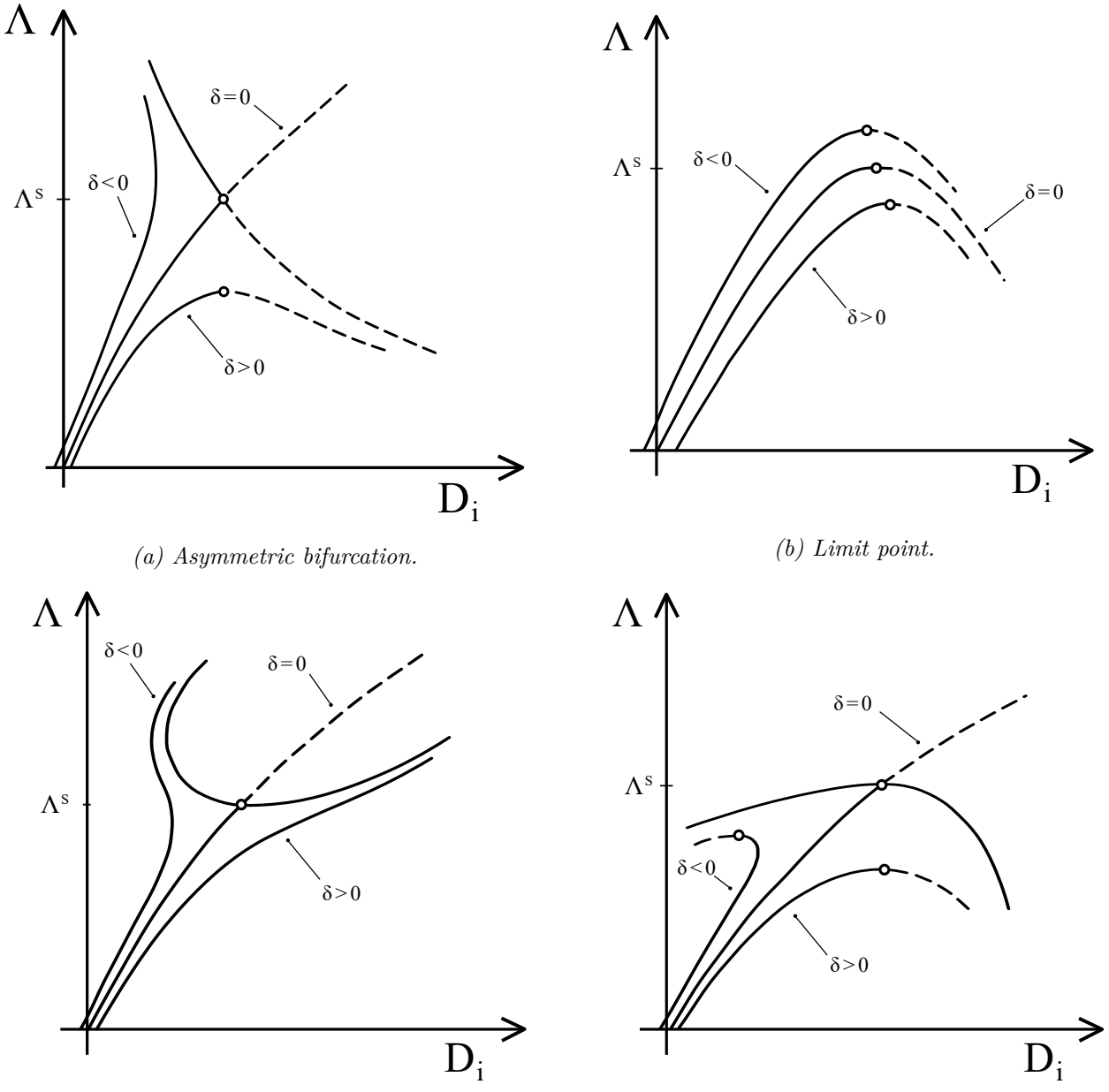

(a) Asymmetric bifurcation.

(b) Limit point.

(c) Stable symmetric bifurcation.

(d) Unstable symmetric bifurcation.

Figure 2.7: Overview of different buckling behavior for perfect and imperfect systems. Inspiration from [Thompson and Hunt, 1973, p. 66-67]. The solid lines represent stable equilibrium paths, whereas the dashed lines are unstable. δ denotes imperfection, "$\circ$" is stability points, D_i is a set of generalized coordinates, and Λ is a loading parameter.

In general, imperfections can be attributed to geometry, material, or loading conditions. An imperfect structure will never experience bifurcation buckling. Instead, the buckling behavior will be a limit point or with no stability point [Lindgaard and Lund, 2011b]. The effect of imperfections is illustrated in Figure 2.6. In the framework of FEM, the typical method of incorporating geometrical imperfection is to perturb the nodes in the lowest mode shape of a linear buckling analysis by some fraction of the thickness [Lindgaard et al., 2010].

2.2.2 Buckling of Composite Structures

Composite structures necessitate additional considerations compared with structures made from isotropic material when classifying their buckling behavior [Singer et al., 2002, p. 1053]. Depending on the layup, composite materials experience elastic coupling, as is evident in the so-called ABD-matrix of the FSDT. As stated in [Cook et al., 2002, p. 639], bifurcation buckling occurs when membrane strain energy is converted to bending strain energy with no change in externally applied loading. This alternative definition of bifurcation buckling indicates that the coupling between membrane and bending deformation in the constitutive relation of the composite material acts as an imperfection. Therefore, composite structures with elastic coupling may not exhibit bifurcation buckling. Even small elastic couplings may have a significant effect on the buckling behavior of composite plates [Singer et al., 2002, p. 1058]. Considering a stiffened composite structure, such as a wind turbine blade, the cross-sectional stiffness typically exhibits many couplings. The coupling is evident by the need for tools like BECAS (BEam Cross section Analysis Software) from the Technical University of Denmark [BECAS], which utilizes anisotropic beam theory to account for all stiffness terms [Blasques and Stolpe, 2012, Giavotto et al., 1983]. BECAS is used both in the wind energy industry and within academia. Like the material-induced coupling between membrane and bending deformation, this geometry-based coupling acts as an imperfection and eliminates the bifurcation behavior of a full-scale wind turbine blade.

2.2.3 Computational Methods

The computational methods presented here are within the framework of the finite element method. The fundamental equation for determining the stability point of a structure stems from the fact that the tangent stiffness matrix stops being positive definite and becomes singular at the stability point [Bathe, 1996, p. 632]:

$$[K_T]^s\{\phi\}_j = \{0\} \tag{2.2}$$

Here, $[K_T]$ is the global tangent stiffness matrix where the superscript s refers to the structure being at the stability point and $\{\phi\}_j$ is the j^{th} mode shape. The *mode shape* is the deformation mode of the structure at the stability point. The mode shape only contains information about the relative magnitude of deformation. Depending on the assumptions valid for a problem, different approximations for the global tangent stiffness matrix at the stability point can be used. For structures like wind turbine blades, substantial geometrically non-linear (GNL) effects are present [Tønnesen and Christoffersen, 2025]. Therefore, a non-linear buckling analysis should be used.

Non-linear Buckling Analysis

To avoid performing a direct singularity check of the tangent stiffness matrix, the tangent stiffness matrix at the stability point can be approximated by linear extrapolation based on tangent information from a previously converged load step. The tangent information can be based on a single converged point or two, i.e., the one-point or two-point approach [Lindgaard and Lund, 2010]. Structural analysis is performed in the commercial software ANSYS [ANSYS, b]. ANSYS implements the two-point approach through a linear perturbation procedure [ANSYS, 2024e, Sec. 15.8.5]. The two-point approach is derived based on the procedure in [Bathe, 1996, Sec. 6.8.2]. The global tangent stiffness matrix at the stability point is approximated by linearly extrapolating the change in $[K_T]$ between any two

load steps prior to buckling $(n-1,i)$ and (n,i).

$$[K_T]^s \approx [K_T]^{(n-1,i)} + \lambda_j \left([K_T]^{(n,i)} - [K_T]^{(n-1,i)} \right) \tag{2.3}$$

The global external force vector at the stability point is approximated in the same manner:

$$\{R\}^s \approx \{R\}^{(n-1,i)} + \lambda_j \left(\{R\}^{(n,i)} - \{R\}^{(n-1,i)} \right) \tag{2.4}$$

Substituting equation (2.3) into equation (2.2) results in the eigenvalue problem:

$$[K_T]^{(n-1,i)} \{\phi\}_j = -\lambda_j \left([K_T]^{(n,i)} - [K_T]^{(n-1,i)} \right) \{\phi\}_j \tag{2.5}$$

λ_j is the eigenvalue of the problem, with the subscript j indicating different eigenvalues. The eigenvalues are sorted in ascending order, with λ_1 being the smallest eigenvalue. In the framework of FEM, one eigenvalue is available for every degree of freedom of the model. The two-point procedure is valid for any load steps prior to buckling, and linearity is assumed from load step $(n-1,i)$ onward.

The eigenvalue buckling analysis based on linear perturbation in ANSYS has three parts, *Base Analysis*, *Phase 1*, and *Phase 2*. During the base analysis, the incremental equilibrium equations (2.6) are solved. The incremental equilibrium equations of a GNL analysis are formulated with the Updated Lagrangian (UL) formulation in ANSYS [ANSYS, 2024e, p. 50]. In the UL formulation, geometric non-linearity is formulated based on the previous converged configuration rather than the original state of the structure [Bathe, 1996, p. 542]. The incremental equilibrium equations for a UL formulation are:

$$[K_T]^{(n-1,i)} \delta\{D\}^{(n-1,i)} = \{R\}^{(n,i)} - \{F\}^{(n-1,i)} \tag{2.6a}$$

$$[K_T]^{(n-1,i)} = [K_0]^{(n-1,i)} + [K_\sigma]^{(n-1,i)} \tag{2.6b}$$

The solution is known at load step $n-1$ and sought in load step n. The superscript i refers to a substep in a Newton-Raphson (NR) sense. $\delta\{D\}$ is the global incremental displacement vector, $\{R\}$ is the global external force vector, $\{F\}$ is the global internal force vector, $[K_0]$ is the global initial stiffness matrix, and $[K_\sigma]$ is the global stress stiffness matrix. Because this is a UL formulation, $[K_0]$ relates to the previous converged configuration of the structure and includes displacement dependencies. For a UL formulation with large strains, large rotation, and large displacement capabilities, Cauchy stress and logarithmic strain are used as the stress and strain measures [Bathe, 1996, p. 486] [ANSYS, 2024e, p. 35].

Phase 1 of the procedure is the linear perturbation analysis. Because the base analysis is converged at load step (n,i), the perturbation load step is (n_{pert},i). The perturbation load step is different from other load steps because it does not necessarily converge to the same point of the equilibrium path as the non-linear equilibrium equations. A perturbation load step approximates the displacements by solving the linear system of equations, see equation (2.8) [ANSYS, 2024d, p. 336]. Only $[K_\sigma]$ in equation (2.6b) is assumed to change between load step (n,i) and (n_{pert},i), while $[K_0]$ is assumed to remain unchanged. This assumption is reasonable if the perturbation step is small, specifically if the displacement-dependent stiffness terms in $[K_0]$ are unchanged. Consequently, the change in $[K_T]$ from load step (n,i) to (n_{pert},i) is approximated as the global perturbed stress-stiffness matrix:

$$[K_\sigma]_{pert}^{(n,i)} \approx [K_T]^{(n_{pert},i)} - [K_T]^{(n,i)} \tag{2.7}$$

The global perturbed stress-stiffness matrix $[K_\sigma]_{pert}^{(n,i)}$ is calculated from the perturbed displacements. The perturbed displacements $\{D\}_{pert}^{(n,i)}$ are calculated by applying an additional load increment to the structure as a perturbation load $\{R\}_{pert}^{(n,i)}$ and solving the static equilibrium equations [ANSYS, 2024e, Sec. 15.8.5]:

$$[K_T]^{(n,i)} \{D\}_{pert}^{(n,i)} = \{R\}_{pert}^{(n,i)} \tag{2.8}$$

Here, $[K_T]^{(n,i)}$ denotes the tangent stiffness matrix regenerated from the base analysis. The perturbation load corresponds to the term in the parenthesis in equation (2.4). The perturbed displacements are used to calculate the perturbed stress, which is used to calculate the perturbed element stress-stiffness matrix [Cook et al., 2002, p. 647],[ANSYS, 2024e, p. 879].

$$[k_\sigma]_{pert} = \int [G]^T \begin{bmatrix} \sigma_x & \tau_{xy} & \tau_{xz} \\ sym. & \sigma_y & \tau_{yz} \\ & & \sigma_z \end{bmatrix}_{pert} [G] dV \tag{2.9}$$

Here, $[G] = d[N]$ is the differentiated shape function. Finally, the perturbed element stress-stiffness matrices are assembled to a global perturbed stress-stiffness matrix.

In phase 2, the eigenvalue problem based on linear perturbation is formulated by inserting equation (2.7) into (2.3).

$$[K_T]^{(n,i)}\{\phi\}_j = -\lambda_j [K_\sigma]^{(n,i)}_{pert}\{\phi\}_j \tag{2.10}$$

Notice, the load step is at (n,i) because the base analysis is converged at this load step. In [ANSYS, 2024e, p. 879], the right-hand side of equation (2.10) is given with the opposite sign. Based on the derivation provided, the opposite sign is determined to be a typographical error in [ANSYS, 2024e]. λ_1 is used to calculate the 1$^{\text{st}}$ buckling load, by inserting $\{R\}^{(n,i)}_{pert}$ into equation (2.4):

$$\{R\}^{(n,i)}_{buckling} = \{R\}^{(n,i)} + \lambda_1 \{R\}^{(n,i)}_{pert} \tag{2.11}$$

Here, λ_1 measures how much additional perturbation load must be applied for the structure to become unstable. This implies that the base analysis has reached the buckling load when $\lambda_1 = 0$. The accuracy of the two-point approach is better than the one-point approach because the two-point approach captures the change of the global stress-stiffness matrix, rather than linearly extrapolating the stress-stiffness matrix from (n,i). A higher accuracy is important near stability points where the curvature of the stress field is large. The accuracy of the linear extrapolation in equation (2.3) becomes better as load step n approaches the stability point. The two-point approach requires an additional solution of the system to obtain the perturbed displacements. However, this step is computationally inexpensive because the global tangent stiffness matrix is regenerated in phase 1 as a factorized matrix. A detailed description of the implementation is given in [Tønnesen and Christoffersen, 2025, Ch. 3].

Linear Buckling Analysis

The classical linear buckling analysis will briefly be presented as a final remark on the computational methods. The linear buckling analysis includes several simplifying assumptions. The fundamental assumptions are: small displacements, small rotations, linearly elastic materials, and forces independent of displacements. Consequently, a linear proportionality between the external load and the stress-stiffness matrix is assumed from the unloaded state to the stability point [Lindgaard and Lund, 2010, p. 2320]. The base analysis is a linear static analysis that solves the static equilibrium equations.

$$[K_0]\{D\} = \{R\} \tag{2.12}$$

Here, $[K_0]$ does not have a superscript because it does not have displacement-dependencies like in equation (2.6b). $\{D\}$ is the global displacement vector and $\{R\}$ is the global external force vector. The eigenvalue problem is formulated with equations (2.3), (2.4), and (2.5), where load step $n-1$ is the unloaded configuration and load step n is a converged load step. The magnitude of the load applied is arbitrary because linearity is assumed from the unloaded state to the stability point. The change in tangent stiffness from load step 0 to load step 1 is approximated as the global stress stiffness matrix.

$$[K_\sigma] \approx [K_T]^{(1)} - [K_T]^{(0)} \tag{2.13}$$

Inserting equation (2.13) into equation (2.5) and noting that the tangent stiffness at load step 0 is $[K_0]$, the eigenvalue problem is formulated as:

$$([K_0] + \lambda_j [K_\sigma])\{\phi\}_j = \{0\} \tag{2.14}$$

The buckling load is calculated with equation (2.4). The global external load vector is $\{0\}$ at load step 0, and the full load is applied at load step 1. The first buckling load is calculated as:

$$\{R\}^{lin}_{buckling} = \lambda_1 \{R\} \tag{2.15}$$

The linear buckling analysis is a useful tool for analyzing many structures. However, if geometric non-linearities or imperfections are present, the assumptions are violated, and the results cannot be trusted.

Non-Linearity Factors

The non-linearity factors presented in [Tønnesen and Christoffersen, 2025, p. 21-24], provides a method of detecting local buckling, based on the approach outlined in [Lindgaard and Lund, 2011b]. The magnitude of non-linearity is determined by the proportionality of a result with respect to the applied load, measured relative to a previous load step. Non-linearity may be assessed on an element basis as presented in [Tønnesen and Christoffersen, 2025], or for each layer as presented in [Lindgaard and Lund, 2011b]. The following equation is used to calculate the non-linearity factor:

$$\chi^n_{GNL} = 1 + \left| \frac{\frac{\chi^n}{\alpha^n} - \frac{\chi^{ref}}{\alpha^{ref}}}{\frac{\chi^{ref}}{\alpha^{ref}}} \right| \tag{2.16}$$

χ^n_{GNL} is the non-linearity factor calculated at load step n. χ represents a result, such as the 1st principal strain or moment resultants. α refers to the load factor of the applied load. The superscript *ref* represents the reference result, from which linearity is assessed. This may be the first load step or another chosen load step in the linear regime. In the linear regime, equation (2.16) gives $\chi^n_{GNL} = 1$, whereas $\chi^n_{GNL} > 1$ indicates local buckling.

Several results were implemented and assessed for determining non-linearity in [Tønnesen and Christoffersen, 2025]. Firstly, the 1st principal strain and the von Mises equivalent strain-based non-linearity factors were considered. These non-linearity factors are advantageous because non-linearity can be assessed using a single parameter, rather than considering multiple directions per element. The principal strain-based non-linearity factors indicate the load at which the local instability occurs. However, they do not necessarily provide information about where on the structure it occurs [Tønnesen and Christoffersen, 2025].

Secondly, the geometric non-linearity factors, consisting of the moment-resultant, curvature, and difference in in-plane strain-based non-linearity factors. The geometric non-linearity factors capture the onset and progression of non-linear bending behavior. The formulation of the geometric non-linearity factors is based on the rapid increase in deflection of stable post-buckling structures near the stability point of the perfect structure described in [Thompson and Hunt, 1973, p. 68] and the definition of bifurcation in [Cook et al., 2002, p. 639], where the strain energy transitions from membrane to bending at the bifurcation point. The non-linearity factors proved insufficient as stopping criteria when using a critical non-linearity factor χ^c_{GNL}. The magnitude before the observed buckling load varied depending on the specific problem. However, a rapid increase was generally observed before local buckling. Truncation and magnitude filters were necessary, particularly for the geometric non-linearity factors [Tønnesen and Christoffersen, 2025, p. 23 & 62]. The magnitude of the filter and truncation are defined by the truncation number χ_{TN}. See Appendix C for a more detailed description of the truncation and

filter. Consequently, the filter and truncation also significantly influenced the magnitude of the non-linearity factors. However, the non-linearity factors can be used as a post-analysis tool for examining the structural behavior, particularly by plotting the maximum non-linearity factor and displaying the distribution throughout the analysis.

2.3 Failure Modes & Criteria in Sandwich Structures

To facilitate the implementation and evaluation of localized composite failure criteria, WTBs are simplified into more manageable geometries, specifically, plates. The simplification is visualized in Figure 2.8.

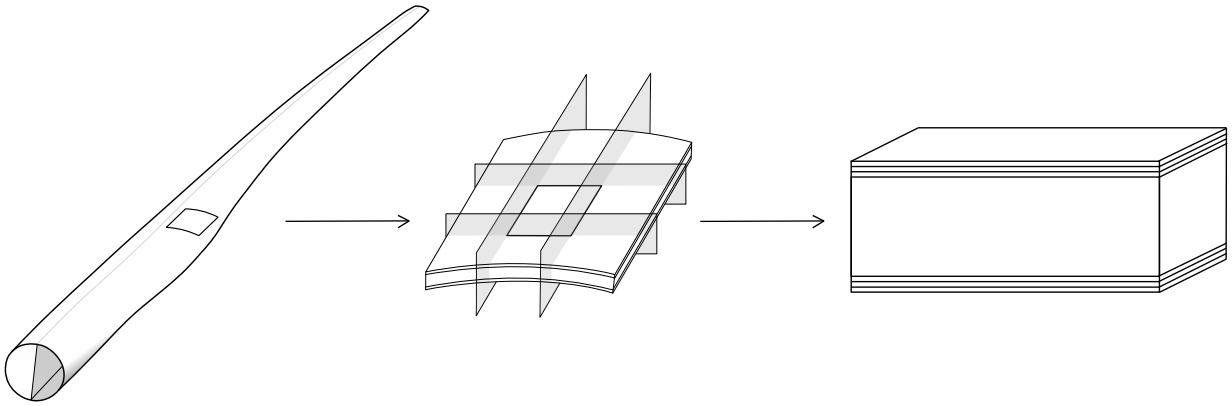

Figure 2.8: Simplification of geometry from a WTB to a plate, used to facilitate implementation of failure criteria.

According to [DNV-GL, 2015], fiber failure must be assessed for all points of the structure under extreme static loading conditions. An appropriate failure criterion shall be employed, with simple stress- and strain-based criteria considered acceptable. A simple approach for determining failure in composite structures, in contrast to progressive damage models, is to utilize a *First Ply Failure* (FPF) criterion [Lund et al., 2024]. This method defines structural failure as the load at which the chosen criterion is first satisfied, in any layer at any location within the structure. However, utilizing FPF does not provide information about the structure's behavior beyond initial failure [Lund et al., 2024]. In particular, changes in stiffness and damage resulting from the first ply failure are not captured. Failure of a single layer does not necessarily result in immediate structural collapse, as the load can be redistributed to surrounding material [Jones, 1999, p. 251]. Nevertheless, over time, the accumulation of cracks will either directly cause a global failure or trigger unstable crack propagation, ultimately destroying the structure [Overgaard et al., 2010a]. Therefore, utilizing FPF can be regarded as a conservative but efficient approach for determining failure.

Several failure modes can arise in sandwich structures, based on a combination of geometry and loading. The failure modes in sandwich structures can be attributed to the face sheets, core, or the interface between them. Moreover, compression can lead to failure associated with instability [Zenkert, 2005, Ch.7]. In the following sections, failure criteria indices are first outlined. Subsequently, intralaminar failure modes and criteria are presented, followed by an overview of failure modes and criteria specific to sandwich structures. The failure criteria implemented in this report derive from ANSYS Composite PrePost (ACP) [ANSYS, 2024a, Ch. 5.3].

2.3.1 Failure Criteria Indices

Several factors can be calculated to evaluate how close a material is to failure. Typically, failure criteria are expressed by a *failure criterion function* (f), which relates the multiaxial stress state to the materials' uniaxial strength parameters [ANSYS, 2025]. A failure criterion function of $f \geq 1$ indicates laminate failure. The *Reserve Factor* (RF) relates the predicted failure load to the applied load, as seen in equation 2.17.

$$\{R\}_f = RF \cdot \{R\} \tag{2.17}$$

Here, $\{R\}_f$ refers to the calculated failure load and $\{R\}$ denotes the applied load. Equation (2.17) implies that failure is yet to occur while $RF > 1$. Typically, RF is calculated with a numeric line search method based on the failure criterion, stresses, strains, and material strength parameters [ANSYS, 2024a, p. 394]. Consequently, at the point of failure, $f = RF = 1$. Moreover, the RF can be used to calculate the *Inverse Reserve factor* (IRF), a more convenient parameter for tracking failure, as failure occurs when $IRF \geq 1$. The IRF is calculated as depicted in equation (2.18).

$$IRF = \frac{1}{RF} \tag{2.18}$$

2.3.2 Intralaminar Failure

When applying the FPF approach, the laminate face sheets of a sandwich structure are evaluated for failure at the lamina level. Since FPF evaluates failure at the lamina level, it becomes essential to consider failure mechanisms that can occur within individual plies.

Intralaminar failure modes, referring to failure occurring within a single lamina, can be classified as either *Fiber Failure* (FF) or *Inter Fiber Failure* (IFF), which encompasses failure of the matrix or in the adhesive failure between fiber and matrix [Puck and Schürmann, 2002]. For a unidirectional FRP lamina subjected to in-plane loading, the failure mode depends on the direction of loading relative to the direction of the fibers [Jones, 2006]. When the lamina is loaded along the fibers, the failure mode is fiber-dominated [Jones, 1999]. On the other hand, when the load is applied in the 2-direction or in shear, the failure mode is IFF-dominated. The failure modes related to in-plane loading of UD lamina are presented in Figure 2.9, along with associated strength parameters. Strength can be defined based on strain (e) and stress (X,Y,S). X is strength along the materials 1-direction, Y is the lamina strength in the 2-direction, and S refers to shear strength. The subscripts t and c denote tension and compression. This distinction is important, as fiber-reinforced lamina tend to have different strengths in tension and compression [Jones, 1999, p. 89].

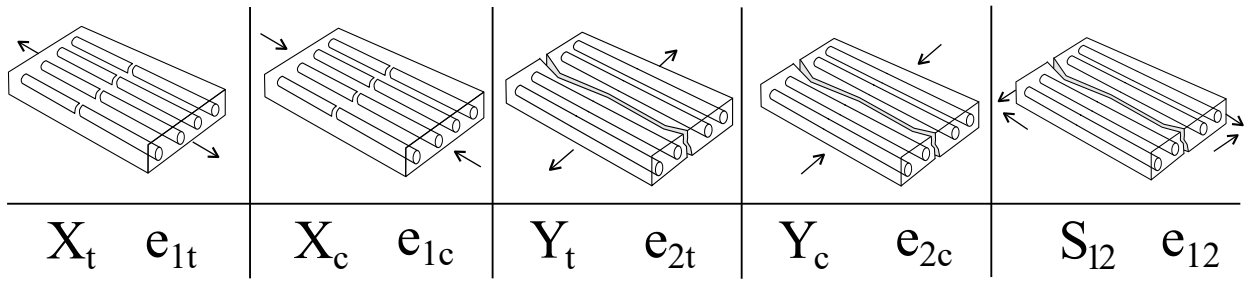

Figure 2.9: Failure modes of a unidirectional lamina under in-plane loading with the associated strength parameters. Inspiration from [Lund et al., 2024, Prt. 6,p. 33].

Failure criteria for fiber-reinforced materials can be classified into four main types: classic, quadratic, modal, and physical [Lund et al., 2024, Prt. 6,p. 32]. The key advantage of classical failure criteria, such as the maximum stress and maximum strain criteria, lies in their simplicity and straightforward application. These criteria consist of three inequality equations, each corresponding to the three directional strength parameters in Figure 2.9, in relation to the associated stress or strain. Failure occurs for the maximum strain failure criteria if:

$$-e_{1c} \geq \varepsilon_1 \geq e_{1t} \qquad -e_{2c} \geq \varepsilon_2 \geq e_{2t} \qquad |\varepsilon_{12}| \geq e_{12} \tag{2.19}$$

These failure criteria facilitate FF and IFF prediction, as visualized in Figure 2.9. However, interaction of stresses or strains is not accounted for [Jones, 1999, p. 106]. Quadratic failure criteria, including Tsai-Hill and Tsai-Wu, appear as curve-fitting models based on experimental data [Lund et al., 2024, Prt.6, p. 44]. These failure criteria describe failure in a multiaxial stress field using a single scalar failure function. Moreover, the quadratic failure criteria account for the interaction of stresses and are invariant to coordinate transformations [Lund et al., 2024]. However, failure modes can not be predicted using the quadratic failure criteria [Jones, 1999, p. 103]. Modal failure criteria, such as Hashin's failure criterion, distinguish between failure modes while considering stress interaction [Lund et al., 2024, Prt. 7, p. 17]. In addition to the five strength parameters shown in Figure 2.9, modal failure criteria require additional strength parameters. Physical failure criteria, which include Puck's action plane criterion, LaRC, and Cuntze's failure criteria, are physically based [ANSYS, 2024a, Lund et al., 2024]. These failure criteria account for stress interaction, differentiate between various failure modes, and provide insight into the underlying failure mechanisms. However, while these criteria offer valuable insight, they require additional strength parameters [ANSYS, 2024a, Ch. 2.5]. Puck's action plane failure criterion is further described in Appendix D.

2.3.3 Sandwich Failure

Sandwich structures have various failure modes related to the general structure, the face sheets, the core, and the interface between the face sheets and the core. In addition to the failure modes relevant to the face sheets described in Section 2.3.2, the stability of the sandwich panel, the stability of the face sheets, and core failure must also be considered. An overview of some of the most common sandwich failure modes is presented in Figure 2.10 [Zenkert, 2005, p. 7.1].

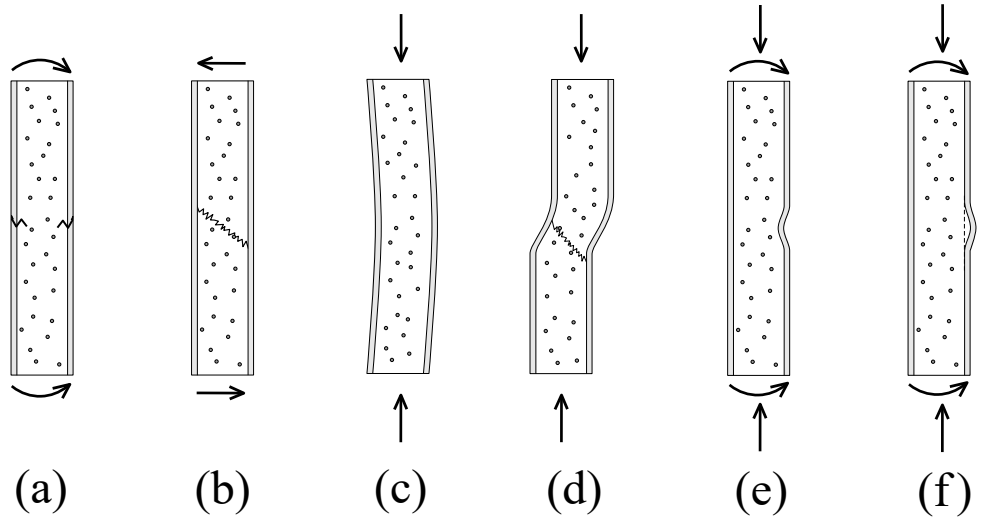

Figure 2.10: Overview of failure modes of sandwich beams. (a) face fracture, (b) core shear failure,(c) general buckling, (d) shear crimping, (e & f) Face sheet wrinkling. Inspiration from [Zenkert, 2005, Fig. 7.1].

Face Fracture
In bending, compression, or extension, the face sheets are subjected to in-plane tension and/or compression, potentially causing failure by fracture, provided that the compressive forces do not first induce instability [Zenkert, 2005, p. 7.2]. Face fracture must be evaluated for both face sheets, as the strength may differ in tension and compression [Zenkert, 2005, p. 7.2]. The failure criteria outlined in Section 2.3.2 apply to assessing face fracture.

Core Failure
The core will carry most of the shear loading, depending on the relative thickness of the face sheets and the core. Consequently, large transverse shear forces can cause failure in the core. Assuming isotropic core material, the shear stress will induce a 45° "shear crack", as illustrated in Figure 2.10(b) [Zenkert, 2005]. PET foam will have a similar response [Fathi, 2018, p. 130]. The appropriate failure criteria depend on the core material analyzed.

In ACP, two failure criterion functions are presented for general core failure. The failure criterion for isotropic core material is based on a simplified Tsai-Wu formulation [ANSYS, 2024a]. The formulation for orthotropic materials is formulated as a maximum stress approach [ANSYS, 2025, p. 25]. The core failure criteria in ACP assume that core failure is dominated by transverse stress and shear stress. Consequently, in-plane stresses are neglected [ANSYS, 2025]. This assumption holds, particularly when $E_f \gg E_c$, as illustrated in Figure B.1 in Appendix B. In a 3-dimensional analysis, the core failure criteria are formulated as:

Isotropic core

$$f_{cf} = \left(\frac{\tau_{13}}{S_{13}}\right)^2 + \left(\frac{\tau_{23}}{S_{23}}\right)^2 + \left(\frac{\sigma_3}{Z_i}\right)^2 \quad i = c \ \textit{if} \ \sigma_3 < 0 \ \textit{else} \ i = t \tag{2.20}$$

Orthotropic core

$$f_{cf} = max\left(\left|\frac{\tau_{13}}{S_{13}}\right|, \left|\frac{\tau_{23}}{S_{23}}\right|, \left|\frac{\sigma_3}{Z_i}\right|\right) \quad i = c \ \textit{if} \ \sigma_3 < 0 \ \textit{else} \ i = t \tag{2.21}$$

In a 2D formulation, $\sigma_3 = 0$. S_{13}, S_{23} and Z are material strength parameters in relation to the corresponding stresses [ANSYS, 2025].

General Buckling & Shear Crimping
In addition to face fracture, compressive loading may cause instability failure in the sandwich panels. Depending on the structure's response, general buckling can be categorized as either global or local buckling, as illustrated in Figure 2.10(c). The onset of local buckling can be detected using the non-linearity factors presented in Section 2.2.3.

According to [Sullins et al., 1969] shear crimping should not be classified as a local failure mode of a sandwich structure, but rather a special form of general buckling. Shear crimping occurs in cases where the wavelength of the buckled configuration is very small, typically in cases where the core material has a low transverse shear modulus [Sullins et al., 1969, p. 41]. Shear crimping is illustrated in Figure 2.10(d). Crimping may occur suddenly, which can cause the core to fail as a result of significant transverse shear stresses induced by out-of-plane deformations [ANSYS, 2025, Zenkert, 2005]. Additionally, crimping can be induced for buckled configurations featuring larger waves, due to significant local transverse shear stresses at the end of the wave pattern [Sullins et al., 1969]. Crimping can also occur in sandwich panels with both thin and thick face sheets, particularly in regions with a sudden change in laminate stiffness [ANSYS, 2024a].

Three equations for calculating the critical shear crimping load resultant N_{sc} are presented in [ANSYS, 2024a, p. 415]. The first, initially proposed by [Vinson, 1986] [ANSYS, 2024a, p. 416], assumes very thin face sheets. Consequently, the contribution of the face sheets to resist shear crimping is disregarded. For a sandwich panel with very thin face sheets under a uniaxial load, the equation is given as:

$$N_{sc} = G_C \cdot t_C \tag{2.22}$$

G is the transverse shear modulus in the direction of loading, and t is thickness. The subscript C refers to the core. Equation (2.22) is valid for sufficiently large sandwich panels, where crimping is not influenced by boundary conditions [Coburn and Weaver, 2016]. If the sandwich structure features thicker face sheets, equation (2.22) may yield an underestimation of the critical shear crimping load resultant N_{sc} [Coburn and Weaver, 2016, p. 6].

Furthermore, Vinson also proposed a criterion considering the face sheets' contribution to the critical shear crimping load resultant N_{sc} [ANSYS, 2024a, p. 416]. According to [Coburn and Weaver, 2016], equation (2.23) assumes thin face sheets, in contrast to the very thin face sheet assumption made in equation (2.22).

$$N_{sc} = G_C \cdot \frac{h^2}{t_C} \qquad\qquad h = t_C + \frac{(t_{Fb} + t_{Ft})}{2} \tag{2.23}$$

The subscript F represents the face sheets, and t and b refer to top and bottom, respectively. h^2 is denoted as h_2 in equation [ANSYS, 2024a, eq. 5.120], which is believed to be a typographical error, supported by equation (21) in [Coburn and Weaver, 2016].

The final equation, which is used in ANSYS is a slightly modified formulation of the allowable shear crimping load resultant, N_{sc}:

$$N_{sc} = G_C \cdot (k_C \cdot t_C + k_F \, (t_{Fb} \cdot t_{Ft})) \tag{2.24}$$

The shear crimping factors k are weighting factors for the core and face sheet terms. These factors allow for the configuration of the shear crimping criterion to account for material and application [ANSYS, 2024a]. The allowable shear crimping load is highly sensitive to imperfections; consequently, ANSYS recommends that the shear crimping factors be determined experimentally [ANSYS, 2024a, p. 415]. The default values are set to $k_C = 1$ and $k_F = 0$, which reduces equation (2.24) to equation (2.22). If both shear crimping factors are set to 1, equation (2.24) closely coincides with equation (2.23) [ANSYS, 2024a].

For a multiaxial loading condition, the IRF is calculated in the principal directions as a sum of efforts [ANSYS, 2024a]. Equation (2.25) applies to uniaxial compression, while equation (2.26) is formulated for biaxial compression.

$$IRF_{sc} = \frac{-N_\xi}{N_{sc,\xi}} \qquad \textit{for } N_\eta \geq 0 \ \& \ N_\xi < 0 \tag{2.25}$$

$$IRF_{sc} = \frac{-N_\xi}{N_{sc,\xi}} + \frac{-N_\eta}{N_{sc,\eta}} \qquad \textit{for } N_\eta < 0 \ \& \ N_\xi < 0 \tag{2.26}$$

The subscripts ξ and η are the axes of a Cartesian coordinate system in which ξ is in the principal direction of maximum in-plane compression, the axis ζ is perpendicular to the face sheets, while η is orthogonal to the $\xi\zeta$-plane. In Figure 4.2, the $\xi\eta$-coordinate system is shown in relation to the material and element coordinate systems.

Face Sheet Wrinkling

Face sheet wrinkling (e & f) in Figure 2.10 is an instability phenomenon like general buckling and shear crimping. However, face sheet wrinkling only concerns the stability of the face sheets of the sandwich structures. In this sense, it is a more localized instability failure mode than general buckling and shear crimping [Sullins et al., 1969, p. 1-4]. Face sheet wrinkling can occur in three different modes, namely antisymmetric, symmetric, and one-sided. The antisymmetric and symmetric modes are shown in Figure 2.11. The one-sided mode is illustrated in Figure 2.10. This mode is more applicable when considering bending or unequal face sheets [Niu and Talreja, 1999].

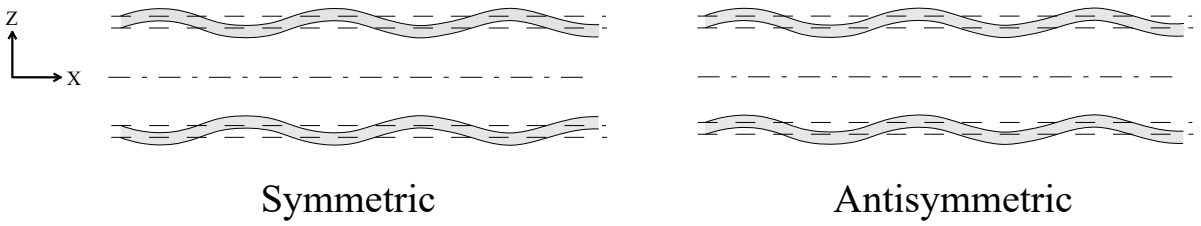

Figure 2.11: Modes of instability for face sheet wrinkling. Inspired by Fig. 6.1 [Zenkert, 2005, p. 160] and [Niu and Talreja, 1999, Fig. 1]. The dotted lines represent the unbuckled state of the face sheets.

Many methods exist for calculating the onset of wrinkling. In [Zenkert, 2005], Winkler's elastic foundation model, Hoff's method based on energy, and a solution of the governing differential equation with Airy's stress function are presented. Each method provides different formulae for calculating the in-plane compressive stress inducing face sheet wrinkling. An overview of the state-of-the-art in 1999 is given in [Ley et al., 1999]. Eight different theoretical wrinkling stresses are provided in Table 1 in [Ley et al., 1999] for sandwich plates with thick cores in compression. The overview in [Ley et al., 1999] is not an exhaustive review of the available theories. The intent is to give design engineers and analysts a foundation for selecting the correct formula. The various methods and models are inconvenient for a design engineer, and choosing a simple expression suitable for a general case is challenging, as highlighted in [Niu and Talreja, 1999, p. 875]. The many formulae for the theoretical wrinkling stress are a testament to the problem-specific nature of the failure mode.

The general analysis model in [Zenkert, 2005, p. 6.1] [Sullins et al., 1969, p. 2-21] and [ANSYS, 2024a, p. 413] can be viewed as a plate on an elastic foundation under in-plane compression. The materials are assumed to be linearly elastic and homogeneous. The method provided in [ANSYS, 2024a, p. 414] reflects the current theory used in industry and is based on the procedures provided in [Sullins et al., 1969] and [ESA, 1994]. In [ANSYS, 2024a] and [Zenkert, 2005], the core is assumed sufficiently thick, and the deformation of one face sheet does not interact with the other. The formula in [ANSYS, 2024a] for calculating the wrinkling stress is:

$$\sigma_{w,\xi} = -Q \left(\frac{E_{F,\xi} E_{C,\zeta} G_{C,\zeta\xi}}{1 - \nu_{F,\xi\eta} \nu_{F,\eta\xi}} \right)^{1/3} \tag{2.27}$$

The theoretical value of Q, corresponding to a perfect structure is $Q = 0.825$ [ESA, 1994, Eq. 26.10.1]. A more conservative value of Q that better represents experimental data is $Q = 0.5$. $E_{F,\xi}$ is Young's modulus of the face sheet in the ξ-direction. $G_{C,\zeta\xi}$ is the transverse shear modulus of the core. $\nu_{F,\xi\eta}$ and $\nu_{F,\eta\xi}$ are the major and minor Poisson's ratios of the face sheet. In biaxial compression, an interaction formula is recommended [Sullins et al., 1969, p. 2-26][ANSYS, 2024a, p. 414].

$$f_{w,Fi} = \left(\frac{\sigma_\xi}{\sigma_{w,\xi}}\right) + \left(\frac{\sigma_\eta}{\sigma_{w,\eta}}\right)^3 \quad for\ \frac{\sigma_\xi}{\sigma_{w,\xi}} \geq \frac{\sigma_\eta}{\sigma_{w,\eta}} \tag{2.28}$$

$$f_{w,Fi} = \left(\frac{\sigma_\eta}{\sigma_{w,\eta}}\right) + \left(\frac{\sigma_\xi}{\sigma_{w,\xi}}\right)^3 \quad for\ \frac{\sigma_\xi}{\sigma_{w,\xi}} < \frac{\sigma_\eta}{\sigma_{w,\eta}} \qquad for\ i = t,b \tag{2.29}$$

Here $\sigma_{w,\xi}$ and $\sigma_{w,\eta}$ are calculated as uniaxial compressive cases as in equation (2.27). If in-plane shear stress is present, the principal stresses should be calculated first and used in the above interaction formula. For a given cross-section of a sandwich structure, the failure criterion function is independently calculated for the top and bottom faces, and a single reserve factor for the cross-section is evaluated as:

$$RF_w = max(RF_{w,Ft}, RF_{w,Fb}) \tag{2.30}$$

2.4 Safety Factors

The choice of analysis method and failure criteria is motivated by the design guidelines [DNV-GL, 2015]. The guidelines specify the required analysis and specify a set of partial safety factors depending on the employed analysis methods. The total safety factor is the product of all partial factors:

$$\gamma_m = \gamma_{m0}\ \gamma_{mc}\ \gamma_{m1}\ \gamma_{m2}\ \gamma_{m3}\ \gamma_{m4}\ \gamma_{m5} \tag{2.31}$$

Here, γ_{m0} is a base factor associated with all verification analyses, γ_{mc} relates to criticality of the failure mode, γ_{m1} is long term degradation of materials in the blade, γ_{m2} accounts for temperature effects, γ_{m3} accounts for manufacturing effects, γ_{m4} corrects for the accuracy of the analysis method, and γ_{m5} relates to the number of loads considered in the load envelope.

An overview of the safety factors associated with the presented analysis method is given in Table 2.1.

Factor	**Buckling**	**Fiber failure**	**Inter-fiber failure**	**Description**
γ_{m0}	1.20	1.20	1.20	Base factor
γ_{mc}	1.08	1.08	1.00	Failure criticality
γ_{m1}	1.05	1.20	1.10	Long-term degradation
γ_{m2}	1.05	1.10	1.00	Temperature
γ_{m3}	1.10	1.30	1.00	Manufacturing
γ_{m4}	1.05	1.00	1.15	Analysis accuracy
γ_{m5}	1.00	1.00	1.00	Load cases
γ_m	1.65	2.22	1.52	Total safety factor

Table 2.1: Partial safety factors required based on the presented analysis approach.

The partial safety factors reveal the importance of a GNL analysis for buckling. The partial safety factor associated with a linear analysis is $\gamma_{m4} = 1.25$, resulting in an overall safety factor of $\gamma_m = 1.96$.

3 | Analysis Method

This chapter provides an overview of the implemented non-linear buckling analysis described in Section 2.2.3, before outlining the implementation of the sandwich failure criteria. The analysis method is developed in ANSYS Parametric Design Language (APDL), where a simplified schematic overview of the program is given in Figure 3.1. Additional development has been made from the non-linear buckling analysis presented in [Tønnesen and Christoffersen, 2025], to facilitate post-processing of sandwich failure criteria and the parametric study for the Gurit98m WTB model.

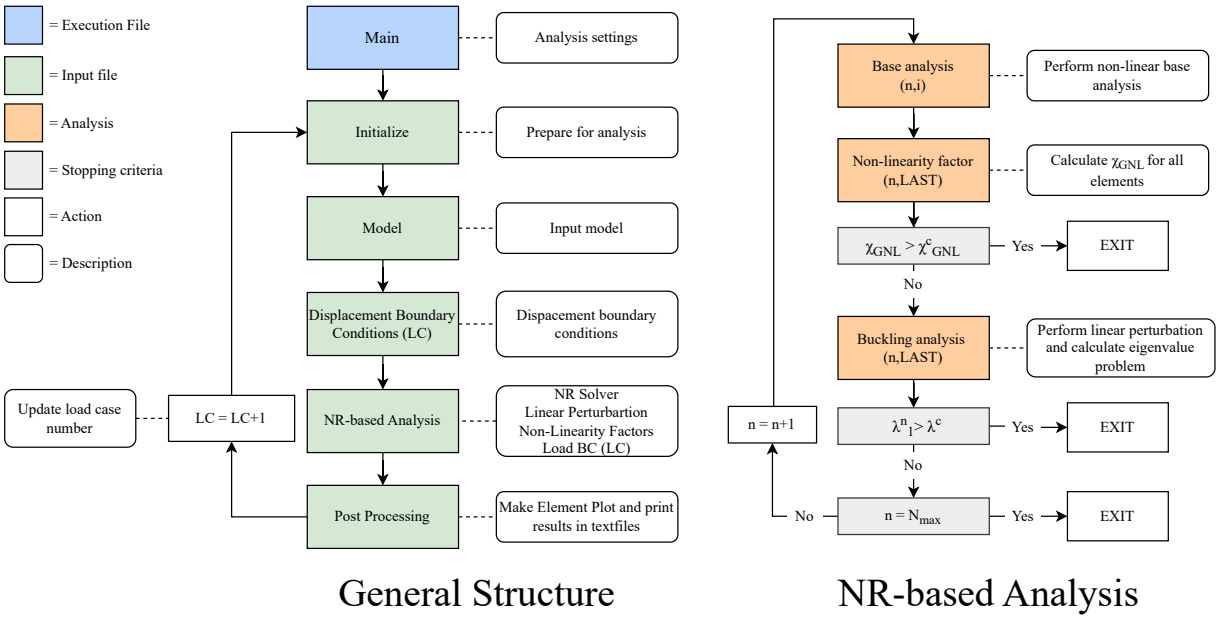

Figure 3.1: Simplified overview of the non-linear buckling analysis presented in [Tønnesen and Christoffersen, 2025].

The different parts of the analysis are divided into separate input files. An input file is an ASCII file used for implementing APDL code, with the extension *.inp*. Input files can be edited with standard text editors and executed with the `/INPUT` command in the APDL utility menu. The program utilizes a single-file configuration, meaning the entire analysis is executed from one file, the *Main* input file, which also contains all user-defined analysis settings. After executing *Main*, a loop is initiated for the Load Cases (LCs). Following this, *Initialize* prepares the program for a new analysis, after which the model and displacement boundary conditions are introduced. Then, the non-linear buckling analysis is executed in the *NR-based Analysis*, where the load boundary conditions are incrementally applied and buckling based on linear perturbation is performed.

ANSYS utilizes Multiframe Restart to perform the linear perturbation, which allows for pausing and resumption of an analysis at a user-defined load step and substep [ANSYS, 2024c, p. 116]. Multiframe Restart is incompatible with the arc-length method. Therefore, the Newton-Raphson (NR) method is utilized instead. In contrast to the arc-length method, the Newton-Raphson method is susceptible to numerical stability issues when the tangent stiffness matrix becomes singular or ill-conditioned. Therefore, stopping criteria are necessary to ensure the analysis does not pass a critical point. The overview of the NR-based analysis is shown on the right side in Figure 3.1. In the NR-based analysis, a GNL load step is solved in the base analysis. The load is equally incremented based on the total number of load steps, as presented in the following equation:

$$\alpha^n = \frac{n}{N_{max}} \qquad \{R\}^n = \alpha^n \cdot \{R\} \tag{3.1}$$

α^n is the load factor for load stepping in the NR-based analysis. α^n is multiplied by the reference load $\{R\}$, which is the load defined in the boundary condition files. n is the current load step, and N_{max} is the user-defined total number of load steps. Following the base analysis, non-linearity factors are calculated for the current load step n and the last sub-step ($i = LAST$) on an element basis. The maximum non-linearity factor is checked against a user-defined critical non-linearity factor χ^c_{GNL}. The analysis is terminated if:

$$max\left(\{\chi\}^{(n,LAST)}_{GNL}\right) \geq \chi^c_{GNL} \tag{3.2}$$

If equation 3.2 is false, the analysis resumes from $(n, LAST)$, followed by the buckling analysis based on linear perturbation.

The perturbation load is applied as a small increment to the external force. The perturbation load is defined in equation (3.3).

$$\{R\}^{(n,i)}_{pert} = \zeta_{pert}\{R\}^{(n,i)} \tag{3.3}$$

ζ_{pert} is the perturbation load factor, i.e., a scalar multiplier for the applied load. ζ_{pert} should be a small fraction of the applied load as the perturbation load should guide the structure on the current deformation path [Bathe, 1996, p. 630-634] of its current state. The nodal coordinates are updated according to the perturbation displacements, and the eigenvalue problem is solved as described in Section 2.2.3.

After solving for λ_1, the buckling load factor γ^n is calculated, which relates the approximated buckling load $\{R\}^n_{buckling}$ to the reference load $\{R\}$.

$$\gamma^n = \alpha^n \cdot \eta \cdot (1 + \lambda^n_1 \cdot \zeta_{pert}) \qquad \{R\}^n_{buckling} = \gamma^n \cdot \{R\} \tag{3.4}$$

η is the external load factor, which scales the loads defined in the boundary condition file. η is useful for applying safety factors. λ^n_1 is the lowest positive eigenvalue at load step n. For $\gamma^n \leq 1$, the structure is approximated to buckle for the applied load. The analysis terminates if the converged base analysis is within a user-defined tolerance of the calculated buckling load.

$$\lambda^n_1 \leq \lambda^c \tag{3.5}$$

The appropriate magnitude of λ^c is problem-specific. However, the assumptions described in Section 2.2.3 should not be violated. This check helps ensure that the analysis does not exceed the stability point, thereby mitigating the risk of numerical issues related to the NR method. If this is false and the analysis has not reached the maximum number of load steps $n = N_{max}$, the analysis is restarted from (n,$LAST$), the load step number n is incremented, and a new load step is performed.

After the NR-based analysis, the *Post Processing* input file is executed. A text file is printed documenting the reason for termination, the final buckling load factor γ, and its history throughout the

analysis. Additionally, text files are generated for all enabled non-linearity factors throughout the analysis. These text files can be post-processed to visualize the non-linearity factors for all load steps in the APDL Utility Menu. Moreover, the averaged element stresses in the material coordinate system for all layers' top, middle, and bottom positions and the force resultants for all elements are printed into text files. These text files are used to post-process the sandwich failure criteria in Fortran. The stresses and force resultants are extracted with the `ETABLE` command. The output coordinate system is defined as the material coordinate system along with the specific layer and position before extracting the averaged element stresses using `ETABLE`. The `ETABLE` command outputs an averaged element centroidal stress, calculated as an average based on the element's nodal values [ANSYS, 2024b, p. 688-689] & [ANSYS, 2024c, p. 52]. The force resultants are calculated as an average based on the sum of the contributing nodal values [ANSYS, 2024b, p. 689]. Finally, if the program has not reached the final LC, the current LC is updated, and a new analysis is performed.

4 | Implementation of Sandwich Failure Criteria

This chapter describes the implementation of sandwich failure criteria in a post-processing program based on a reduced version of Aalborg University's (AAUs) in-house software MUlti Disciplinary Synthesis Tool (MUST). MUST can read discretized models exported from ANSYS, including nodal coordinates, element formulations, connectivity, material models, coordinate systems, and specific bookkeeping for sandwich structures and laminates. MUST offers many features, such as structural analysis and topology optimization.

To avoid confusion between the complete MUST program and the post-processing routine developed in this project, all post-processing procedures will be referred to as Fortran Post-Processing (FPP).

Within FPP, sandwich-specific bookkeeping assigns a unique index to each element, indicating if the element is a sandwich structure. It categorizes each ply into one of three predefined ply groups (PG): top face sheet, core, and bottom face sheet, respectively. This grouping is based on the assumption that the in-plane stiffness of the core is significantly lower than that of the face sheets, i.e., $E_{1,C} \ll E_{1,F}$. The bookkeeping process categorizes the layup data for each element, including thickness, material orientation, and material properties, according to these ply groups. This categorized data, referred to as Ply Group Layup Data (PGLD), forms the basis for the constitutive modeling of each ply group independently.

Furthermore, the PGLD is used to calculate the stress within each group using the element stress from APDL. Stress values are averaged through-the-thickness for each ply group as described in the following equation:

$$\{\sigma_{xyz}\}_{PG} = \frac{1}{3N_{PG}} \sum_{k=1}^{N_{PG}} \sum_{p=1}^{3} \left[T(\theta_{x1}^{k})\right]^{T} \{\sigma_{123}\}^{(k,p)} \qquad for \quad PG = Ft,C,Fb \tag{4.1}$$

In equation (4.1), N_{PG} denotes the number of layers within a given ply group. p is the number of data points through the thickness of each lamina. The matrix $[T]$ represents the in-plane rotation matrix [Cook et al., 2002, p. 274]. The material angle θ_{x1} is the angle from the x-axis of the element coordinate system to the 1-axis of the material coordinate system. The subscripts 123 and xyz on the element stress vectors indicate the material and element coordinate systems, as presented in Figure 4.1. The exact method of determining the stress acting on a face sheet is not explicitly stated in the documentation, however, the definition of equation (4.1) stems from the formulation: "*The average face sheet stresses σ_x, σ_y, τ_{xy} are obtained from the layer stresses of the face sheets.*" [ANSYS, 2024a, p. 414].

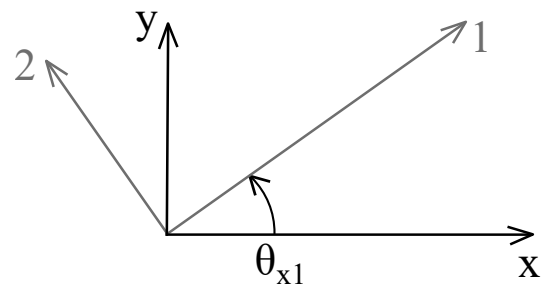

Figure 4.1: Element coordinate system and material coordinate system. {1,2} *represents the material coordinate system, and* {x,y} *depicts the element coordinate system.*

Since the stress components are averaged in the element coordinate system, the stresses are transformed from the material coordinate system to the element coordinate system before averaging. The in-plane rotation matrix $[T(\theta)]$ is defined in equation (4.2).

$$[T(\theta)] = \begin{bmatrix} a^2 & b^2 & 0 & ab & 0 & 0 \\ b^2 & a^2 & 0 & -ab & 0 & 0 \\ 0 & 0 & 1 & 0 & 0 & 0 \\ -2ab & 2ab & 0 & a^2-b^2 & 0 & 0 \\ 0 & 0 & 0 & 0 & a & -b \\ 0 & 0 & 0 & 0 & b & a \end{bmatrix} \qquad for \quad a = cos(\theta) \quad \& \quad b = sin(\theta) \tag{4.2}$$

4.1 Constitutive Modeling

Constitutive modeling in this context refers to the procedure used to extract the engineering constants in the principal $\xi\eta$-coordinate system. The first step involves determining the orientation of the $\xi\eta$-system relative to the element coordinate system. Here, the ξ-direction is aligned with the direction of maximum compressive stress, corresponding to the second principal stress direction under a plane stress assumption. The approach for determining the principal stresses and associated angles follows [Goodno and Gere, 2016, Sec. 7.3].

The orientation of the principal directions is obtained by calculating the principal angle using equation (4.3).

$$\theta_p = \frac{1}{2} tan^{-1}\left(\frac{2\tau_{xy}}{\sigma_x - \sigma_y}\right) \tag{4.3}$$

The principal angle θ_p defines the orientation of the principal planes on which the principal stresses act. Equation (4.3) yields two possible solutions for θ_p: one in the range of 0° to 90°, and the other in the range of 90° to 180°.

To identify which of the two angles corresponds to the direction of maximum compressive stress (i.e., the second principal stress), the calculated angle is substituted into the x-component of the plane stress transformation equation, given by equation (4.4):

$$\sigma_{x'} = \frac{\sigma_x + \sigma_y}{2} + \frac{\sigma_x - \sigma_y}{2} cos(2\theta_p) + \tau_{xy} sin(2\theta_p) \tag{4.4}$$

The resulting stress $\sigma_{x'}$ is then compared with the principal stresses σ_{1p} and σ_{2p}, which are given by:

$$\sigma_{1p,2p} = \frac{\sigma_x + \sigma_y}{2} \pm \sqrt{\left(\frac{\sigma_x - \sigma_y}{2}\right)^2 + \tau_{xy}^2} \tag{4.5}$$

If $\sigma_{x'}$ is equal to σ_{1p}, then the principal angle θ_p corresponds to the direction of maximum tensile stress. Consequently, the direction of maximum compressive stress, aligned with the ξ-axis, is orthogonal to this, and the angle between the x-axis of the element coordinate system and the ξ-direction is $\theta_{x\xi} = \theta_p + 90°$. Conversely, if $\sigma_{x'}$ equals σ_{2p}, then θ_p already defines the direction of maximum compressive stress, and $\theta_{x\xi} = \theta_p$.

A few unique cases are encountered with the described method. In the case of pure biaxial loading, i.e., $\sigma_x = \sigma_y$ and $\tau_{xy} = 0$ the fraction in equation (4.3) is $\frac{0}{0}$, which causes computational issues. This is avoided by manually setting the principal angle $\theta_p = 0°$. In the case of equal biaxial loading with shear $\tau_{xy} \neq 0$, the principal direction is set to $\theta_p = \pi/4$. A final check is performed regarding the association of the principal angle and the direction of maximum compression. For the case of pure biaxial loading, the $\xi\eta$-system coincides with the element coordinate system, and the most compressive direction is manually set to be the x-direction, i.e., $\theta_{x\xi} = \theta_p$. Numerical evaluation using double precision variables is prone to round-off errors, so determining if the loading is purely biaxial in the above checks is done with $|\sigma_x - \sigma_y| < 10^{-8}$. Likewise, the shear stress is treated as zero if $|\tau_{xy}| < 10^{-8}$ and different from zero if $|\tau_{xy}| > 10^{-8}$.

To determine the engineering constants in the $\xi\eta$-coordinate system, the angle from the $\xi\eta$-system to the material coordinate system must be established. This angle, denoted as $\theta_{\xi 1}$, is computed as:

$$\theta_{\xi 1} = \theta_{x1} - \theta_{x\xi} \tag{4.6}$$

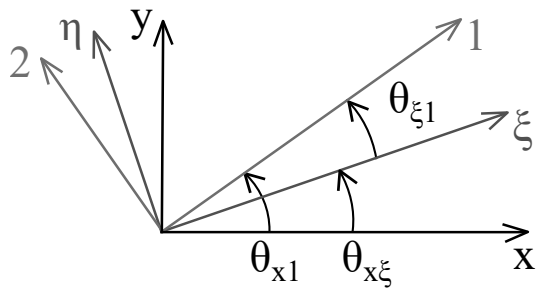

Figure 4.2: Element coordinate system, $\xi\eta$-coordinate system and material coordinate system. {1,2} *represents the material coordinate system, and* {x,y} *depicts the element coordinate system.*

With $\theta_{\xi 1}$ determined, the engineering constants are calculated based on FSDT. The constitutive behavior of a laminate is described by the ABD-matrix, which relates the force and moment resultants to the mid-plane strain and curvature, as seen in equation (4.7).

$$\left\{\begin{array}{c} N \\ \hline M \\ \hline Q \end{array}\right\} = \left[\begin{array}{c|c|c} A & B & 0 \\ \hline B & D & 0 \\ \hline 0 & 0 & \bar{A} \end{array}\right] \left\{\begin{array}{c} \varepsilon^0 \\ \hline \tilde{\kappa} \\ \hline \gamma^0 \end{array}\right\} \tag{4.7}$$

The assembly of the ABD-matrix is based on the orthotropic stiffness matrix of each ply, denoted as $[\hat{C}]$.

$$\begin{Bmatrix} \sigma_1 \\ \sigma_2 \\ \sigma_3 \\ \tau_{12} \\ \tau_{23} \\ \tau_{13} \end{Bmatrix} = \begin{bmatrix} \frac{E_1}{1-\nu_{12}\nu_{12}} & \frac{\nu_{21}E_1}{1-\nu_{12}\nu_{21}} & 0 & 0 & 0 & 0 \\ \frac{\nu_{12}E_2}{1-\nu_{21}\nu_{12}} & \frac{E_2}{1-\nu_{12}\nu_{21}} & 0 & 0 & 0 & 0 \\ 0 & 0 & 0 & 0 & 0 & 0 \\ 0 & 0 & 0 & G_{12} & 0 & 0 \\ 0 & 0 & 0 & 0 & G_{23} & 0 \\ 0 & 0 & 0 & 0 & 0 & G_{13} \end{bmatrix} \begin{Bmatrix} \varepsilon_1 \\ \varepsilon_2 \\ \varepsilon_3 \\ \gamma_{12} \\ \gamma_{23} \\ \gamma_{13} \end{Bmatrix} \tag{4.8}$$

In FSDT, the transverse normal strain is assumed to be zero [Mittelstedt, 2023, Sec . 10.1]. This is enforced by setting the entry in the 3rd row and 3rd column to zero. The stiffness matrix for each ply is rotated into the element coordinate system [Cook et al., 2002, p. 275].

$$[\bar{C}] = [T(\theta_{\xi 1})]^T [\hat{C}][T(\theta_{\xi 1})] \tag{4.9}$$

Here, $[\bar{C}]$ represents the transformed stiffness matrix, analogous to the plane stress reduced stiffness matrix $[\bar{Q}]$ used in CLT, but includes all six stress components [Jones, 1999, Sec.4.2]. The contribution of each ply to the overall laminate stiffness is then incorporated into the calculation of the ABD-matrix, as shown in equations (4.10)–(4.13). The individual submatrices are calculated by integrating the transformed ply stiffness matrices $[\bar{C}]$ through the laminate thickness:

$$A_{ij} = \sum_{k=1}^{N_{PG}} (\bar{C}_{ij})_k \, (z_k - z_{k-1}) \qquad i,j = 1,2,4 \tag{4.10}$$

$$B_{ij} = \frac{1}{2} \sum_{k=1}^{N_{PG}} (\bar{C}_{ij})_k \left(z_k^2 - z_{k-1}^2 \right) \qquad i,j = 1,2,4 \tag{4.11}$$

$$D_{ij} = \frac{1}{3} \sum_{k=1}^{N_{PG}} (\bar{C}_{ij})_k \left(z_k^3 - z_{k-1}^3 \right) \qquad i,j = 1,2,4 \tag{4.12}$$

$$\bar{A}_{ij} = \sum_{k=1}^{N_{PG}} (\bar{C}_{ij})_k \, (z_k - z_{k-1}) \qquad i,j = 5,6 \tag{4.13}$$

To extract the relevant engineering constants, the ABD-matrix is inverted to obtain the laminate compliance matrix [Jones, 1999, sec. 4.4.1]. Inverting the ABD-matrix captures all coupling effects potentially present in a laminate.

$$\left\{ \begin{array}{c} \varepsilon^0 \\ \hline \tilde{\kappa} \\ \hline \gamma^0 \end{array} \right\} = \left[\begin{array}{c|c|c} A' & B' & 0 \\ \hline (B')^T & D' & 0 \\ \hline 0 & 0 & \bar{A}' \end{array} \right] \left\{ \begin{array}{c} N \\ \hline M \\ \hline Q \end{array} \right\} \tag{4.14}$$

The prime superscripts show that the submatrices are the compliance matrices. The diagonal terms of the compliance matrix are directly related to the engineering constants [Jones, 1999, p. 64]. Since only the in-plane engineering constants are required for the sandwich failure criteria, the in-plane compliance submatrix is isolated and normalized with respect to the total laminate thickness t_{PG}.

$$[S] = t_{PG} \begin{bmatrix} A'_{11} & A'_{12} & 0 & A'_{14} & 0 & 0 \\ A'_{21} & A'_{22} & 0 & A'_{24} & 0 & 0 \\ 0 & 0 & 0 & 0 & 0 & 0 \\ A'_{41} & A'_{42} & 0 & A_{44} & 0 & 0 \\ 0 & 0 & 0 & 0 & \bar{A}'_{55} & \bar{A}'_{56} \\ 0 & 0 & 0 & 0 & \bar{A}'_{65} & \bar{A}'_{66} \end{bmatrix} \tag{4.15}$$

The engineering constants can then be extracted from $[S]$ as:

$$E_\xi = \frac{1}{S_{11}} \qquad E_\eta = \frac{1}{S_{22}} \qquad \nu_{\xi\eta} = -\frac{S_{21}}{S_{11}} \qquad \nu_{\eta\xi} = -\frac{S_{12}}{S_{22}} \tag{4.16}$$

$$G_{\zeta\eta} = \frac{1}{S_{55}} \qquad G_{\zeta\xi} = \frac{1}{S_{66}} \tag{4.17}$$

4.2 Face Sheet Wrinkling

The wrinkling stress σ_w is calculated based on engineering constants in the $\xi\eta$-coordinate system for the face sheet and core ply group, as is evident in equation (2.27). The calculation of these constants is described in Section 4.1. The pseudo code for implementing face sheet wrinkling, see equations (2.27)-(2.30), is presented in Table 4.1.

1:	**do** $ElemNo = 1..nElem$
2:	**do** $PG = Ft,Fb$
3:	Compute: $\sigma_{1p,2p}$
4:	**if** $\sigma_{1p} > -10^{-8}$ and $\sigma_{2p} > -10^{-8}$
5:	Set: $f_{w,PG} = 0$
6:	Go to line 2
7:	**end if**
8:	Compute: $E_{PG,\xi}$, $E_{PG,\eta}$, $\nu_{PG,\xi\eta}$, $\nu_{PG,\eta\xi}$, $E_{C,\zeta}$,$G_{C,\zeta\eta}$, $G_{C,\zeta\xi}$
9:	**if** $\sigma_{1p} > -10^{-8}$ and $\sigma_{2p} < -10^{-8}$
10:	Compute: $f_{w,PG} = \sigma_{2p}/\sigma_{w,\xi}$
11:	**else if** $\sigma_{1p} < -10^{-8}$ and $\sigma_{2p} < -10^{-8}$
12:	Compute: $f_{w,PG,\xi} = \sigma_{2p}/\sigma_{w,\xi}$
13:	Compute: $f_{w,PG,\eta} = \sigma_{1p}/\sigma_{w,\eta}$
14:	**if** $f_{w,PG,\xi} \geq f_{w,PG,\eta}$
15:	Compute: $f_{w,PG} = f_{w,PG,\xi} + f^3_{w,PG,\eta}$
16:	**else**
17:	Compute: $f_{w,PG} = f_{w,PG,\eta} + f^3_{w,PG,\xi}$
18:	**end if**
19:	**end if**
20:	**end do**
21:	Compute: $f_w = max(f_{w,Ft}, f_{w,Fb})$
22:	**end do**

Table 4.1: Pseudo code for implementation of face sheet wrinkling in Fortran post processing. nElem is the number of elements in the model.

Due to the numerical accuracy of double precision variables, the if-statements on lines 4, 9, and 11 are only true if the stress is less than or more than -10^{-8}.

4.3 Shear Crimping

Evaluating the failure criterion function for shear crimping involves many of the same steps as face sheet wrinkling. The main difference is the use of force resultants rather than stress. The interaction formula is also different. The pseudo code for shear crimping, see equations (2.24)-(2.26), is presented in Table 4.2.

1:	**do** $ElemNo = 1..nElem$
3:	Compute: $N_{1p,2p}$
4:	**if** $N_{1p} > -10^{-8}$ and $N_{2p} > -10^{-8}$
5:	Set: $f_{sc} = 0$
6:	Go to line 1
7:	**end if**
8:	Compute: $G_{C,\zeta\eta}$, $G_{C,\zeta\xi}$
9:	**if** $N_{1p} > -10^{-8}$ and $N_{2p} < -10^{-8}$
10:	Compute: $f_{sc} = -N_{2p}/N_{sc,\xi}$
11:	**else if** $N_{1p} < -10^{-8}$ and $N_{2p} < -10^{-8}$
12:	Compute: $f_{sc} = -N_{2p}/N_{sc,\xi} - N_{1p}/N_{sc,\eta}$
13:	**end if**
14:	**end do**

Table 4.2: Pseudo code for implementing shear crimping in Fortran post processing.

4.4 Core Failure

The implementation of core failure utilises the ply group layup data and the ply group stress for the core. The pseudo code for implementing core failure, see equations (2.20)-(2.21), is presented in Table 4.3.

1:	**do** $ElemNo = 1..nElem$
2:	**if** $Elem = isotropic$
3:	Compute: $f_{cf} = \left(\frac{\tau_{13}}{S_{13}}\right)^2 + \left(\frac{\tau_{23}}{S_{23}}\right)^2$
4:	**else if** $Elem = orthotropic$
5:	Compute: $f_{cf} = max\left(\left\|\frac{\tau_{13}}{S_{13}}\right\|, \left\|\frac{\tau_{23}}{S_{23}}\right\|\right)$
6:	**end if**
7:	**end do**

Table 4.3: Pseudo code for implementation of core failure in Fortran post processing.

5 | Verification of Sandwich Failure Criteria

This section presents the verification of the implemented face sheet wrinkling and shear crimping sandwich failure criteria in FPP. Three rectangular sandwich plates with different layups are used for verification. Throughout the chapter, the complexity of the layup and the loading increases gradually to ensure that the implementation can accommodate increasingly complex scenarios. The three models are referred to as single ply (SP), symmetric cross ply (CP), and antisymmetric angle ply (AP), characterized by the layup of the face sheets. The solutions generated from FPP are compared against those from ANSYS Composite PrepPost (ACP). Where applicable, comparison is also done with MUST and/or an analytical solution implemented in MATLAB. The analytical solution utilizes FSDT to create the constitutive matrices and evaluate stresses and strains. The failure criteria are assessed in MATLAB based on the FSDT constitutive modeling in Section 4.1 and the analytical stresses.

Firstly, the models and analysis setup are presented. This details the geometry of the sandwich plate, material parameters, boundary conditions, and analysis settings related to the program described in Chapter 3, as well as the factors for the sandwich failure criterion functions. Moreover, the mesh is given along with a mesh convergence study. Following this are the results from the SP, CP, and AP analyses. The chapter concludes by discussing the findings from all five verification cases.

5.1 Model & Analysis Setup

The sandwich plate model features four straight edges parallel to the global X-direction and Y-direction. The sandwich plate's width and length are $150[mm]$, and the total thickness is $t = 24[mm]$. The thickness of the core is $t_C = 20[mm]$ and the thickness of each face sheet is $t_{Fc} = t_{Fb} = 2[mm]$ for all layups. The geometry of the sandwich plate is visualized in Figure 5.1.

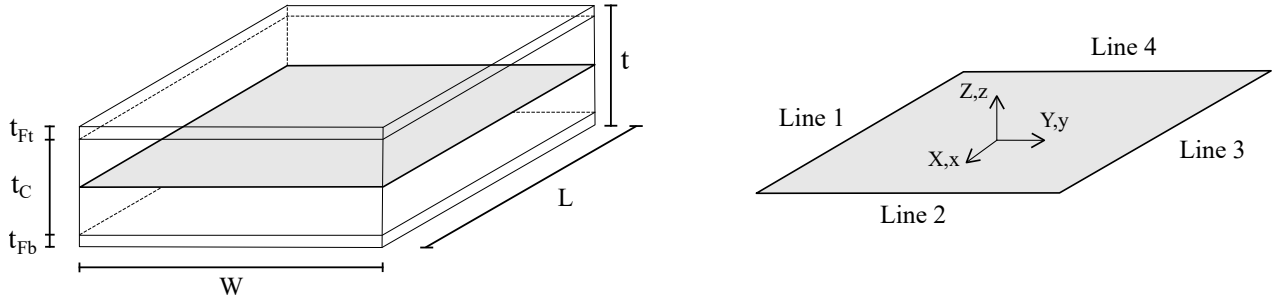

Figure 5.1: Sandwich plate geometry and dimensions. X,Y,Z refers to the global coordinate system, and x,y,z to the element coordinate system.

The boundary conditions for the four load cases used in the verification examples are presented in Tables 5.1-5.4. The relevant load case will be specified as the analysis is presented.

Uniaxial	u_x	u_y	u_z	N_x	N_y
Line 1	-	0	0	-	-
Line 2	0	-	0	-	-
Line 3	-	-	0	-	-100
Line 4	-	*Coupled*	0	-	-

Table 5.1: Uniaxial compression in y-direction. N_y is in $[N/mm]$.

Uniaxial	u_x	u_y	u_z	N_x	N_y
Line 1	-	*Coupled*	0	-	-
Line 2	-	-	0	-100	-
Line 3	-	0	0	-	-
Line 4	0	-	0	-	-

Table 5.2: Uniaxial compression in x-direction. N_x is in $[N/mm]$.

Biaxial	u_x	u_y	u_z	N_x	N_y
Line 1	-	0	0	-	-
Line 2	-	-	0	-100	-
Line 3	-	-	0	-	-100
Line 4	0	-	0	-	-

Table 5.3: Biaxial compression. N_x and N_y are in $[N/mm]$.

Biaxial	u_x	u_y	u_z	N_x	N_y
Line 1	0	0	0	-	-
Line 2	-	-	0	-100	-
Line 3	-	-	0	-	-100
Line 4	0	0	0	-	-

Table 5.4: Biaxial compression with fixed edges. N_x and N_y are in $[N/mm]$.

Analysis Setup
The analytical solution in MATLAB assumes linear elasticity; therefore, the analysis in ACP and FPP is based on a linear static base analysis, as described for the linear buckling analysis in Section 2.2.3. A list of the analysis settings used for all analyses is found in Table 5.5. The non-linearity factors are disabled for the verification analyses.

NR-Analysis		**Failure Criteria**	
N_{max}	2	k_F	1
ζ_{pert}	$1 \cdot 10^{-5}$	k_C	1
λ^c	$7 \cdot 10^3$	Q	0.5

Table 5.5: Analysis settings. N_{max} is the maximum number of load steps, ζ_{pert} is the perturbation load factor, and λ^c is the critical eigenvalue for buckling analysis. k_F and k_C are the shear crimping factors related to equation (2.24)*, and Q relates to face sheet wrinkling in equation* (2.27)*.*

The material parameters for the GFRP and PET-foam used in the verification examples are provided in Table 5.6.

Parameter	**Unit**	**GFRP**	**PET**
E_1	$[MPa]$	38000	112
E_2	$[MPa]$	9000	112
E_3	$[MPa]$	9000	112
ν_{12}	$[-]$	0.28	0.40
ν_{23}	$[-]$	0.28	0.40
ν_{13}	$[-]$	0.28	0.40
G_{12}	$[MPa]$	3600	36
G_{23}	$[MPa]$	3600	36
G_{13}	$[MPa]$	3500	39

Table 5.6: Material parameters for GFRP and Kerdyn^{TM}150 PET foam from Gurit98m [Hermansen et al., 2025].

Mesh
The FE models consist of 225 layered linear shell elements, *SHELL181* [ANSYS, 2024c, p. 683-702]. The elements are formulated according to FSDT. Full integration with incompatible modes is used for higher accuracy in in-plane bending [ANSYS, 2024c, p. 691]. Mixed interpolation of tensorial components (MITC) is used to avoid out-of-plane shear locking[ANSYS, 2024e, p. 600]. Results are stored at the top, middle, and bottom of every layer, coincident with the integration points through the thickness of each layer. The element size was chosen based on an initial convergence study across all analyses in ACP to ensure a converged result. The convergence criterion is defined by the maximum inverse reserve factor changing less than 0.5% when the number of degrees of freedom increases by 100%. Convergence is verified for both face sheet wrinkling and shear crimping in ACP.

The convergence criterion is verified by ensuring $|a| < 5 \cdot 10^{-3}$ where a is the slope of a linear function $f(x) = ax$ and x is the number of nodes in the model. The nodes are changed from $x_1 = 256$ to $x_2 = 441$, and the resulting slope is presented in Table 5.7. The mesh is presented in Figure 5.2.

Case	Wrinkling	Crimping
SP	0.0	0.0
CP - LC 1	0.0	0.0
CP - LC 2	0.0	0.0
CP - LC 3	$1.135 \cdot 10^{-6}$	$-2.541 \cdot 10^{-6}$
AP	$2.335 \cdot 10^{-5}$	$1.551 \cdot 10^{-5}$

Table 5.7: Convergence data for all analyses.

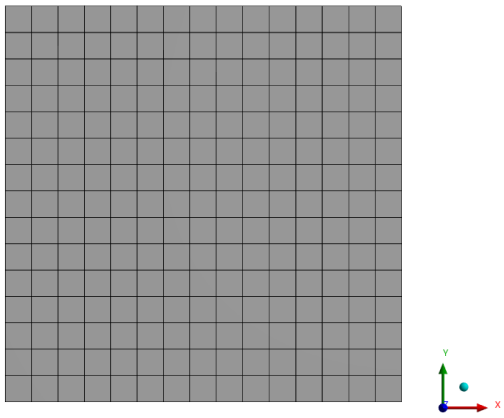

Figure 5.2: Mesh used in all verification analyses.

5.2 Single Ply

The SP layup consists of a single ply for each face sheet, with UD GFRP oriented along the element x-axis. In laminate shorthand notation, the layup is $(GFRP@0°, PET@0°, GFRP@0°)$. The SP model is subjected to uniaxial compression in the element y-direction with simple supports, and serves as the simplest test case. The load case is detailed in Table 5.1. For this case, intermediate results such as stress through the thickness and engineering constants in the $\xi\eta$-coordinate system are presented before evaluating the failure index. This step ensures that the modeling approach is consistent across different analysis tools and establishes a baseline of agreement before proceeding to more complex cases.

Structural Response

The SP model is analyzed analytically using MATLAB and numerically using ACP and FPP. The stress field is uniform across the plate, and the stress through the thickness is identical across the different analysis tools. The stress is presented in Figure 5.3.

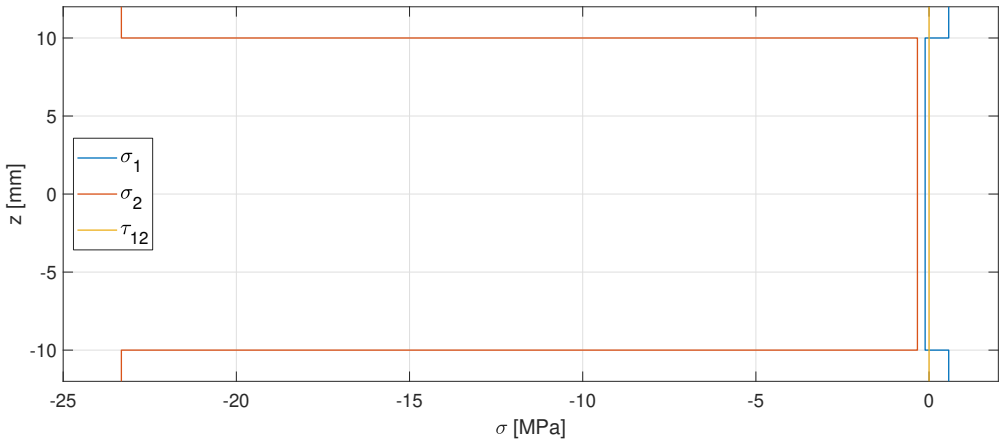

Figure 5.3: Single Ply, in-plane stress through the thickness in the material coordinate system.

The direction of maximum compression is oriented along the element's y-direction, as the model is loaded in uniaxial compression in the y-direction. Accordingly, the analytical MATLAB solution and FPP calculate $\theta_{\xi 1} = -90°$. In ACP, the principal stress direction can be visualized using the *Vector Principal Stress* tool in the *Static Structural* analysis system in *Ansys Workbench*. The principal directions for the face sheets are presented in Figure 5.4.

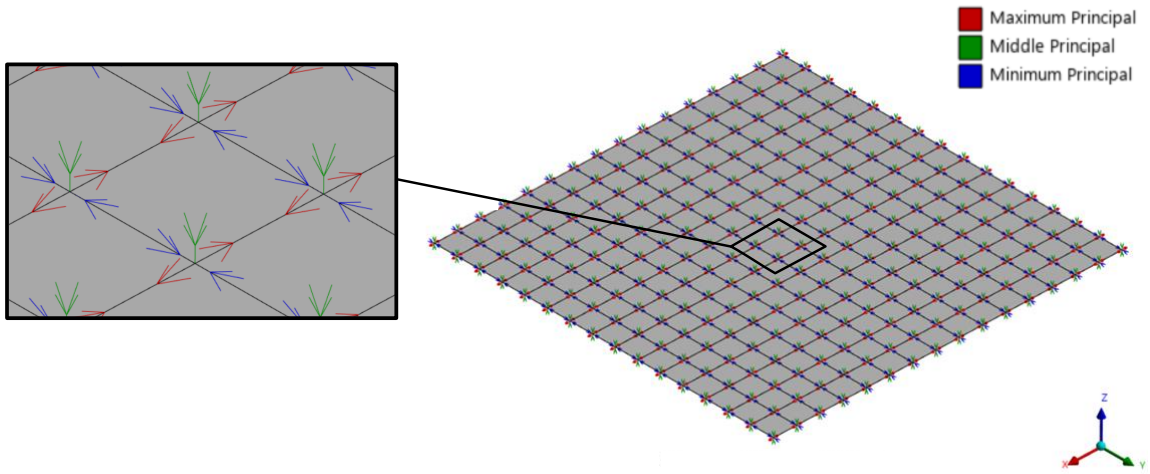

Figure 5.4: Principal directions for SP in layer one. These results are also representative of the principal directions in layer three.

Finally, the relevant engineering constants in the $\xi\eta$-coordinate system from MATLAB, FPP, and ACP are listed in Table 5.8. The engineering constants are extracted from ACP by modeling the face sheet and core separately with a local coordinate system coincident with the $\xi\eta$-system. The material constants align with the material parameters given for the 2-direction in Table 5.6.

	$E_{F,\xi}$	$E_{F,\eta}$	$\nu_{F,\xi\eta}$	$\nu_{F,\eta\xi}$	$G_{C,\xi\zeta}$	$E_{C,\eta\zeta}$
MATLAB	9000	38000	0.28	0.0663	36	39
FPP	9000	38000	0.28	0.0663	36	39
ACP	9000	38000	0.28	0.0663	36	39

Table 5.8: Laminate engineering constants in $\xi\eta$-coordinate system from FPP and MATLAB. The subscripts F and C refer to face sheet and core, respectively.

Failure Criteria

After confirming the structural response is equal across ACP, FPP, and MATLAB, the failure criteria are compared. The failure indices from ACP, FPP, and MATLAB for face sheet wrinkling and shear crimping are presented in Table 5.9. The percentage change in Table 5.9 is calculated using equation (5.1), yielding the % change in relation to 1, i.e., failure. The distribution of FPP face sheet wrinkling and shear crimping failure indices is uniform across the plate. The distribution is provided in Appendix E.

$$Change\ \% = \frac{max(f) - max(IRF)}{1} \cdot 100 \tag{5.1}$$

Failure Mode	**ACP**	**FPP**	**MATLAB**	**Change [%]**
Face sheet wrinkling	$IRF_w = 0.1400$	$f_w = 0.1400$	$f_w = 0.1400$	0.000%
Shear crimping	$IRF_{sc} = 0.1157$	$f_{sc} = 0.1157$	$f_{sc} = 0.1157$	0.000%

Table 5.9: Comparison of failure indices from ACP, FPP, and MATLAB with percentage change calculated with equation (5.1).

5.3 Symmetric Cross Ply

The CP model is subjected to three load cases: uniaxial compression in the element x-direction, simply supported biaxial compression, and biaxial compression with fixed edges. The layup of the CP model is $(GFRP@0°, GFRP@90°, GFRP@90°, GFRP@0°, \overline{PET@0°})_s$. The core is $t_C = 20[mm]$ and both face sheets are $t_{Ft} = t_{Fb} = 2[mm]$. Consequently, each face sheet lamina has a thickness of $0.5[mm]$.

Uniaxial Compression

The boundary conditions for the uniaxial compression load case are presented in Table 5.2. The magnitude of failure indices from FPP and ACP are presented in Table 5.10. The distribution is presented in Figure 5.5.

Failure Mode	ACP	FPP	Change [%]
Face sheet wrinkling	$IRF_w = 0.1033$	$f_w = 0.1033$	0.000%
Shear crimping	$IRF_{sc} = 0.1068$	$f_{sc} = 0.1068$	0.000%

Table 5.10: Comparison of failure indices from ACP and FPP with percentage change calculated with equation (5.1).

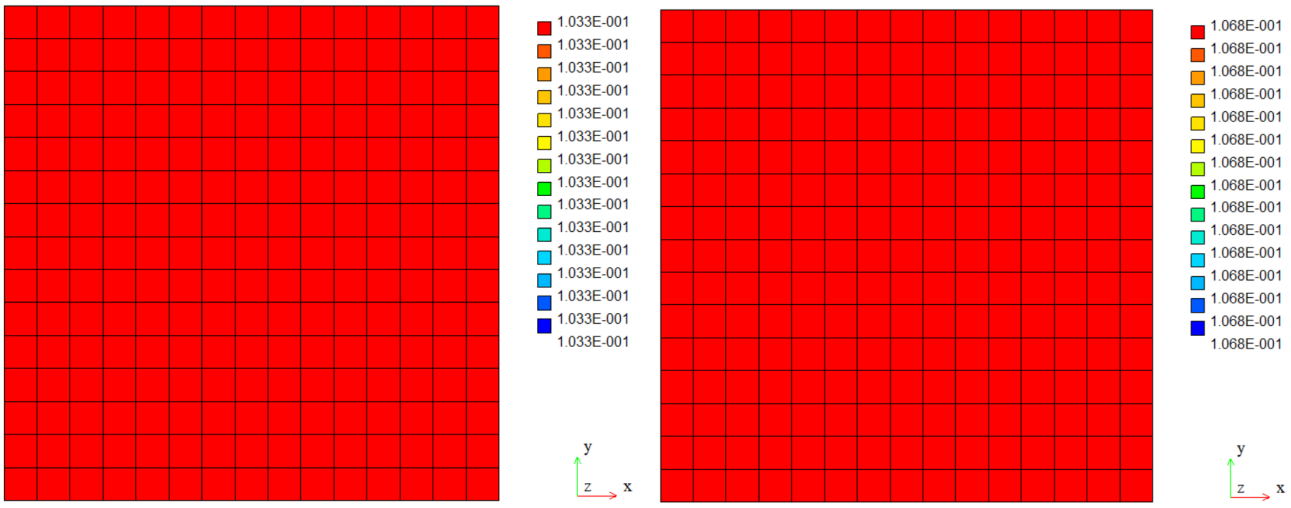

(a) Face sheet wrinkling. *(b) Shear crimping.*

Figure 5.5: Face sheet wrinkling and shear crimping failure for SP subjected to uniaxial compression.

Biaxial Compression

The boundary conditions for biaxial compression are given in Table 5.3. The magnitude of the failure indices from FPP and ACP are presented in Table 5.11. The distributions are presented in Figures 5.6 and 5.7.

Failure Mode	ACP	FPP	Change [%]
Face sheet wrinkling	$IRF_w = 0.1691..\ 0.1711$	$f_w = 0.1064$	-6.4700%
Shear crimping	$IRF_{sc} = 0.2222..\ 0.2226$	$f_{sc} = 0.2226$	-0.0000%

Table 5.11: Comparison of failure indices from ACP and FPP with percentage change calculated with equation (5.1).

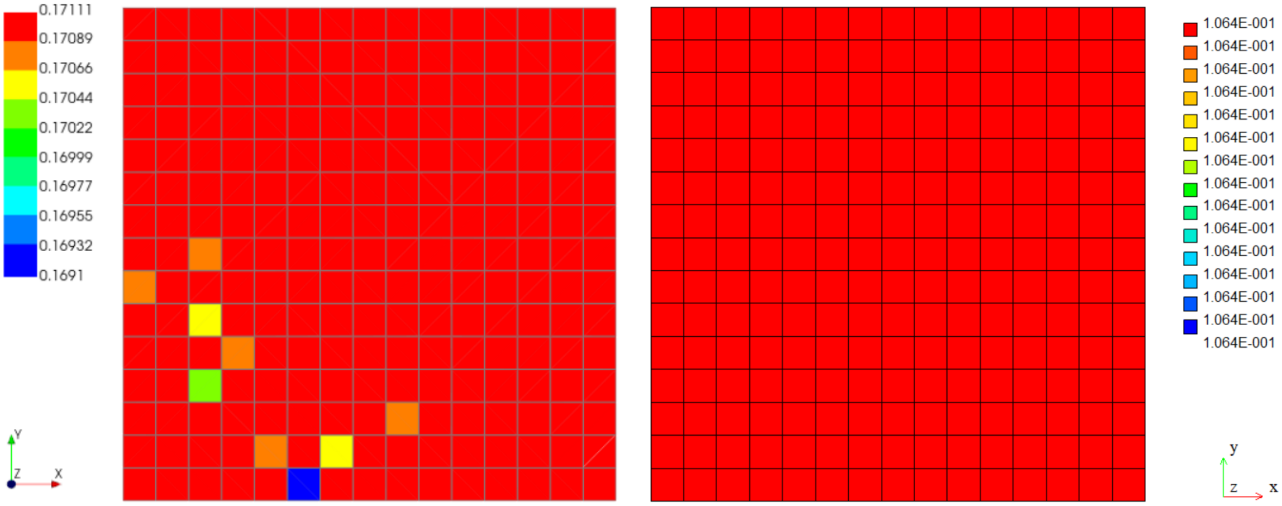

(a) ACP face sheet wrinkling. *(b) FPP face sheet wrinkling.*

Figure 5.6: ACP and FPP face sheet wrinkling failure indices for CP model subjected to biaxial compression.

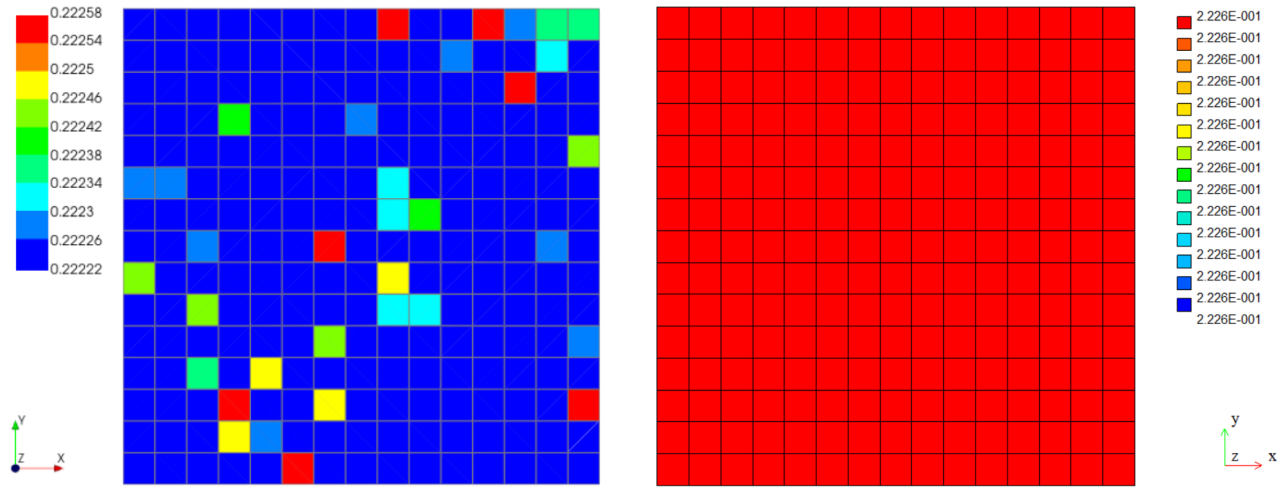

(a) ACP shear crimping. *(b) FPP shear crimping.*

Figure 5.7: ACP and FPP shear crimping failure indices for CP model subjected to biaxial compression.

The IRF solution from ACP shows a non-uniform distribution with IRF ranging between $IRF_{SC} =$ 0.22222-0.22258 and $IRF_w =$ 0.16910-0.17111, while FPP calculates a uniform FI distribution.

The source of the differences in failure indices for shear crimping and face sheet wrinkling is investigated in Appendix F. The non-uniform distribution observed in shear crimping can be attributed to the tolerances used for determining if small numbers are zero when calculating the principal directions, see Appendix F. In FPP, the tolerance is 10^{-8}, as presented in Section 4.1. In the investigation of face sheet wrinkling, intermediate quantities such as through-thickness stresses, principal stresses, and engineering constants in the $\xi\eta$-coordinate system are examined. Due to limited access to intermediate calculations in ACP, not all internal steps can be directly verified. As a result, some discrepancies remain unexplained. However, it is suspected to be due to the determination of the stress applied to the face sheets. This step is associated with ambiguity in the documentation, see equation (4.1).

Performing the analysis in MUST, the results are identical in magnitude and distribution to FPP. In MUST, face sheet wrinkling is calculated by averaging the element centroidal stress applied to each ply in the face sheets, following the same procedure described in equation (4.1). Moreover, MUST evaluates the sandwich failure criteria as failure criterion functions, rather than an IRFs.

Fixed Biaxial Loading

The boundary conditions used in the fixed biaxial compressive load case are presented in Table 5.4. The magnitude of the failure indices from FPP and ACP is presented in Table 5.12, and the distribution is presented in Figure 5.8.

Failure Mode	ACP	FPP	Change [%]
Face sheet wrinkling	$IRF_w = 0.0471..\ 0.1734$	$f_w = 0.0202..\ 0.1330$	-4.0400%
Shear crimping	$IRF_{sc} = 0.0621..\ 0.2431$	$f_{sc} = 0.0330..\ 0.2351$	-0.8000%

Table 5.12: Comparison of failure indices from ACP and FPP with percentage change calculated with equation (5.1).

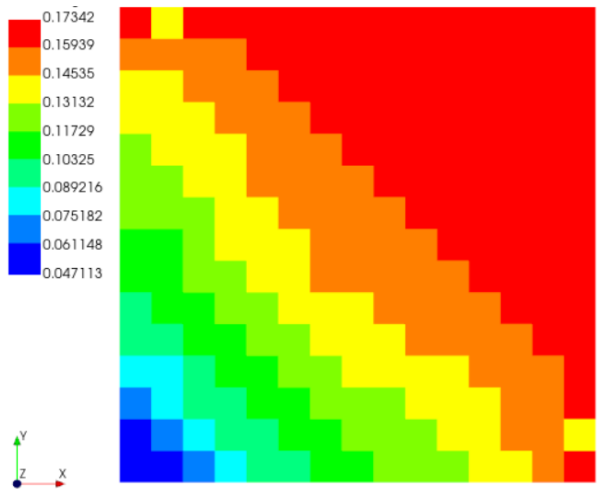

(a) ACP face sheet wrinkling.

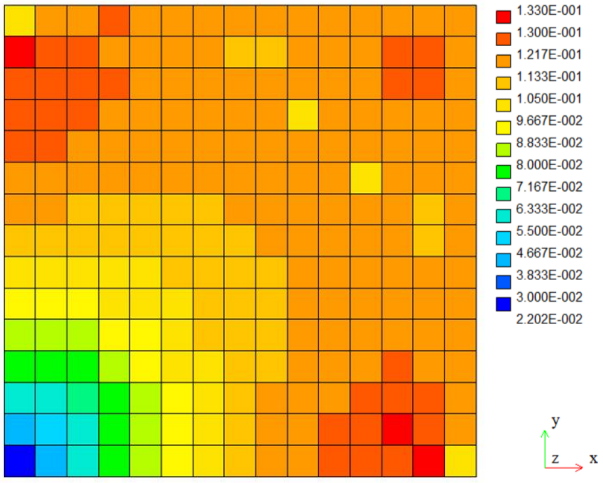

(b) FPP face sheet wrinkling.

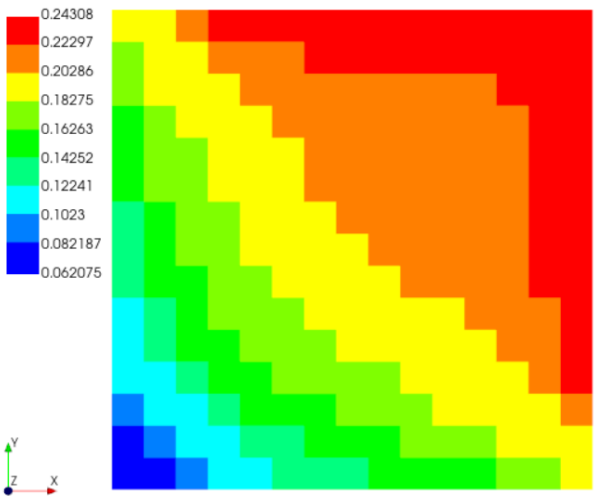

(c) ACP shear crimping.

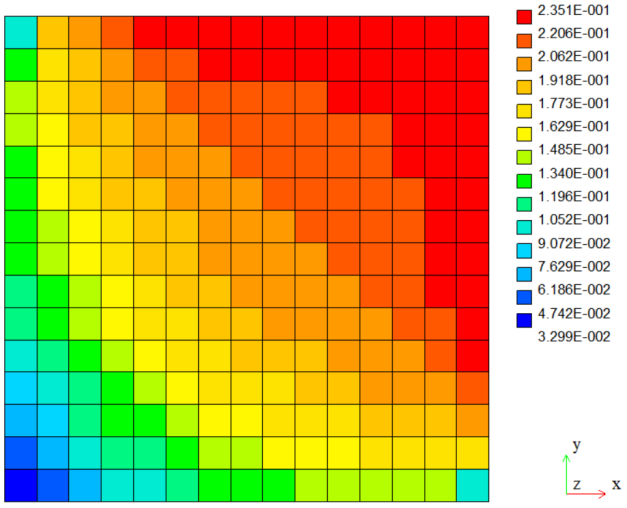

(d) FPP shear crimping.

Figure 5.8: ACP and FPP shear crimping and face sheet wrinkling failure indices for the CP model subjected to biaxial compression with fixed edges.

Discrepancies are observed in the distribution and magnitude of the face sheet wrinkling failure indices. For shear crimping, the distribution is similar. However, the magnitude is lower for FPP. These discrepancies warrant further investigation. This analysis is also performed in the full MUST program in order to compare results. The nodal displacements of the middle surface are compared between ACP, APDL, and MUST in Figure 5.9.

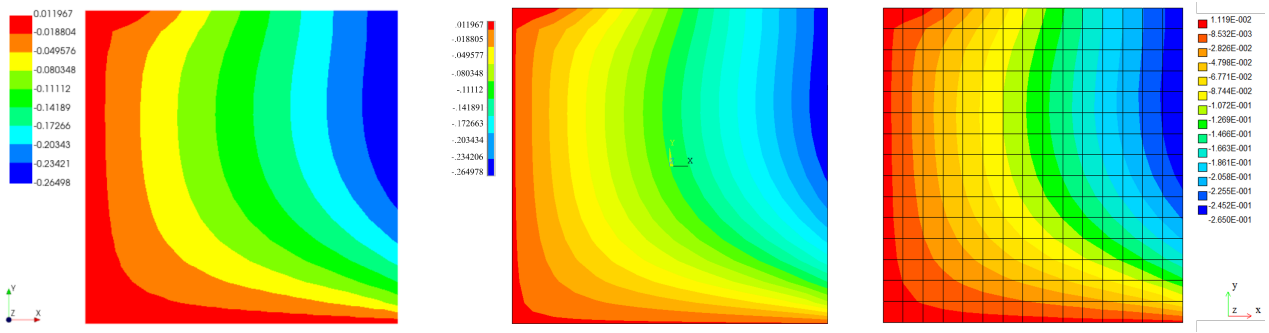

(a) Nodal displacements of middle surface calculated and visualized in ACP.

(b) Nodal displacements of middle surface calculated and visualized in APDL.

(c) Nodal displacements of the middle surface calculated in MUST.

Figure 5.9: Comparison of nodal displacements between ACP, APDL, and MUST.

The distribution and magnitude of the nodal displacements match across the different analysis tools. Similarly, the stresses are equal between ACP and FPP. The distribution of the failure criterion function for face sheet wrinkling and shear crimping calculated in MUST is presented in Figure 5.10.

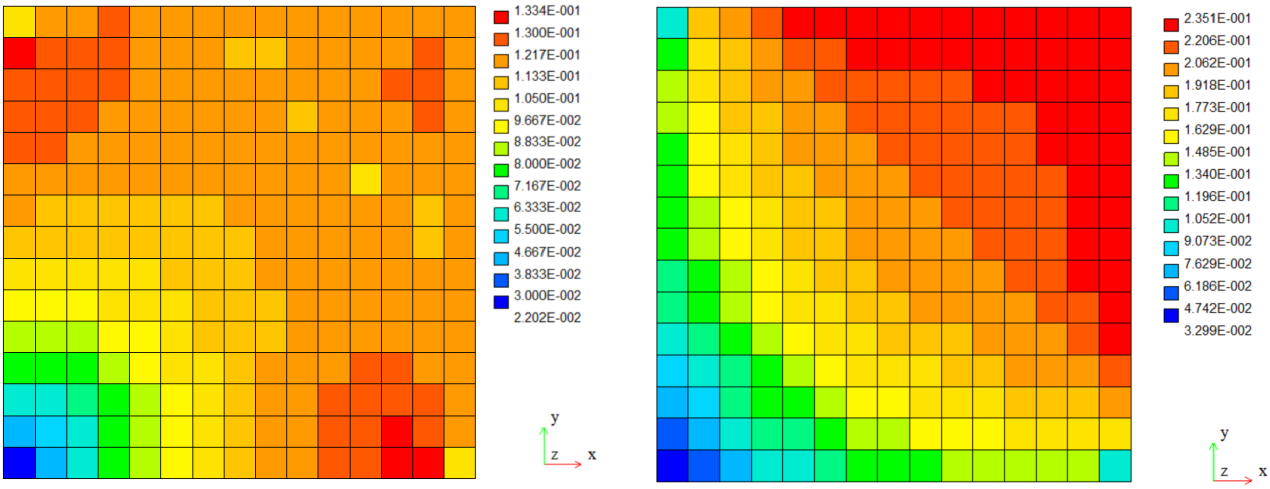

(a) Face sheet wrinkling.

(b) Shear crimping.

Figure 5.10: Face sheet wrinkling and shear crimping calculated in MUST.

A comparable magnitude and distribution are observed between MUST and FPP. The percentage change of the maximum failure index is $(0.1330 - 0.1334)/1 \cdot 100 = -0.04\%$ for face sheet wrinkling. The constitutive modeling is identical between MUST and FPP, so the difference is suspected to stem from the element stresses. In MUST, the element stress is evaluated in the center of each element, which results in slightly different element stresses near the fixed boundaries compared with the element stresses extracted from APDL.

5.4 Antisymmetric Angle Ply

The previous two layups feature symmetric face sheets with no bending-extension coupling. An antisymmetric angle ply with few lamina is an extreme case of bending-extension coupling [Jones, 1999, p. 217]. The boundary conditions are identical to the SP analysis, presented in Table 5.1. The magnitude of the failure indices from FPP and ACP is presented in Table 5.13. The distribution of face sheet wrinkling and shear crimping failure indices is presented in Figure 5.8.

Failure Mode	**ACP**	**FPP**	**Change [%]**
Face sheet wrinkling	$IRF_w = 0.1141..\ 0.1144$	$f_w = 0.1244..\ 0.1246$	1.0500%
Shear crimping	$IRF_{sc} = 0.1068..\ 0.1069$	$f_{sc} = 0.1068$	-0.0100%

Table 5.13: Comparison of failure indices from ACP and FPP with percentage change calculated with equation (5.1).

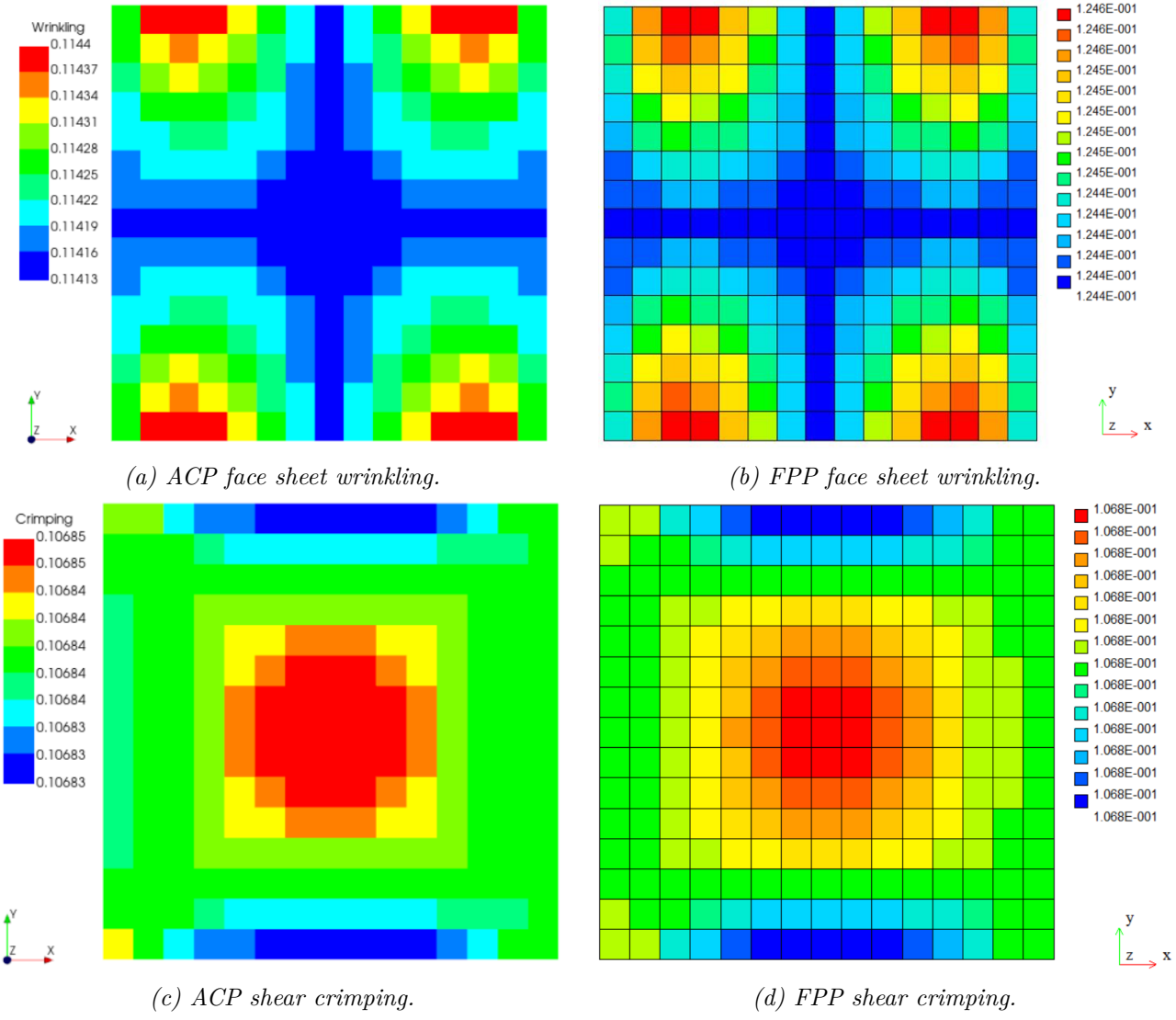

(a) ACP face sheet wrinkling.

(b) FPP face sheet wrinkling.

(c) ACP shear crimping.

(d) FPP shear crimping.

Figure 5.11: ACP and FPP shear crimping and face sheet wrinkling failure indices for the AP model subjected to uniaxial compression.

The distribution of both shear crimping and face sheet wrinkling is comparable between ACP and FPP. A difference in magnitude is observed for face sheet wrinkling. The stresses are equal between FPP and ACP, as observed in the other verification analyses. Agreement is observed when comparing face sheet wrinkling for MUST and FPP in Figure 5.12.

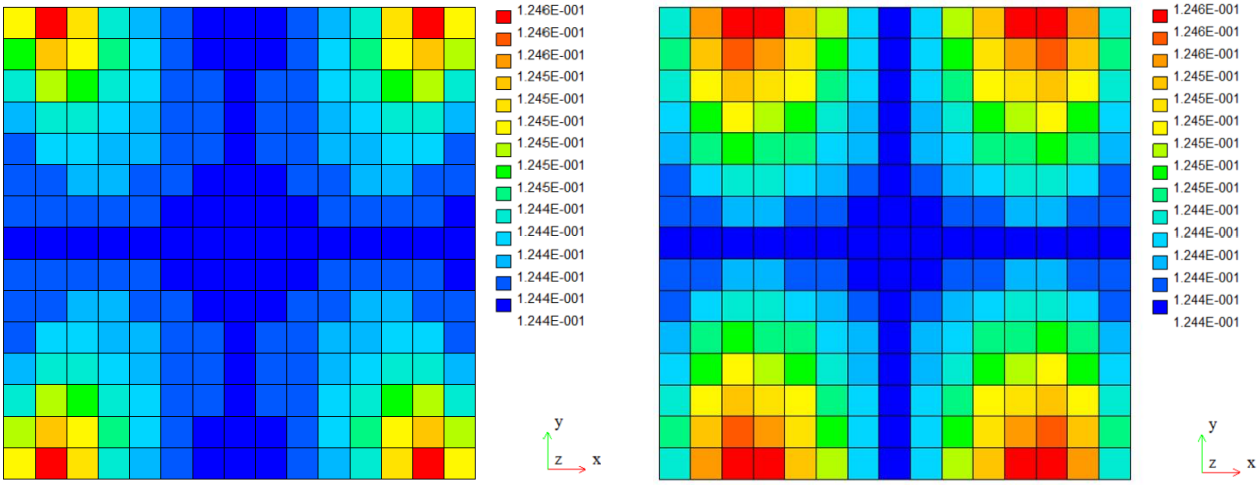

(a) Face sheet wrinkling calculated in MUST. *(b) Face sheet wrinkling calculated in FPP.*

Figure 5.12: Face sheet wrinkling failure criterion function calculated using MUST and FPP.

5.5 Discussion of Verification

This chapter presented the results of five verification analyses. The simple SP analysis compared the analytical solution based on FSDT, the numerical solution in ACP, and the implemented FPP based on APDL results. The stresses through the thickness, laminate engineering constants in the $\xi\eta$-coordinate system, and the failure indices were identical across all analysis tools. The SP analysis verified the general data handling, 90° rotation of material parameters, and ability to represent identical analyses across different analysis tools.

The CP model increased the complexity by introducing multiple lamina in the face sheets. The CP model under uniaxial compression verified the constitutive modeling with multiple lamina in the face sheets. Additionally, with the most compressive direction tested for both x and y, the association of the 2$^{\text{nd}}$ principal stress and the principal angle is verified for the case with zero shear stress and a nonzero denominator in equation (4.3).

The CP model under biaxial compression revealed a change of -6.4700% for face sheet wrinkling between the maximum FI from ACP to FPP. However, FPP and MUST showed identical results. ACP yielded a non-uniform result for shear crimping and face sheet wrinkling with IRF ranging between $IRF_w = 0.16910\text{-}0.17111$ and $IRF_{sc} = 0.22222\text{-}0.22258$ respectively. On the contrary, FPP showed a uniform distribution, which is expected for the simply supported biaxial load case. For shear crimping, the non-uniformity was determined to be attributed to the handling of small stresses when calculating the principal directions, as shown in Appendix F.

Additionally, the source of the discrepancy in face sheet wrinkling was investigated further in Appendix F. Intermediate results were compared across analysis tools. The stress through the thickness was verified against the analytical solution in MATLAB. The principal stress and direction were verified across FPP, ACP, and MATLAB. The elastic constants matched between ACP and FPP. No discrepancy was observed across these quantities. It is not possible to extract the stress acting on the face sheet in ACP, so this was not compared. The stress at the integration points for all elements

was compared with the averaged centroidal element stresses, based on a statement about the IRF evaluation in [ANSYS, a]. The integration point stress was investigated to determine if this was the source of the discrepancy between ACP and FPP. However, as expected, all integration points and the averaged centroidal values featured identical stress results. A final test was performed under the assumption that the stress state of an integration point was used as the stress applied to the face sheet. However, evaluating this stress state revealed a failure index of $f_w = 0.1597$. This failure index is different from the magnitude calculated in ACP.

Biaxial compression with fixed edges applied to the CP model revealed a change of -4.04% for face sheet wrinkling and 0.80% for shear crimping between ACP and FPP. Comparing FPP with MUST revealed almost identical failure indices, with the largest discrepancy in the magnitude of f_w of -0.04%. The AP analysis was associated with a change of 1.05% for face sheet wrinkling and -0.01% for shear crimping between ACP and FPP. However, identical results were observed between MUST and FPP. Based on the presented results, the discrepancies between ACP and FPP are thought to stem from a difference in the determination of stress applied to the face sheets and the subsequent calculation of principal stresses and principal directions. The user has limited access to these intermediate quantities in ACP, making further verification challenging.

In summary, the verification chapter has demonstrated that the implemented sandwich failure criteria in FPP produce results consistent with an analytical solution in MATLAB and MUST across various layup configurations and loading conditions. The strong agreement between FPP, MATLAB, and MUST supports the correctness of the implementation. The method is, therefore, considered sufficiently verified for use in the subsequent parametric study.

6 | Parametric Study

The parametric study aims to answer the problem statement by investigating the effect of varying structural parameters on the Gurit98m WTB model's composite failure and buckling behavior. Key structural parameters are identified by investigating which parameters most effectively enhance or degrade resilience to failure and buckling. The chapter first presents the Gurit98m WTB model, briefly outlining the geometry, materials, mesh, and load cases. Next, the methodology of the parametric study is described along with the analysis settings. The results of the parametric study are presented, followed by an overall comparison of parameters and a discussion of the results.

6.1 The Gurit98m model

Gurit98m is a 98-meter open-source horizontal-axis wind turbine blade model, jointly developed by Gurit Wind Systems A/S and Blade3 ApS [Hermansen et al., 2025]. Gurit98m is developed for the detailed structural design phase, where the outer geometry is fixed and the materials and layup may be modified [Hermansen et al., 2025]. The blade is designed based on the guidelines provided by DNV [DNV-GL, 2015, 2016]. Specifically, linear buckling is employed for the buckling analysis, and maximum stress and maximum strain are used for fiber and inter-fiber failure assessment. Three versions of the Gurit98m model are available on the GitHub repository, featuring one, two, and three shear webs [Hermansen et al., 2024]. The blade featuring one shear web is used in this parametric study. Additionally, Gurit98m is modeled with a prebend. The mesh used for the Gurit98m model is presented in Figure 6.1.

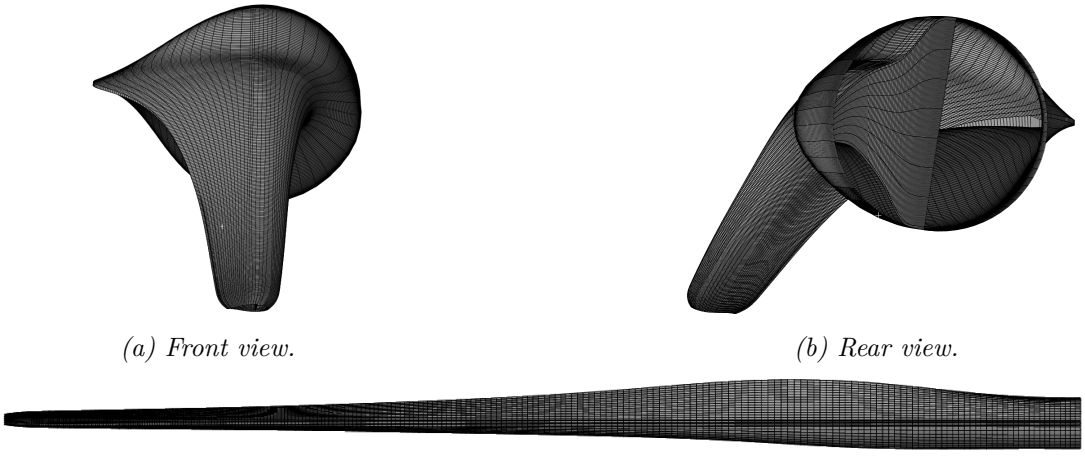

(a) Front view. *(b) Rear view.*

(c) Side view.

Figure 6.1: The Gurit98m WTB model mesh and geometry. The global coordinate system is located at the center of the root. The X-axis is positive from the pressure to the suction side. The Y-axis is positive from the leading to the trailing edge, and the Z-axis is oriented in the spanwise direction, orthogonal to the XY plane.

Gurit98m is meshed with a total of 20977 elements, consisting of 20208 four-node linear shell elements and 769 eight-node linear solid elements, named SHELL181 and SOLID185 in ANSYS, respectively. The solid elements are used to model the glued section of the trailing edge. The rest of the model is meshed using the linear SHELL181 elements. Linear shell elements are used instead of quadratic shell elements for computational efficiency [Hermansen et al., 2025]. Full integration with incompatible modes is included to enhance accuracy in modeling in-plane bending [ANSYS, 2024c, p. 691]. MITC prevents out-of-plane shear locking [ANSYS, 2024e, p. 600-601]. The x-axis for the element coordinate systems for the SHELL181 is oriented in the spanwise direction, positive towards the tip of the blade. The z-axis is positive towards the blade's center, and the y-axis is orthogonal to the xz-plane, referred to as the hoopwise direction. The element coordinate systems are visualized in Figure 6.2.

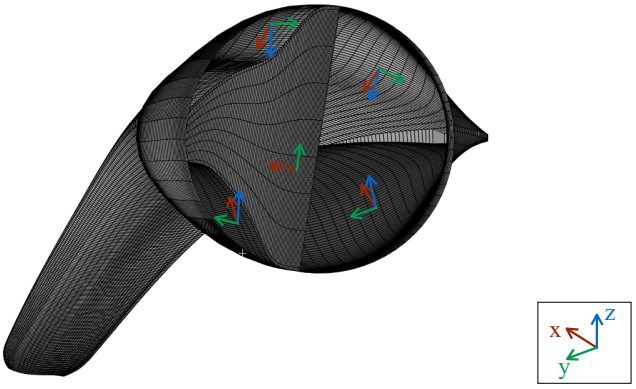

Figure 6.2: Element coordinate system on the Gurit98m, rear view.

Results are saved at each layer's top, middle, and bottom positions for the layered shell elements. The shell elements feature section offset, which describes the location of the nodes in relation to the shell thickness [ANSYS, 2024c, p. 1688]. The section offset extrudes the thickness towards the blade's center, ensuring the outer geometry remains unchanged.

Gurit98m includes E-Glass FRP and CFRP, epoxy adhesive, and PET foam [Hermansen et al., 2025]. GFRP and CFRP are used in UD non-crimp fabrics, where GFRP is also used for biaxial and triaxial NCFs. The biaxial and triaxial NCFs are created of two or three types of UD laminae, oriented as $-45°/+45°/0°$ [Hermansen et al., 2025]. The UD NCFs are primarily used for the spar caps, whereas biaxial and triaxial NCFs are utilized in the root to provide multi-directional strength. To account for metal inserts used for connecting the WTB to the hub, the thickness of the biaxial and triaxial layers is increased [Hermansen et al., 2025]. Recyclable PET foam is used as core material, which includes densities of 150$[kg/m^3]$ (PET150) and 250$[kg/m^3]$ (PET250). PET150 is the primary core material, whereas the higher density PET250 is solely used for the root section. Figure 6.3 presents the element thickness and core thickness distributions.

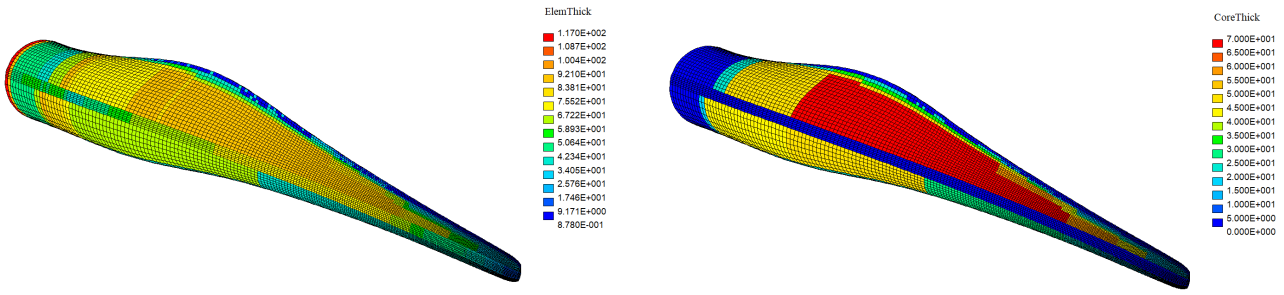

(a) Element thickness $[mm]$. *(b) Core thickness $[mm]$.*

Figure 6.3: Distribution of thickness on the Gurit98m model viewed from the pressure side.

The material and strength parameters are consistent with those used in [Hermansen et al., 2025], where the material parameters for the PET foams are based on Gurit Kerdyn [Gurit, f]. The remaining material parameters originally derive from ESAComp 2016 and ANSYS Workbench version R1 2024 [ANSYS, b]. The material parameters are listed in Table 6.1.

Property	**GFRP**	**CFRP**	**GFRP Biaxial**	**GFRP Triaxial**	**PET150**	**PET250**
E_1 [GPa]	38.000	125.000	24.000	26.472	0.112	0.244
E_2 [GPa]	9.000	8.000	24.000	10.073	0.112	0.244
ν_{12}[GPa]	0.280	0.300	0.110	0.430	0.400	0.400
G_{12}[GPa]	3.600	5.000	3.600	5.873	0.036	0.072
G_{23}[GPa]	3.600	3.080	3.600	3.500	0.036	0.072
G_{13}[GPa]	3.500	5.000	3.500	4.340	0.039	0.079
e_{1t}	0.0245	0.0143	0.0108	0.0204	-	-
e_{1c}	0.0150	0.0097	0.0108	0.0137	-	-
e_{2t}	0.0037	0.0050	0.0108	0.0058	-	-
e_{2c}	0.0122	0.0146	0.0108	0.0118	-	-
e_{12}	0.0194	0.0160	0.0166	0.0186	-	-
e_{23}	0.0120	0.0120	0.0100	0.0114	-	-
e_{13}	0.0194	0.0160	0.0100	0.0166	-	-
X_t [MPa]	-	-	-	-	1.63	2.61
X_c [MPa]	-	-	-	-	2.12	4.50
Y_t [MPa]	-	-	-	-	1.63	2.61
Y_c [MPa]	-	-	-	-	2.12	4.50
S_{12} [MPa]	-	-	-	-	1.26	1.76
S_{23} [MPa]	-	-	-	-	1.19	1.76
S_{13} [MPa]	-	-	-	-	1.19	1.76

Table 6.1: Materials used in Gurit98m, [Hermansen et al., 2025, p. 5].

Load cases

Along with the Gurit98m model, 12 load cases are provided in the GitHub repository [Hermansen et al., 2024]. These load cases include partial safety factors according to [DNV-GL, 2016] [Hermansen et al., 2025, p. 9]. These load cases represent design-driving extreme load cases, with LC 1, 4, 7, and 10 corresponding to extreme flapwise and edgewise loading, while the remaining cases involve multidirectional loading. The number and orientation of the load cases are consistent with DNV guidelines, which state that a wind turbine blade may be evaluated based on 12 representative load cases, where the envelope is equally distributed along all directions [DNV-GL, 2015, p. 15] [Hermansen et al., 2025]. The Gurit98m normalized load case envelope is presented in Figure 6.4. The loads are applied as nodal forces on the spar caps of the blade.

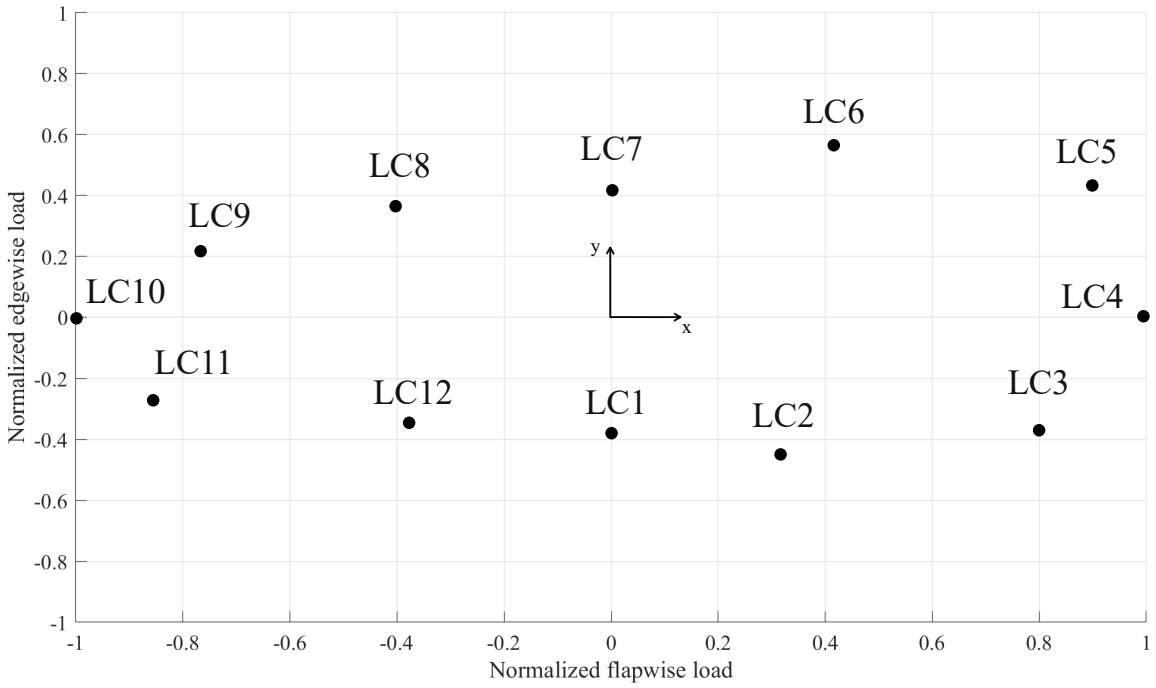

Figure 6.4: Gurit98m normalized load case envelope, inspired by Fig. 1 in [Hermansen et al., 2025].

6.2 Methodology

The study is conducted as a univariate parametric analysis, meaning a single parameter is changed at each analysis while all other parameters are kept at the base value. The benefit of performing a univariate analysis as opposed to a multivariate analysis is time and computational resources. A univariate analysis facilitates a more detailed study into each parameter and its isolated influence on failure indices and buckling. However, interaction between varying parameters cannot be evaluated. Laminate failure will be assessed using the maximum strain failure criterion. Puck's action-plane failure theory is formulated for UD lamina only, so it cannot be applied when the biaxial and triaxial non-crimp fabrics are represented as single, homogenised plies. If those NCFs were instead modeled as two or three distinct UD layers, each with the appropriate fiber orientation, the action-plane criterion would be applicable. The parameters and variations used in the parametric study are presented in Table 6.2.

Parameter	**Symbol**	**Variations**
Core thickness	t_C	-20% / -10% / $+10\%$ / $+20\%$
Transverse shear modulus	G_{13}	-50% / -25% / $+25\%$ / $+50\%$ / $+100\%$
Transverse shear modulus	G_{23}	-50% / -25% / $+25\%$ / $+50\%$ / $+100\%$

Table 6.2: Parameters and variations used in the parametric study. G_{13} and G_{23} refer to the transverse shear moduli of the core.

PET is softer and weaker than balsa wood. Therefore, the thickness or stiffness must be larger to enhance the buckling resistance. Considering the sandwich failure criteria in 2.3.3, the transverse shear stiffness of the core material is a central parameter. The thickness of the core is directly present in shear crimping, and indirectly in the core failure criterion via the stress and the assumption of linear elastic materials.

The variation range of the core thickness is selected to ensure a measurable change in max FI and γ between analyses, without drastically changing the blade's geometry. The variance of the transverse shear moduli G_{13} and G_{23} has been chosen based on the stiffness parameters of the lowest and largest densities for the Gurit Kerdyn PET foams, see [Gurit, e].

According to DNV, the load envelope may be defined as a bending moment distribution in the positive and negative flapwise and edgewise directions, as an alternative to 12 load cases [DNV-GL, 2015, p. 15]. Consequently, due to the computational cost and time required per load case, LCs 1, 4, 7, and 10 are selected. Additionally, the multidirectional LCs 5 and 6 are chosen as they yielded the smallest normalized buckling load factor of all 12 load cases in Fig. 6 in [Hermansen et al., 2025, p. 12].

As detailed in [Tønnesen and Christoffersen, 2025], a non-linear buckling analysis must be performed to assess the structural response and buckling behavior of a WTB. The non-linear buckling analysis presented in Chapter 3 and FPP presented in Chapter 4 are used as the analysis tool in the parametric study. The difference in in-plane strain non-linearity factor $\varepsilon^n_{\Delta,GNL}$ is chosen to detect local buckling, as it provided valuable insight into the distribution of non-linear bending for both the SGRE Student Blade and the Box-profile in [Tønnesen and Christoffersen, 2025, Ch. 4-5]. The truncation number is selected based on the value set for analyzing the SGRE student WTB model in [Tønnesen and Christoffersen, 2025, Ch. 5]. The analysis settings related to the non-linear buckling analysis are presented in Table 6.3.

Analysis setting	N_{max}	η	λ^c	j	ζ_{pert}	$\varepsilon^c_{\Delta,GNL}$	$\varepsilon_{\Delta,TN}$
Value	20	1	$6 \cdot 10^3$	4	$1 \cdot 10^{-5}$	$1 \cdot 10^{14}$	4

Table 6.3: Non-linear buckling analysis settings. N_{max} refers to the maximum number of load steps in the base analysis, η is the external load multiplier, ζ_{pert} is the perturbation load factor, and λ^c is the stopping criterion for the eigenvalue problem presented in Section 3. j is the number of eigenvalues calculated in the non-linear buckling analysis, $\varepsilon^c_{\Delta,GNL}$ is the critical non-linearity factor, and $\varepsilon_{\Delta,TN}$ is the truncation number, relating to the filter and truncation of the results used to calculate $\varepsilon^n_{\Delta,GNL}$.

6.3 Baseline Analysis

The baseline analysis is the analysis of the Gurit98m WTB model, in its original configuration. This analysis is a reference point for the influence of the different parameter variations. It will also be used to present the capabilities of the non-linear buckling analysis and FPP, in addition to giving a general understanding of the response of the blade with respect to failure and buckling. The history of the buckling load factor γ^n will be presented, along with the relevant maximum non-linearity factors $max\left(\varepsilon^n_{\Delta,GNL}\right)$ and distributions of $\varepsilon^{N_{max}}_{\Delta,GNL}$. Envelope plots will be given for each failure criterion, along with a combined envelope plot across all failure criteria. An envelope plot shows the maximum failure index per element across all load cases.

Buckling
The buckling load factor γ^n with respect to the load step factor α^n for all load cases and all load steps are presented in Figure 6.5.

The edgewise load cases, LC 1 and LC 7, are observed to have a larger γ^n than the mixed and flapwise load cases. The mixed LC 5 and the flapwise LC 4 exhibit the smallest γ^1. An increased buckling load is observed for all LCs with the increase of α^n, with the most significant being for LC 4, yielding $\gamma^{n \to N_{max}}_{LC4} = +32.35\%$. The mixed load cases, LC 5 and LC 6, are the most critical.

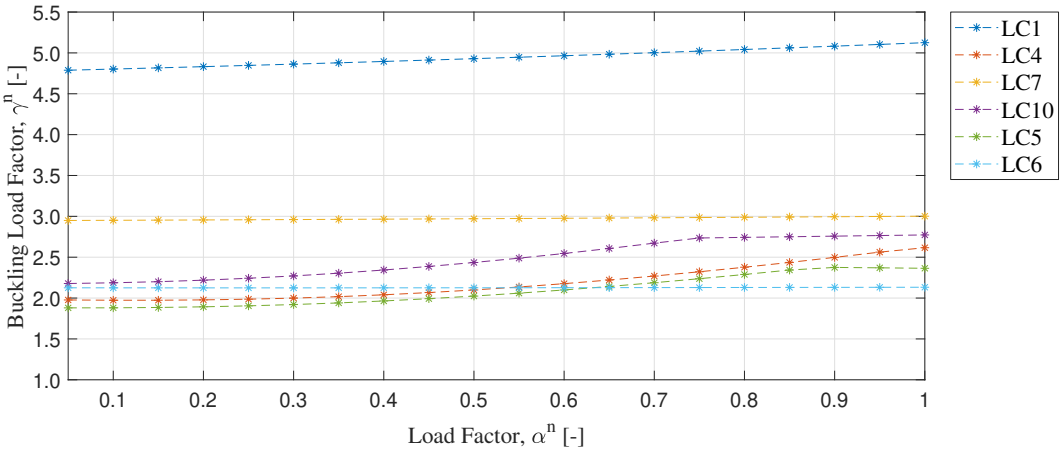

Figure 6.5: Calculated buckling load factor γ^n plotted against increasing load.

Since LC 6 is the most critical, its mode shapes are investigated and presented in Figure 6.6.

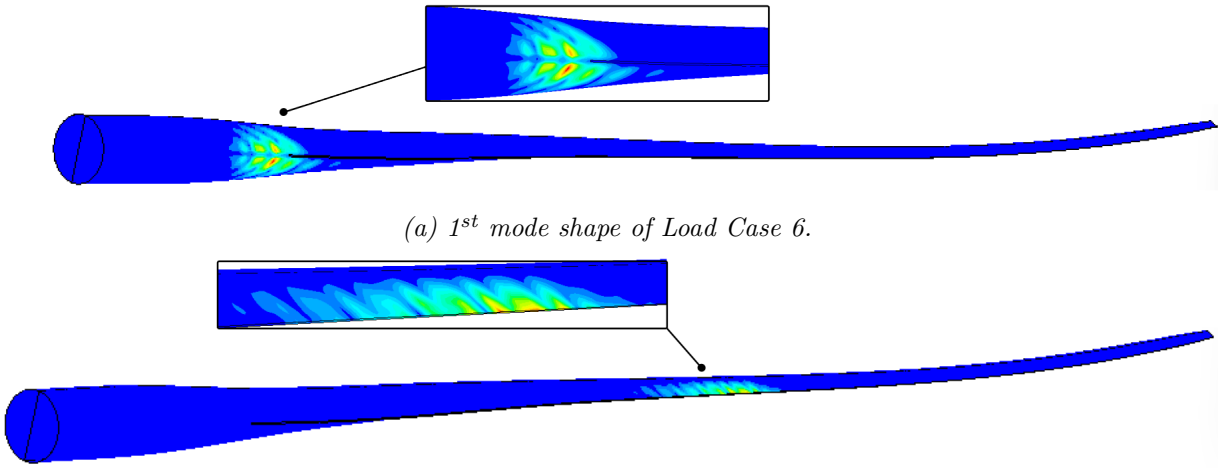

(a) 1st mode shape of Load Case 6.

(b) 3rd mode shape of Load Case 6.

Figure 6.6: 1st and 3rd mode shapes for LC 6 at $\alpha^{N_{max}} = 1.0$. The mode shapes are visualized on the deformed structure as a displacement vector sum.

The 1st mode shape is located near the blade's root at the TE suction and pressure side shells. The 2nd mode shape is in the same location as the 1st mode shape, while the 3rd and 4th mode shapes are located at the trailing edge, midway between the root and tip. None of the load cases bring the blade close to buckling, as evidenced by the large γ^n in Figure 6.5. Consequently, negligible non-linearity is observed in the magnitude of $\varepsilon^{N_{max}}_{\Delta,GNL}$. The maximum $\varepsilon^{N_{max}}_{\Delta,GNL}$for each element direction is given in Table 6.4.

	LC1	**LC4**	**LC7**	**LC10**	**LC5**	**LC6**
$max(\varepsilon^{N_{max}}_{\Delta x,GNL})$	1.000	1.114	1.000	1.114	1.114	1.055
$max(\varepsilon^{N_{max}}_{\Delta y,GNL})$	1.073	1.182	1.105	1.268	1.200	1.182
$max(\varepsilon^{N_{max}}_{\Delta xy,GNL})$	1.050	1.127	1.050	1.127	1.350	1.300

Table 6.4: Maximum difference in in-plane strain non-linearity factor at last load step for all load cases.

All $max(\varepsilon^{N_{max}}_{\Delta,GNL})$ are at or below 1.350, indicating a linear response compared with magnitudes up to $max(\varepsilon^{n}_{\Delta,GNL}) = 28$ observed in [Tønnesen and Christoffersen, 2025, Ch. 5]. The distribution of $\varepsilon^{N_{max}}_{\Delta,GNL}$ shows the region of the blade experiencing non-linear bending. The distribution of $\varepsilon^{N_{max}}_{\Delta y,GNL}$ is presented in Figure 6.6. The distribution highlights non-linear bending in the same region as the 1st mode shape. The distribution of $\varepsilon^{N_{max}}_{\Delta x,GNL}$ is scattered, with a few elements at the root having larger values than one. The scattered distribution indicates an unsuitable truncation and filtering. The distribution of the maximum values of the difference in in-plane shear strain non-linearity factors $\varepsilon^{N_{max}}_{\Delta xy,GNL}$ is mainly located at the leading edge 70$[m]$ from the root.

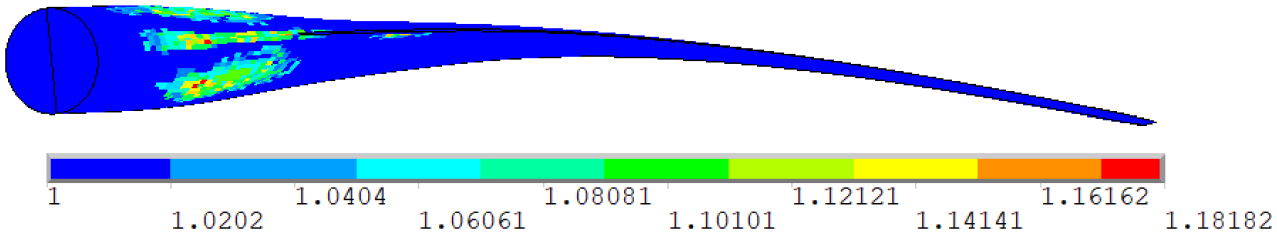

Figure 6.7: $\varepsilon^{N_{max}}_{\Delta y,GNL}$ for LC 6, load step 20. The $\varepsilon^{N_{max}}_{\Delta y,GNL}$ is visualized on the undeformed structure.

Failure

Following the buckling analysis, the distribution and magnitudes of the failure indices for face sheet wrinkling, shear crimping, core failure, and maximum strain are presented. The envelope plots for all failure criteria are shown in Figures 6.8 and 6.9. The highest failure index is observed along the trailing edge midway between the root and the tip for face sheet wrinkling, shear crimping, and maximum strain. The highest failure indices for core failure are observed at the root in the transition from laminate to sandwich layup. For all failure criteria, increased failure indices are observed at core thickness transitions, see Figure 6.3b. Figure 6.10 presents the combined envelope plots indicating the failure distribution. Generally, maximum strain is the active failure mode. However, shear crimping is active in regions of core thickness transition and along the trailing edge in the transition from laminate to sandwich.

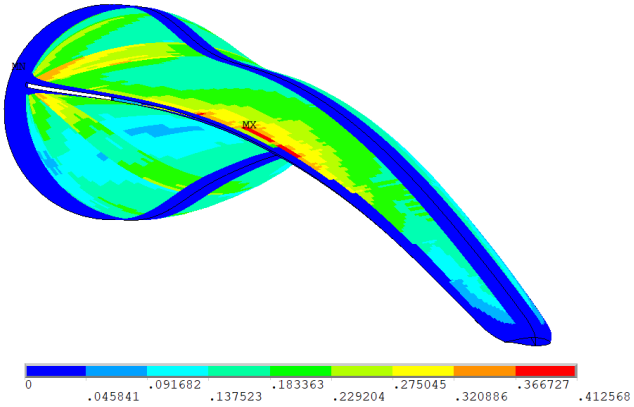

(a) Envelope plot for face sheet wrinkling f_w.

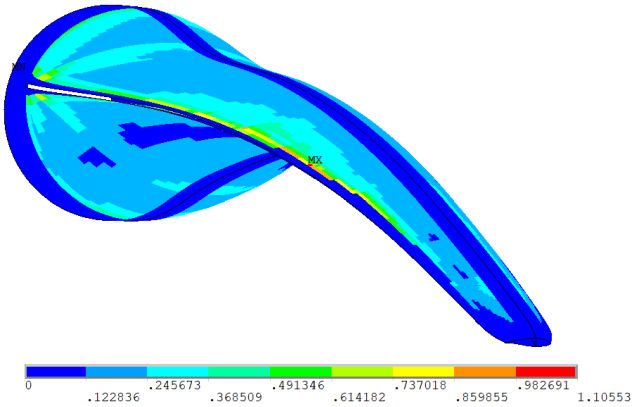

(b) Envelope plot for shear crimping f_{sc}.

Figure 6.8: Envelope plot of face sheet wrinkling and shear crimping for the baseline model. The envelope plots are shown on the underformed structure. Only SHELL181 elements are plotted.

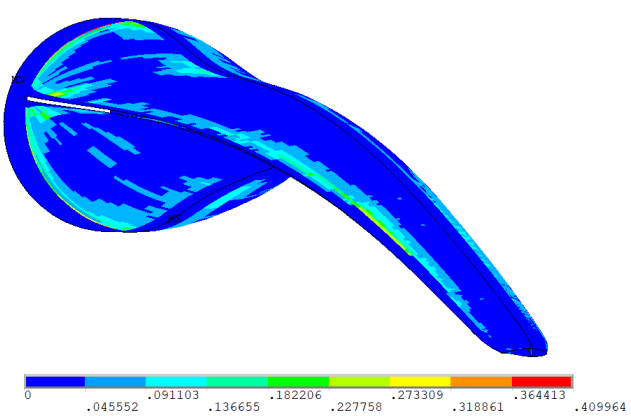

(a) Envelope plot for core failure f_{cf}.

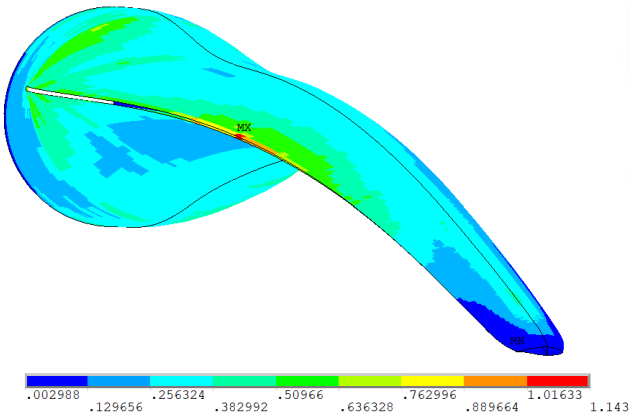

(b) Envelope plot for maximum strain f_e.

Figure 6.9: Envelope plot of core failure and maximum strain for the baseline model. The envelope plots are shown on the underformed structure. Only SHELL181 elements are plotted.

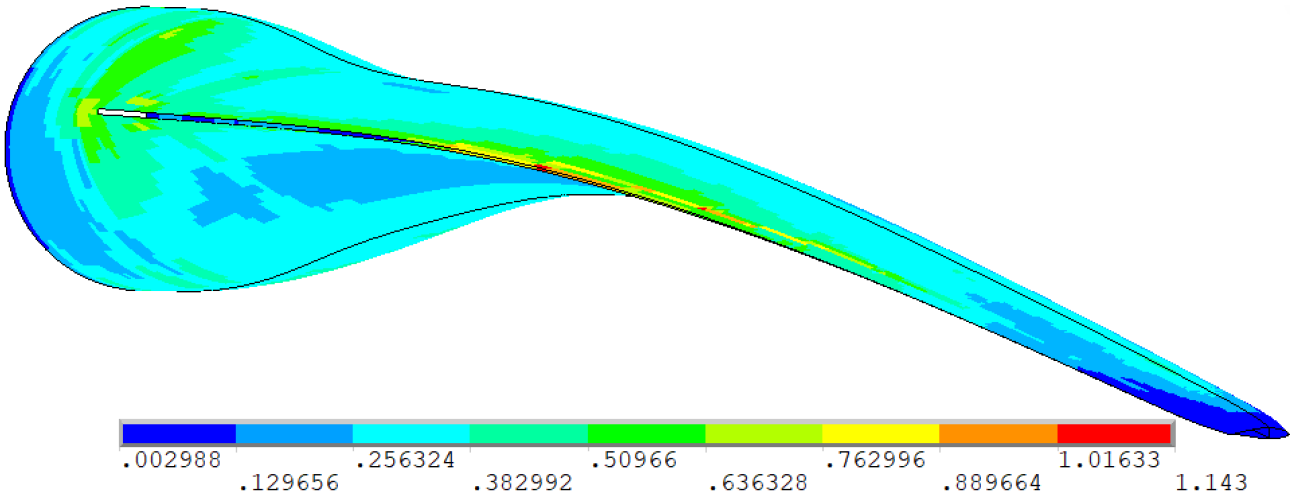

(a) Envelope plot for the baseline analysis. This shows the maximum FI across all failure criteria and LCs.

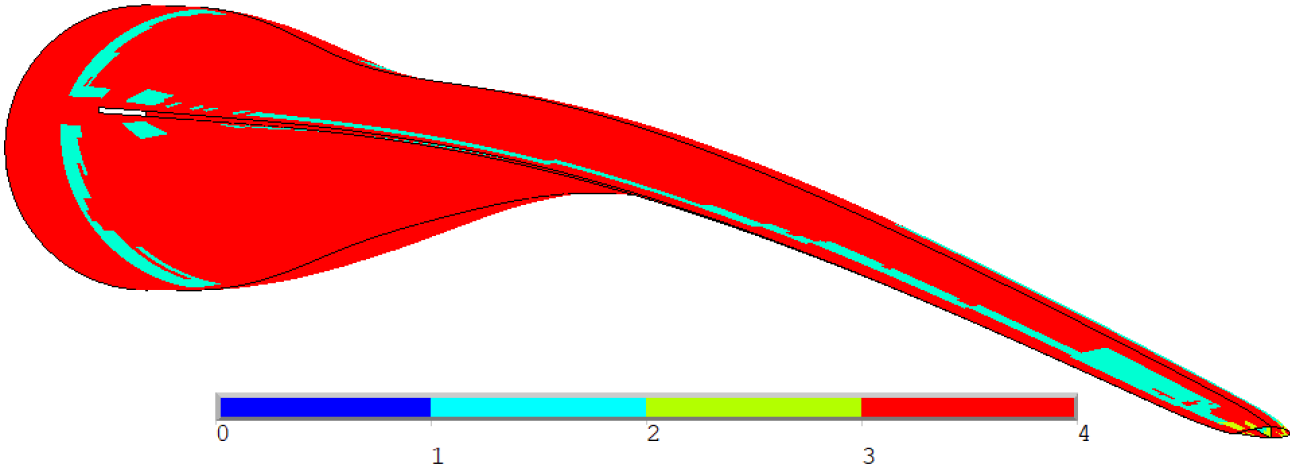

(b) Active failure mode for the baseline analysis.

Figure 6.10: Failure mode per element related to the maximum failure index in the envelope plot. The active failure mode uses the following notation: 1 [Blue] = face sheet wrinkling, 2 [Turquoise] = shear crimping, 3 [Green] = core failure, 4 [Red] = max strain.

6.4 Core Thickness

The first investigation in the univariate parametric study examines the influence of core material thickness across the entire blade. The thicknesses of both PET150 and PET250 are varied. The core thickness variations are defined in Table 6.2.

Buckling
The buckling load factor $\gamma^{N_{max}}$ for all thickness variations is presented in Figure 6.11. The figure is accompanied by Table 6.5 showing the percentage change in $\gamma^{N_{max}}$ compared with the baseline results.

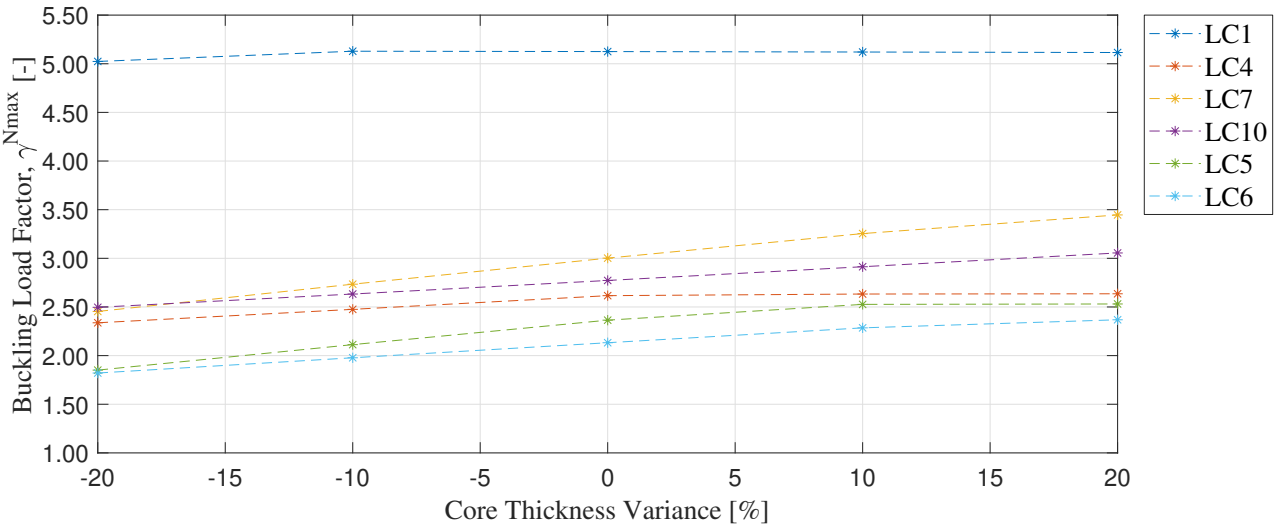

Figure 6.11: Buckling load factor $\gamma^{N_{max}}$ for varying core thickness at the last load step. Core thickness variation = 0% corresponds to the baseline results.

t_C	LC1	LC4	LC7	LC10	LC5	LC6
−20%	−1.9817	−10.6586	−18.2606	−9.9537	−21.7142	−14.6043
−10%	0.0700	−5.3771	−8.9170	−5.0282	−10.6353	−7.2482
+10%	−0.0894	0.6390	8.4111	5.0906	6.8642	7.1699
+20%	−0.1905	0.7379	14.7951	10.1973	7.0448	11.0626

Table 6.5: Percent change in $\gamma^{N_{max}}$ compared to the baseline results $t_C = 0\%$.

The smallest $\gamma^{N_{max}}$ across all load cases are observed at $t_C = -20\%$. The most significant decrease is observed for LC 5, at −21.7142%. A less significant change is observed in the positive direction with an increase of 0.306% from $t_C = +10\% \rightarrow +20\%$. The edgewise load case LC 1 has the largest $\gamma^{N_{max}}$ and is the least sensitive to the change in core thickness. Notably, the largest $\gamma^{N_{max}}$ is observed at $t_C = -10\%$ for LC 1, whereas the smallest $\gamma^{N_{max}}$ is at $t_c = -20\%$. The most significant increase in $\gamma^{N_{max}}$ is observed for the edgewise load case LC 7. LC 6 yields the smallest $\gamma^{N_{max}}$ for all thickness variations, making it the most critical load case regarding buckling. The effect on the mode shape of LC 6 is investigated by comparing the 1st mode shape in the outer ranges of the variation. The 1st mode shapes are visualized in Figure 6.12.

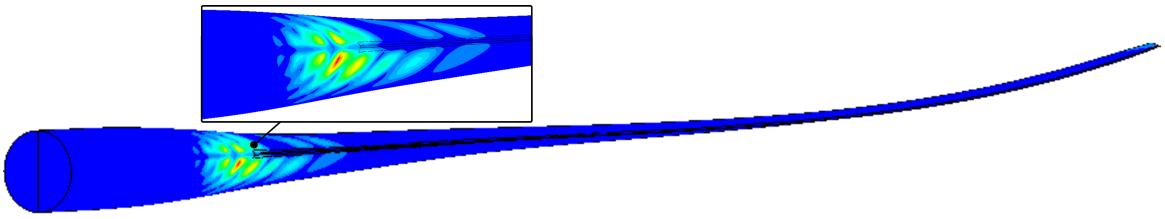

(a) 1st mode shape of Load Case 6 with $t_C = -20\%$.

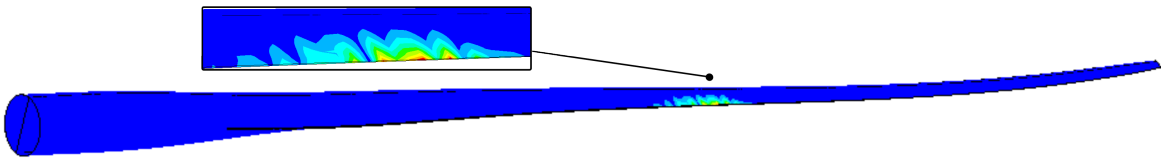

(b) 1st mode shape of Load Case 6 with $t_C = +20\%$.

Figure 6.12: The 1st mode shape of LC 6. Plotted on the deformed structure as a displacement vector sum.

Compared with the 1$^{\text{st}}$ mode shape of the baseline analysis seen in Figure 6.6, reducing the core thickness results in a larger buckling area in the same region at the beginning of the trailing edge. The 1$^{\text{st}}$ four mode shapes of the reduced thickness variation are located around the beginning of the trailing edge, with each mode shape slightly moving in the spanwise direction compared to the previous mode shape. Reducing the thickness eliminates the mode shape further up the blade, concentrated at the trailing edge, corresponding to the 3$^{\text{rd}}$ mode shape of the baseline analysis seen in Figure 6.6b. This mode shape is the 1$^{\text{st}}$ mode shape for $t_C = +20\%$. The 3$^{\text{rd}}$ mode shape of the $t_C = +20\%$ variation is similar to the 1$^{\text{st}}$ mode shape of the baseline analysis. Effectively, the distinctly different mode shapes in the baseline analysis and for $t_C = +20\%$ switch order.

Varying the core thickness does not significantly influence $\varepsilon^n_{\Delta,GNL}$. The distribution and magnitude of all non-linearity factors remain mostly the same as the baseline analysis. Generally, a thinner core results in more non-linearity, indicated by a larger magnitude and area with $\varepsilon^n_{\Delta,GNL} > 1$. Comparing the magnitude of the outer ranges of variance for LC 6 indicates the magnitude of change in the non-linearity factor. For $t_C = -20\%$ $max(\varepsilon^{N_{max}}_{\Delta y,GNL}) = 1.267$ and for $t_C = +20\%$ $max(\varepsilon^{N_{max}}_{\Delta y,GNL}) = 1.182$.

Failure

The effect of varying core thickness on failure is presented in the following. The maximum failure indices are presented for all variations of t_C in Figure 6.13.

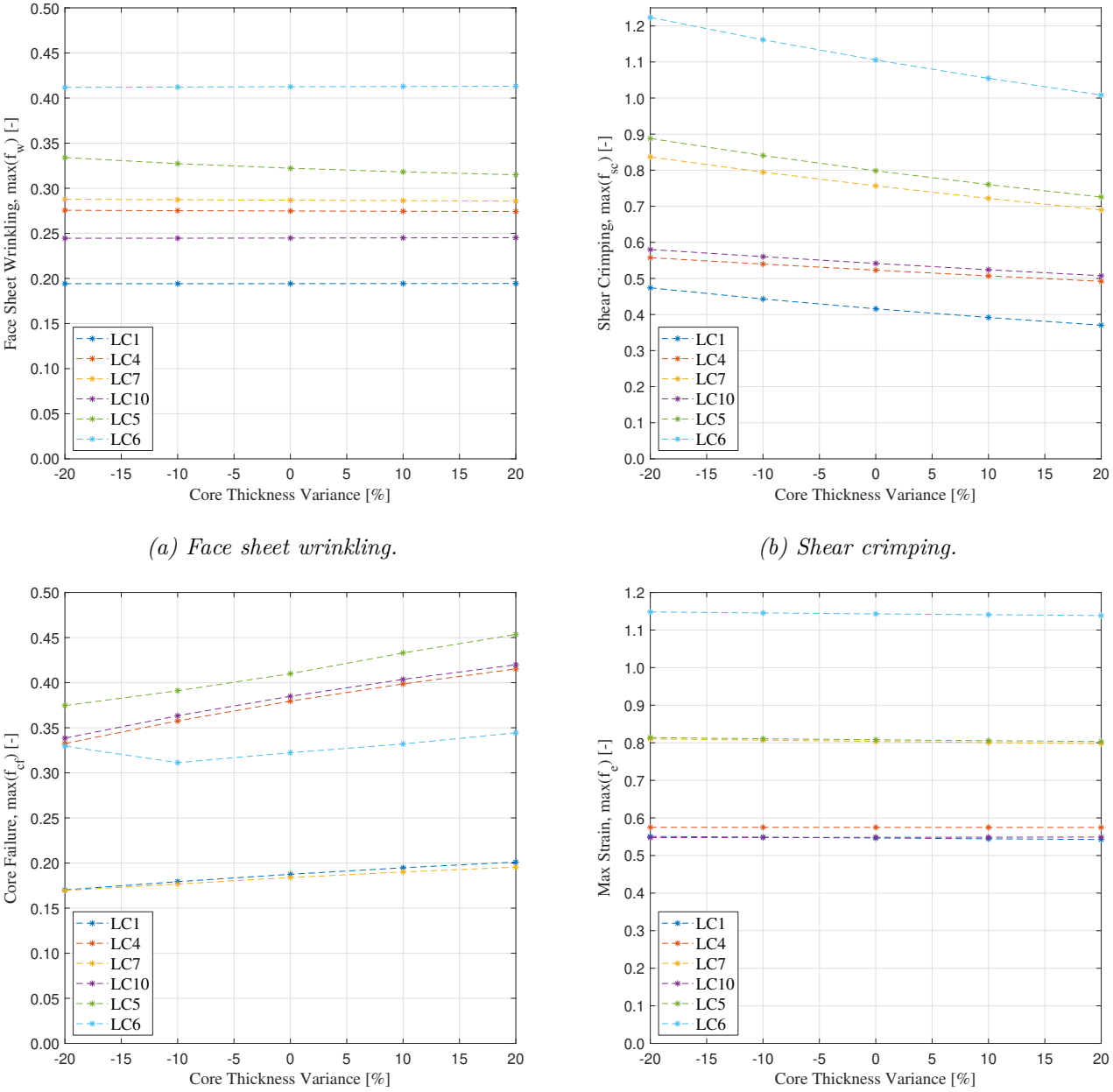

(a) Face sheet wrinkling.

(b) Shear crimping.

(c) Core failure.

(d) Maximum strain.

Figure 6.13: Parameter plots illustrating the effect of varying core thickness on failure criteria. The maximum failure index at the last load step is on the vertical axis.

The magnitude of $max(f_w)$ is generally unchanged except for LC 5, where a decrease of -0.019% is observed from $t_C = -20\% \rightarrow +20\%$. This aligns with theory, as face sheet wrinkling should be unaffected by the geometry [Zenkert, 2005, Sec. 6.9]. This is also apparent in equation (2.27), where the thickness is not used to formulate the wrinkling stress. Shear crimping $max(f_e)$ is more affected by the variation of core thickness, as is evident in equation (2.24). Generally, a thicker core results in a smaller $max(f_{sc})$. The inverse relation is observed for the core failure, where a thicker core leads to

a larger $max(f_{cf})$. Similar to face sheet wrinkling, the maximum strain criterion $max(f_e)$ is largely unaffected by variations in core thickness.

The effect of varying the core thickness on the failure distribution is visualized by plotting the maximum failure index for each failure criterion across all load cases. The distributions are plotted for the minimum and maximum ranges of t_C. The distribution of f_w and f_e is unchanged from the distributions seen in the baseline analysis. These plots are presented in Appendix G. The distribution of f_{sc} and f_{cf} is presented in Figure 6.14. The same overall distribution is apparent across $t_C = -20\% \rightarrow +20\%$. The largest f_{sc} are located along the trailing edge. For f_{cf}, the overall failure indices decrease as the thickness increases. However, the maximum values close to the laminate-to-sandwich layup transition increase.

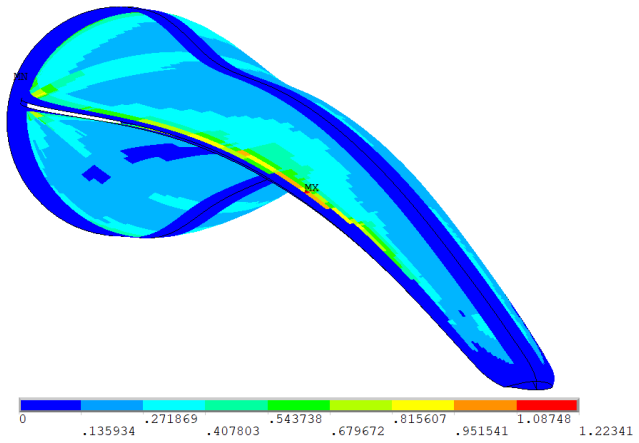

(a) Envelope plot for shear crimping for $t_C = -20\%$.

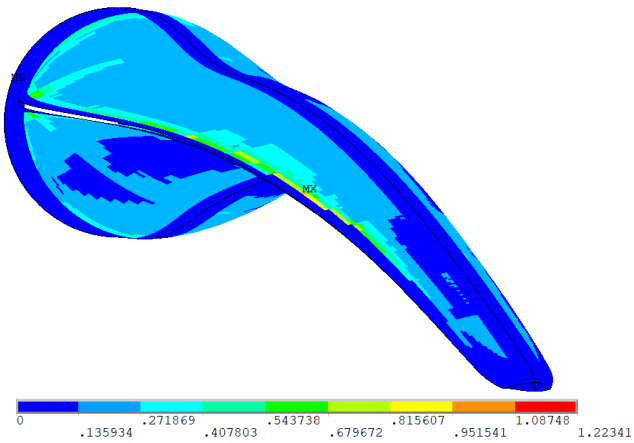

(b) Envelope plot for shear crimping for $t_C = +20\%$.

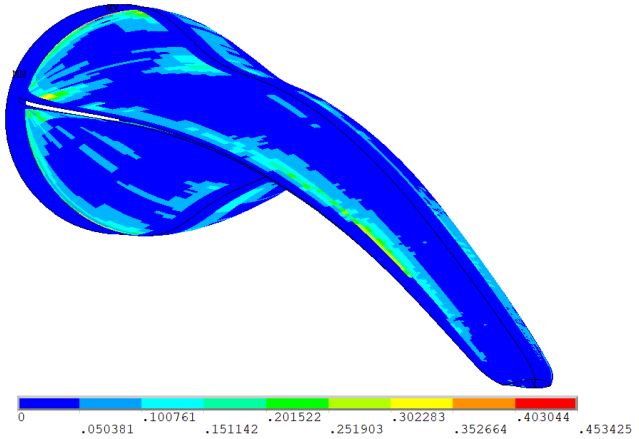

(c) Envelope plot for core failure for $t_C = -20\%$.

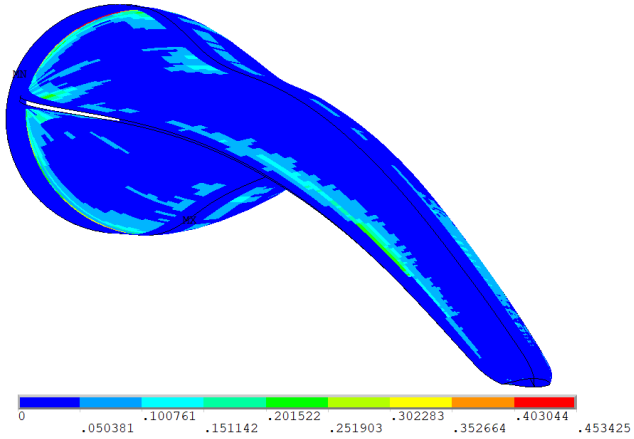

(d) Envelope plot for core failure for $t_C = +20\%$.

Figure 6.14: Envelope plot for shear crimping and core failure with varying core thickness $t_C = -20\%$ and $t_C = +20\%$. The envelope plots are shown on the underformed structure. Note that the color bar is kept constant across variations for each failure criterion. Only SHELL181 elements are plotted.

Comparing the overall effect of varying core thickness with the baseline analysis, envelope plots for the maximum failure index across all failure criteria and load cases are presented in Figure 6.15. Figures 6.15a and 6.15b show the failure index, where Figures 6.15c and 6.15d indicate the active failure modes. Maximum strain is the active failure mode throughout most of the blade, which is why the distribution remains mostly unchanged when varying the core thickness. In Figures 6.15c and 6.15d, shear crimping is the active failure mode in regions of thickness transition, with shear crimping being the active failure mode in a larger area for $t_C = -20\%$.

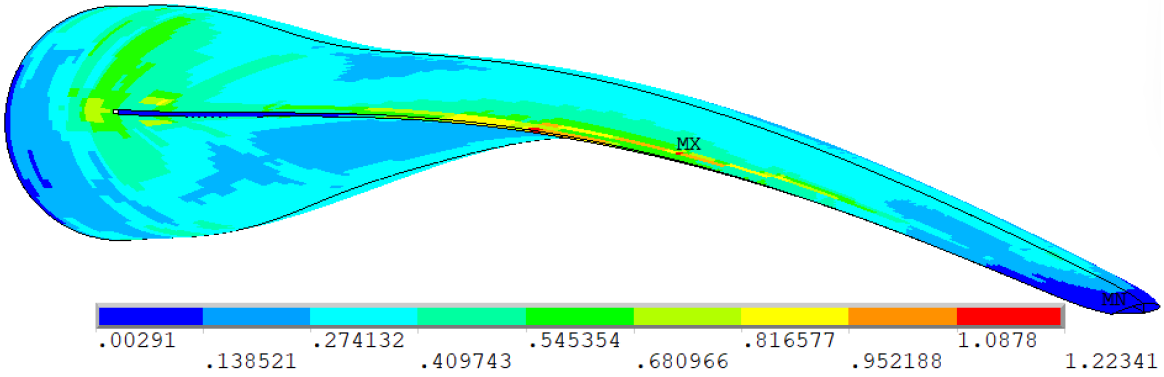

(a) Envelope plot for $t_C = -20\%$. This shows the maximum FI across all failure criteria and LCs.

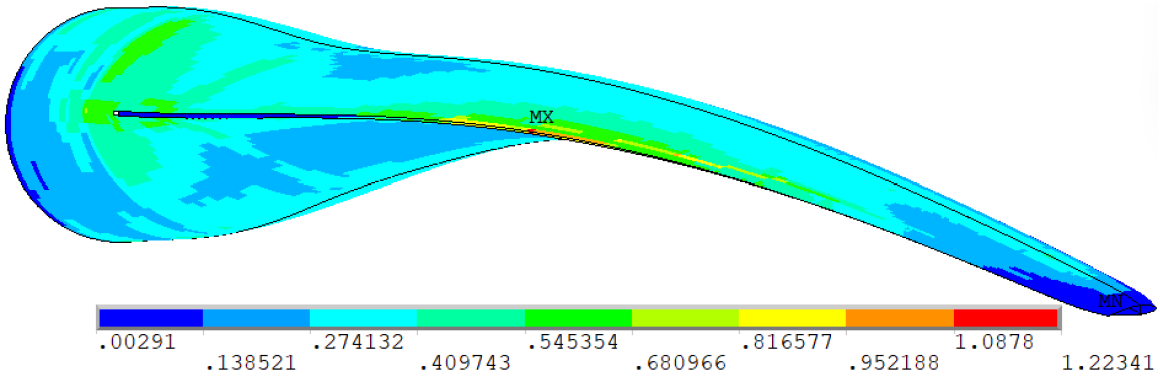

(b) Envelope plot for $t_C = +20\%$. This shows the maximum FI across all failure criteria and LCs.

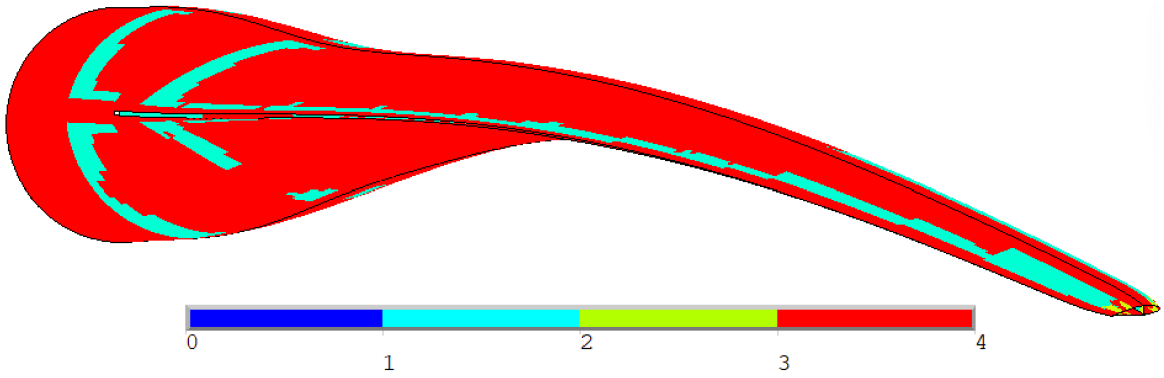

(c) Active failure mode for $t_C = -20\%$.

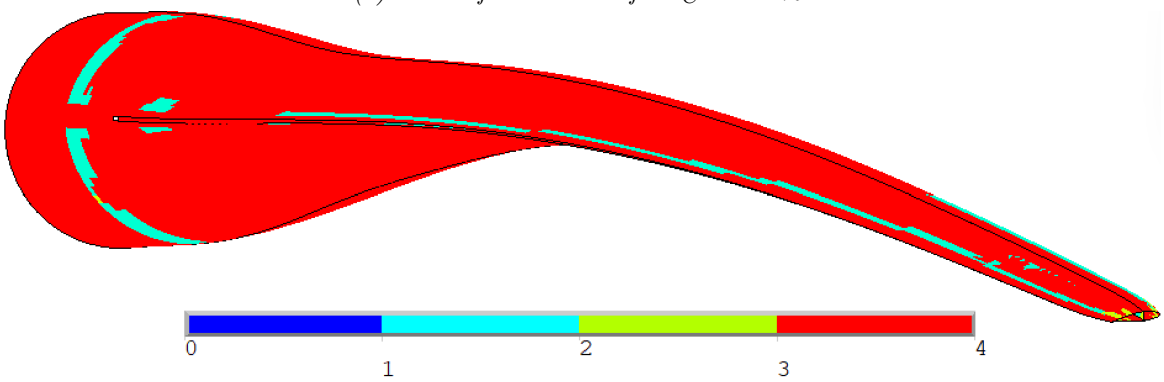

(d) Active failure mode for $t_C = +20\%$.

Figure 6.15: Failure mode per element related to the maximum failure index in the envelope plot. The active failure mode uses the following notation: 1 [Blue] = face sheet wrinkling, 2 [Turquoise] = shear crimping, 3 [Green] = core failure, 4 [Red] = max strain. Note that the color bar for the envelope plots is kept constant across variations.

6.5 Transverse Shear Modulus of Core

The second and final variations for the parametric study are the transverse shear moduli G_{13} and G_{23} of the core materials. All core materials have 0° rotation in relation to the element coordinate system, meaning G_{13} and G_{23} are the transverse shear moduli in the spanwise and hoopwise directions, respectively. Five variations are analyzed for both parameters. The increments for both moduli are found in Table 6.2. Following the same structure as the variation of t_C, the effect of varying the transverse shear stiffness on $\gamma^{N_{max}}$ and the 1st mode shape from the critical LC will be presented. Thereafter, the effect on the sandwich and max strain failure criteria will be given, followed by envelope plots providing insight into the failure distribution.

6.5.1 Transverse Shear Modulus G_{13}

The buckling load factor at the last load step $\gamma^{N_{max}}$ for each variance of shear modulus G_{13} is presented in Figure 6.16, accompanied by Table 6.6 showing the percentage change from the baseline analysis.

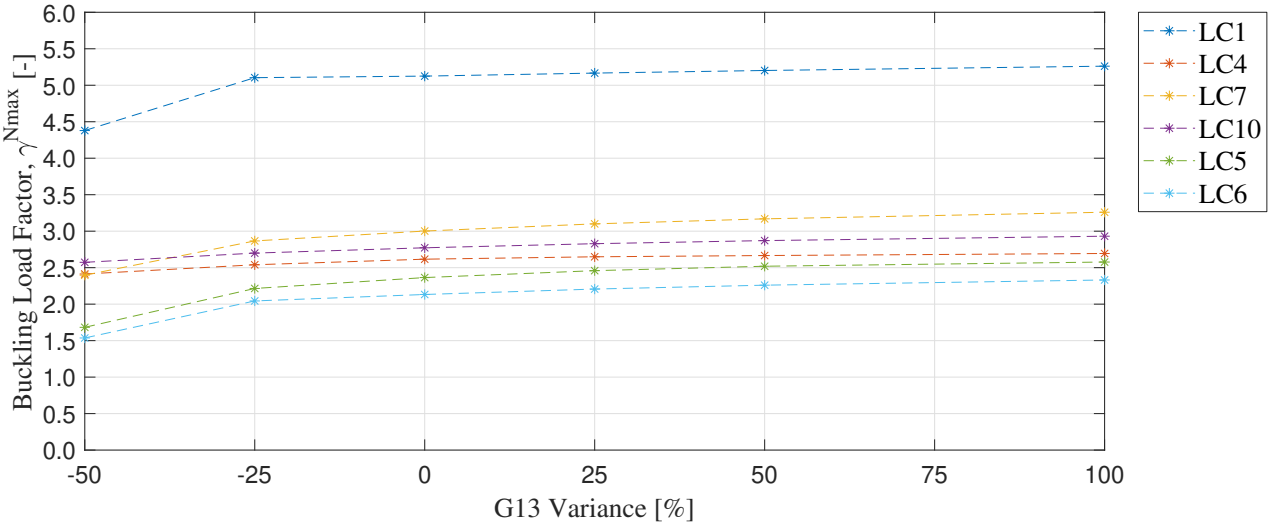

Figure 6.16: Buckling load factor $\gamma^{N_{max}}$ for varying shear modulus G_{13}. 0% variance corresponds to the baseline results.

G_{13}	LC1	LC4	LC7	LC10	LC5	LC6
−50%	-14.555	-7.761	-20.159	-7.188	-28.845	-27.950
−25%	-0.415	-2.927	-4.510	-2.626	-6.317	-4.148
+25%	0.810	1.253	3.276	2.022	4.003	3.491
+50%	1.506	1.909	5.571	3.554	6.570	5.984
+100%	2.660	2.986	8.589	5.726	9.006	9.323

Table 6.6: Percent change in $\gamma^{N_{max}}$ compared to the baseline results.

The smallest $\gamma^{N_{max}}$ is observed for $G_{13} = -50\%$ across all load cases. Notably, a significant decrease in $\gamma^{N_{max}}$ is present when $G_{13} = -25\% \rightarrow -50\%$ except for the flapwise load cases, LC 4 and LC 10. Compared with the baseline analysis, the most significant decrease is observed for LC 5 with −28.845%.

The 1st mode shapes for LC 6, the most critical load case, are provided in Figure 6.17. The effect of G_{13} is investigated by comparing $G_{13} = -50\%$ and $G_{13} = +100\%$.

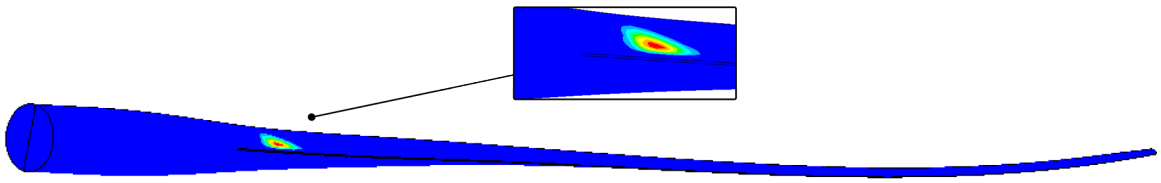

(a) 1st mode shape of Load Case 6 with $G_{13} = -50\%$.

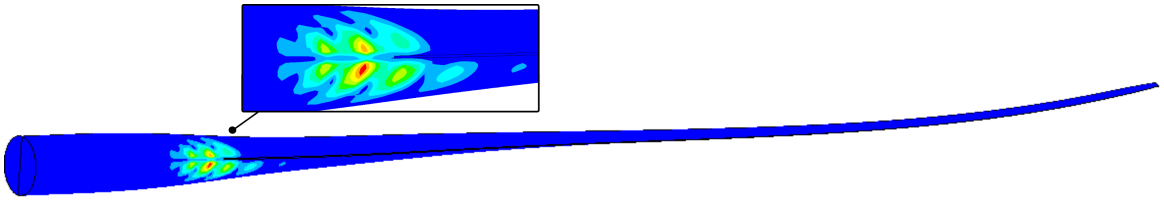

(b) 1st mode shape of Load Case 6 with $G_{13} = +100\%$.

Figure 6.17: The 1st mode shape of Load Case 6. Plotted on the deformed structure as a displacement vector sum.

The 1st mode shape for the baseline analysis and $G_{13} = +100\%$ occurs in the same region, distributed on both sides of the TE, towards the root section. In contrast, when $G_{13} = -50\%$, the 1st mode shape becomes significantly more localized on the TE suction side shell. This shift in deformation is attributed to a reduction in transverse shear stiffness in the load-bearing sandwich shells. The change in deformation mode occurs when the transverse shear stiffness is reduced from $G_{13} = -25\% \rightarrow -50\%$, which is also apparent by the sudden reduction of the $\gamma^{N_{max}}$, as seen in Figure 6.16 and Table 6.6.

The magnitude and distribution of the non-linearity factors are largely unaffected by varying the transverse shear modulus G_{13}. Generally, a softer core results in a larger magnitude and area with $\varepsilon^n_{\Delta,GNL} > 1$. Notably, a significant change in distribution is not observed, contrary to the change in the 1st mode shape for $G_{13} = -50\%$.

The maximum failure indices for the transverse shear stiffness G_{13} variations are presented in Figure 6.18.

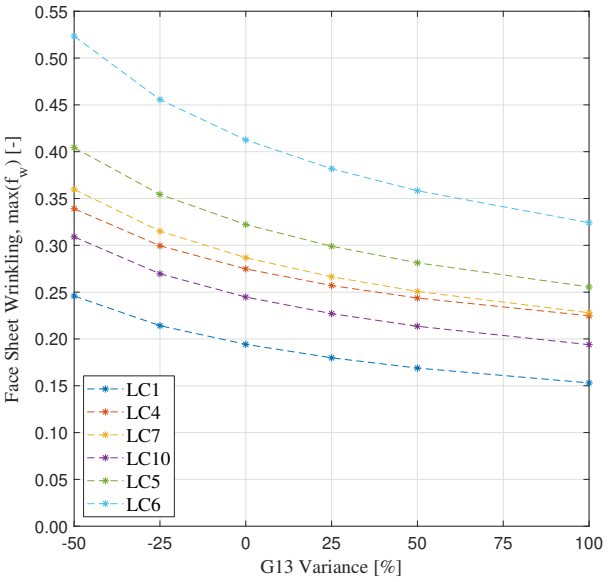

(a) Face sheet wrinkling.

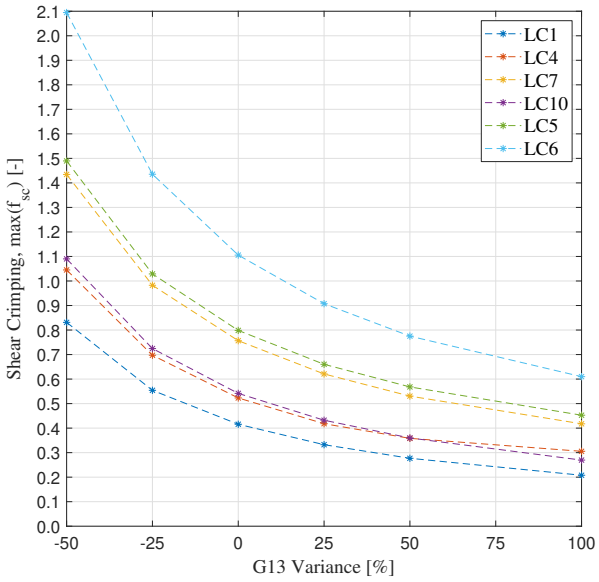

(b) Shear crimping.

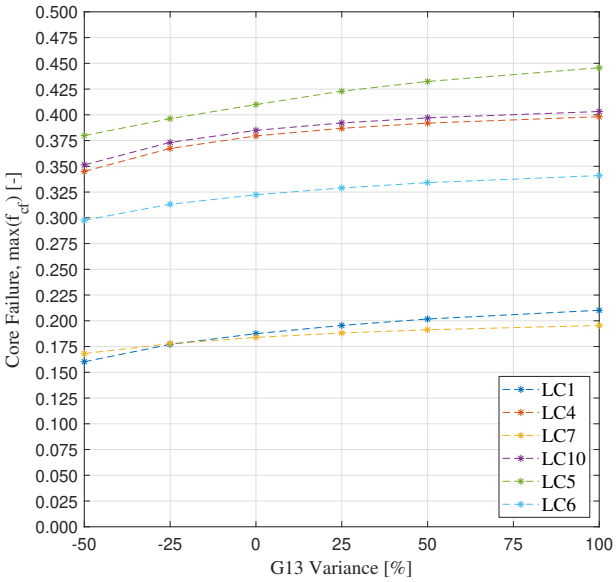

(c) Core failure.

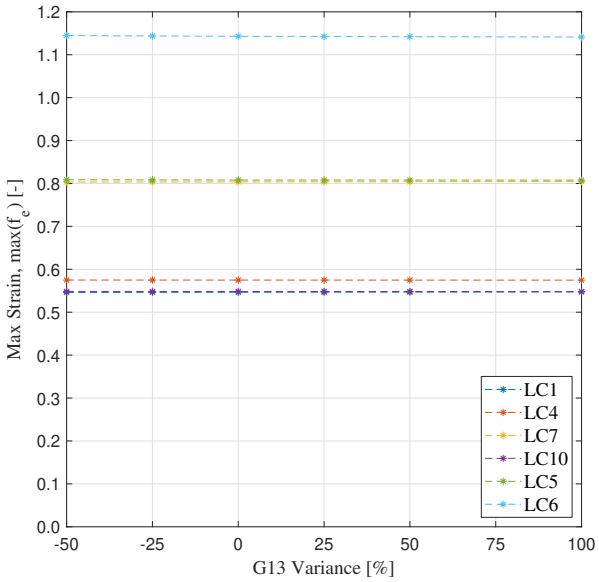

(d) Maximum strain.

Figure 6.18: Parameter plots illustrating the effect of varying transverse shear modulus G_{13} on failure criteria.

Increasing G_{13} yields a diminishing decrease in $max(f_w)$ and $max(f_{sc})$. The variation has a larger effect on shear crimping than face sheet wrinkling. The inverse proportionality is observed for core failure $max(f_{cf})$. Similarly to the core thickness variation, the $max(f_e)$ is largely unaffected by varying G_{13}.

The envelope plots of shear crimping and core failure can be seen in Figure 6.19 for $G_{13} = -50\%$ and $G_{13} = +100\%$. The envelope plots for $G_{13} = -25\%/+25\%/+50\%$ are given in Appendix G.

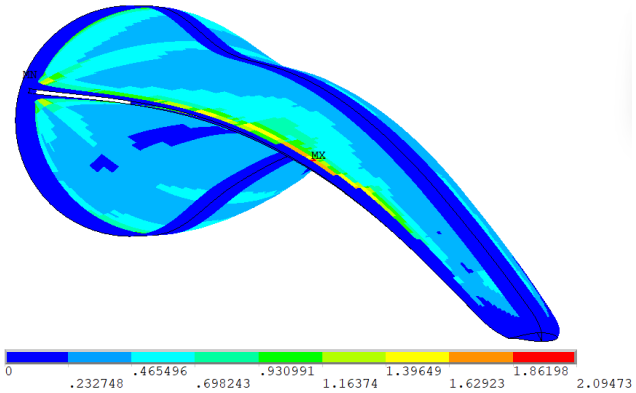

(a) Envelope plot for shear crimping for $G_{13} = -50\%$.

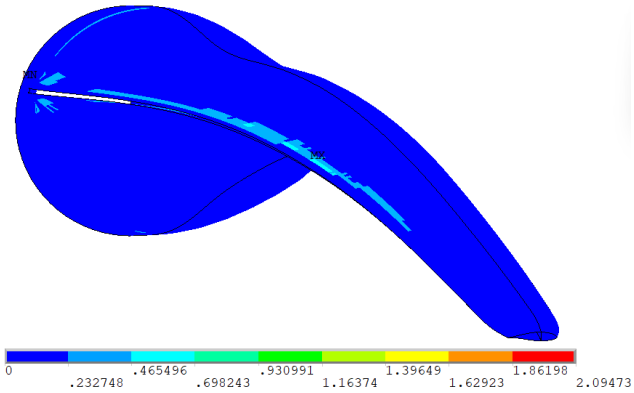

(b) Envelope plot for shear crimping for $G_{13} = +100\%$.

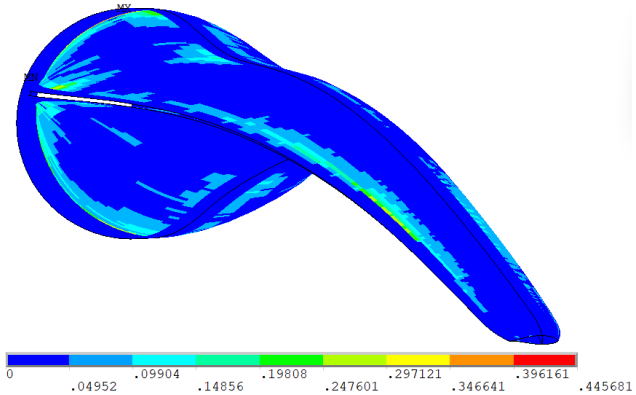

(c) Envelope plot for core failure for $G_{13} = -50\%$.

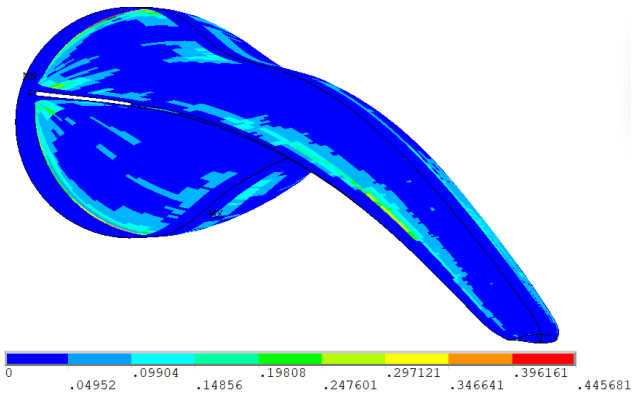

(d) Envelope plot for core failure for $G_{13} = +100\%$.

Figure 6.19: Envelope plot of shear crimping and core failure for $G_{13} = -50\%$ and $G_{13} = +100\%$. The envelope plots are shown on the underformed structure. Note that the color bar is kept constant across variations for each failure criterion. Only SHELL181 elements are plotted.

The distribution of f_w and f_e is largely unaffected by varying G_{13}. The $max(f_{sc})$ for $G_{13} = -50\%$ and $G_{13} = +100\%$ is located along the trailing edge midway between the root and the tip. When the colorbar between $G_{13} = -50\% \rightarrow +100\%$ is not kept constant, but is set based on the maximum and minimum failure indices for the respective analysis, the distributions are nearly identical across all variations. The $max(f_{cf})$ increases in the transition between the laminate and sandwich sections in the root, where the maximum values are located for all variations.

The overall effect of varying G_{13} is quantified in Figure 6.20. Comparing Figure 6.20a and Figure 6.20b, the maximum failure index is closer to the root for $G_{13} = +100\%$, and the failure indices are generally smaller. A significant shift in the active failure mode is observed. Shear crimping is active in the majority of the sandwich panels for $G_{13} = -50\%$, whereas maximum strain is active on most of the blade for $G_{13} = +100\%$. Notably, core failure is the active failure mode in the transition from laminate to sandwich panel near the root.

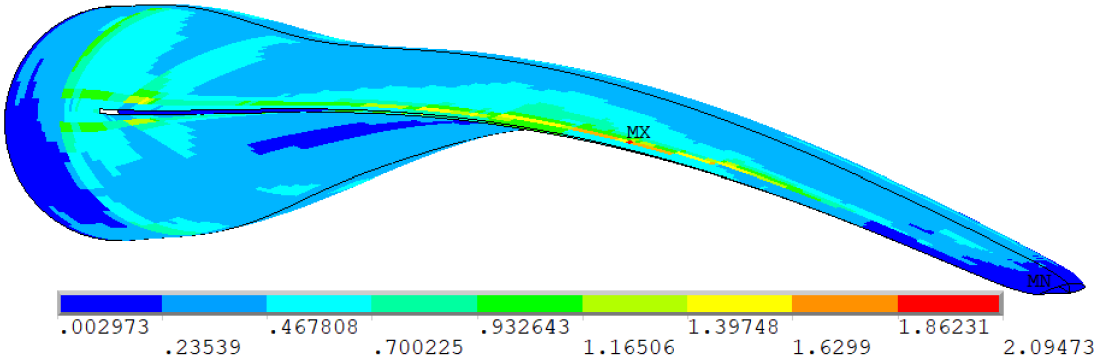

(a) Envelope plot for $G_{13} = -50\%$. This shows the maximum FI across all failure criteria and LCs.

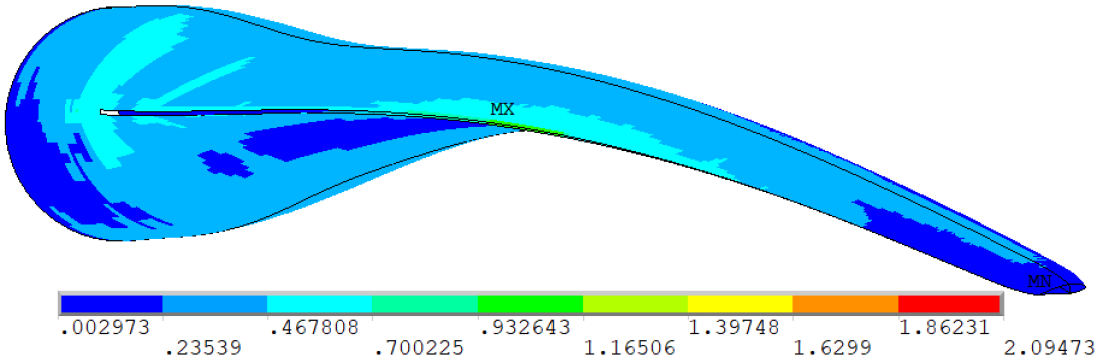

(b) Envelope plot for $G_{13} = +100\%$. This shows the maximum FI across all failure criteria and LCs.

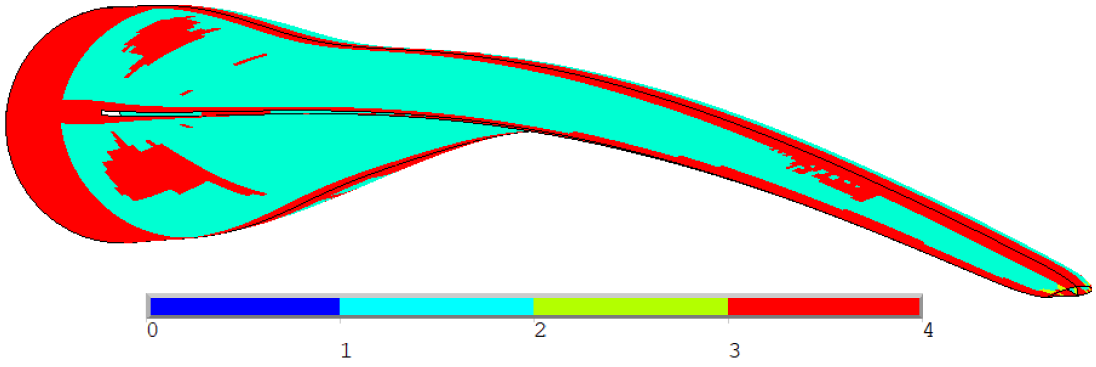

(c) Active failure mode for $G_{13} = -50\%$.

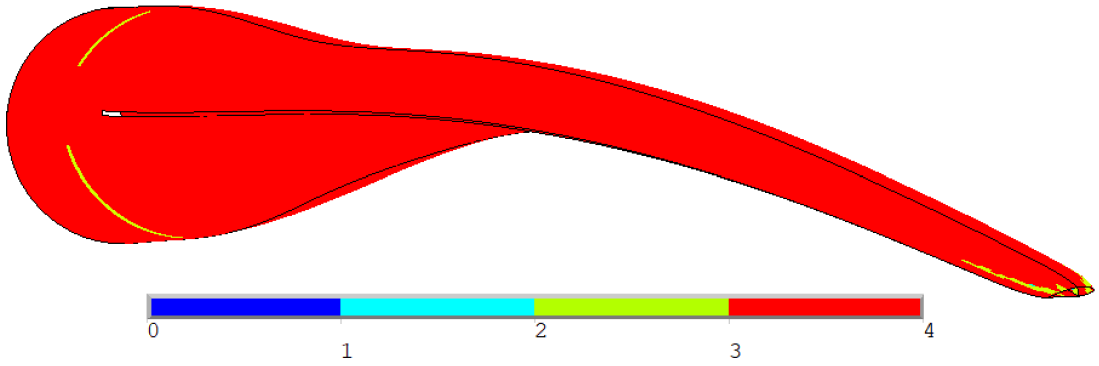

(d) Active failure mode for $G_{13} = +100\%$.

Figure 6.20: Failure mode per element related to the maximum failure index in the envelope plot. The active failure mode uses the following notation: 1 [Blue] = face sheet wrinkling, 2 [Turquoise] = shear crimping, 3 [Green] = core failure, 4 [Red] = max strain. Note that the color bar for the envelope plots is kept constant across variations.

6.5.2 Transverse Shear Modulus G_{23}

The buckling load factor at the last load step $\gamma^{N_{max}}$ for all variations of shear modulus G_{23} is presented in Figure 6.21 and the associated percentage change from the baseline analysis is presented in Table 6.7.

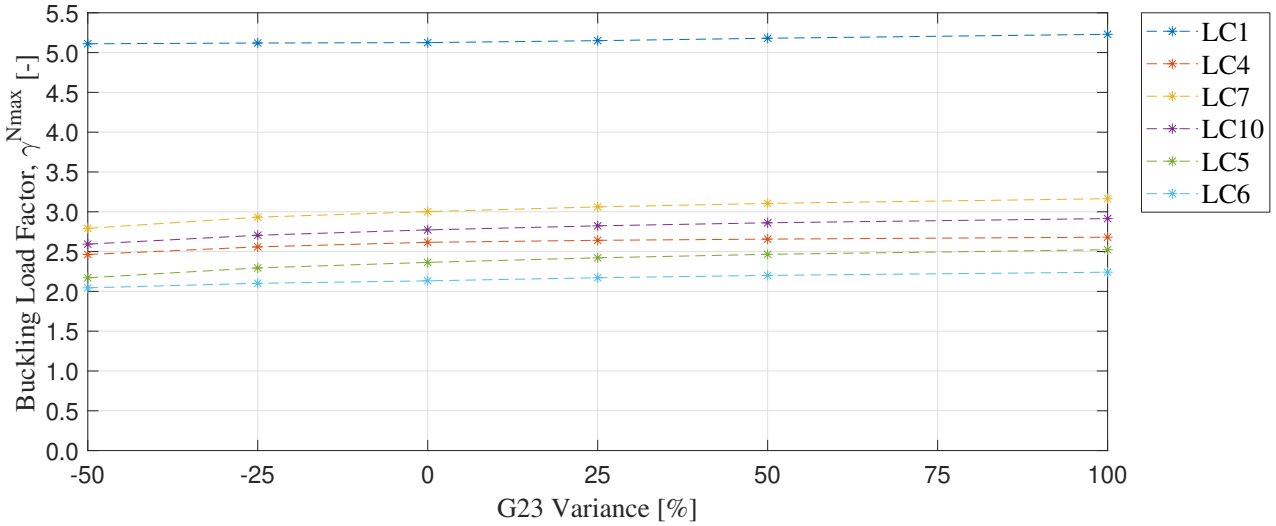

Figure 6.21: Buckling load factor at last load step $\gamma^{N_{max}}$ for varying shear modulus G_{23}. 0% variance corresponds to the baseline results.

G_{23}	LC1	LC4	LC7	LC10	LC5	LC6
−50%	-0.289	-5.853	-7.007	-6.457	-8.172	-4.134
−25%	-0.100	-2.187	-2.326	-2.433	-2.947	-1.444
+25%	0.477	0.966	1.987	1.837	2.432	1.818
+50%	1.070	1.539	3.449	3.211	4.272	3.201
+100%	2.039	2.467	5.410	5.132	6.736	5.091

Table 6.7: Percent change in $\gamma^{N_{max}}$ for 1st mode shape compared to the baseline results.

The same tendency as the previous parameters is observed. The smallest $\gamma^{N_{max}}$ is observed for $G_{23} = -50\%$ across all load cases. LC 5 is the most sensitive to varying G_{23} with a decrease of -8.172% for $G_{13} = -50\%$ and an increase of 6.736% for $G_{13} = +100\%$. LC 6 is the most critical with the smallest $\gamma^{N_{max}}$. The 1st mode shape of LC 6 is presented in Figure 6.22 for the outer ranges of the variation.

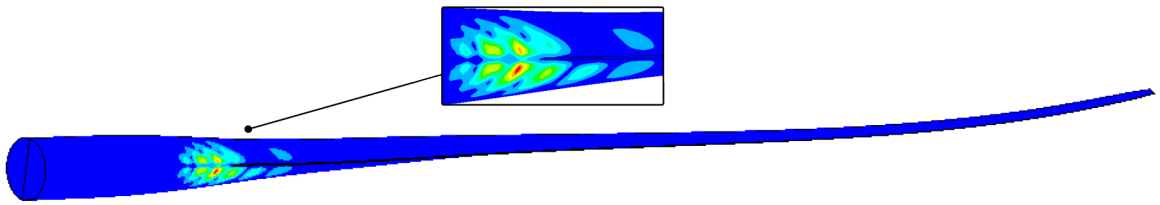

(a) 1st mode shape of Load Case 6 with $G_{23} = -50\%$.

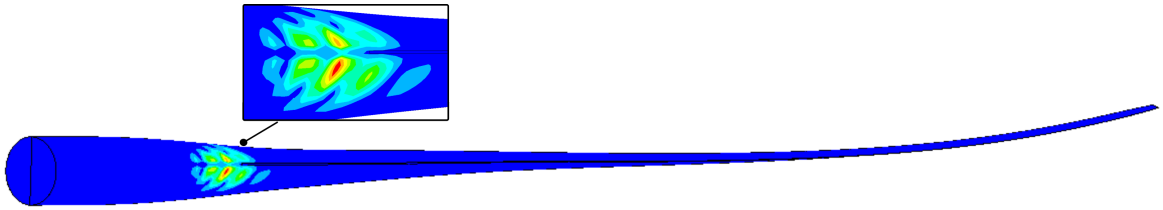

(b) 1st mode shape of Load Case 6 with $G_{23} = +100\%$.

Figure 6.22: The 1st mode shape of Load Case 6. Plotted on the deformed structure as a displacement vector sum.

A low sensitivity to changes in transverse shear stiffness G_{23} is also evident in the 1st mode shapes, which remain nearly unchanged across the baseline, $G_{23} = -50\%$, and $G_{23} = +100\%$ configurations. However, a slight tendency of increased localization in the deformation mode is observed as G_{23} increases.

Similarly to varying G_{13}, the magnitude and distribution of the non-linearity factors are largely unaffected by varying G_{23}. Generally, a softer core results in a larger magnitude and area with $\varepsilon^n_{\Delta,GNL} > 1$.

The parameter plots for face sheet wrinkling $max(f_w)$, shear crimping $max(f_{sc})$, core failure $max(f_{cf})$, and maximum strain $max(f_e)$ for all variations of G_{23} are presented in Figure 6.23. Varying G_{23} has a low influence on the maximum failure indices for face sheet wrinkling, core failure, and maximum strain. An exception is observed for $max(f_w)$ in LC 4, where an increase in transverse shear stiffness G_{23} corresponds to a decrease in max failure index. For shear crimping, G_{23} has a large influence on the edgewise LC 7 and the mixed LCs 5 and 6, where the failure index decreases from $G_{23} = -50\% \rightarrow +100\%$. The flapwise LC 4 experiences a significant reduction in maximum failure index from $G_{23} = -50\% \rightarrow -25\%$, however, it is mostly constant when increased beyond -25%. The edgewise LC 1 and flapwise LC 10 are largely unchanged for all variations of G_{23}.

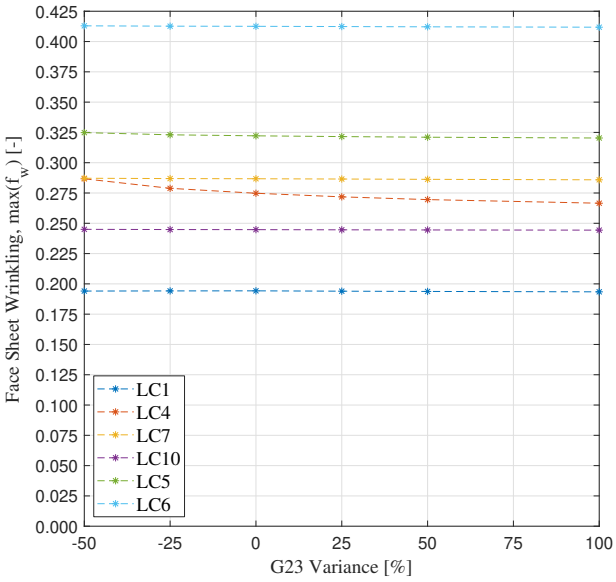

(a) Face sheet wrinkling.

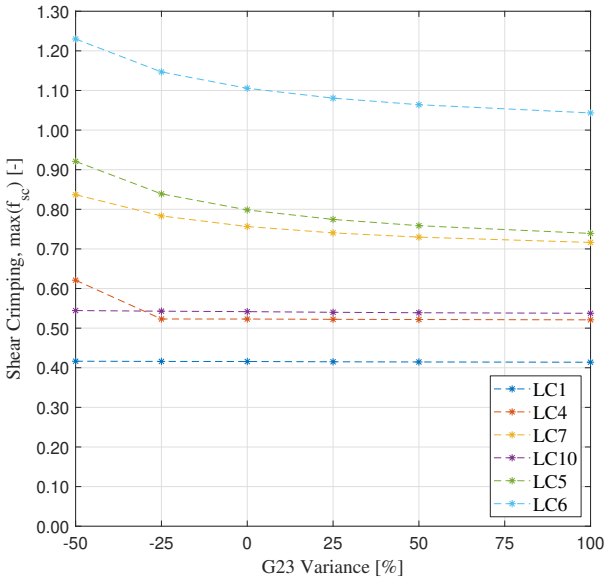

(b) Shear crimping.

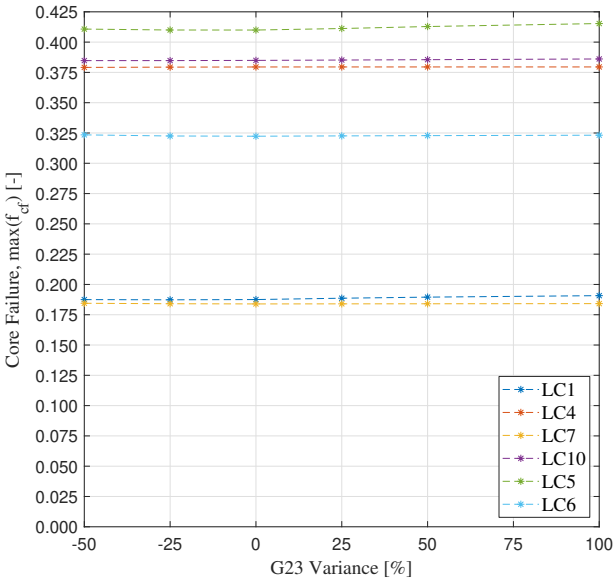

(c) Core Failure.

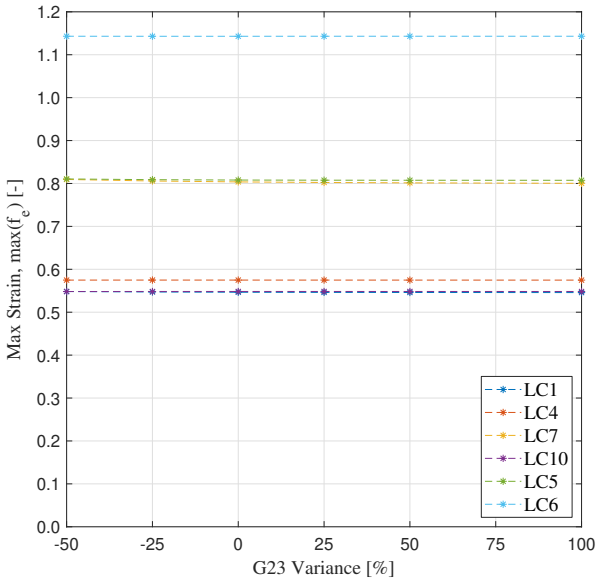

(d) Maximum strain.

Figure 6.23: Parameter plots illustrating the effect of varying transverse shear modulus G_{23} on failure criteria.

The envelope plots for shear crimping and core failure when $G_{23} = -50\%$ and $G_{23} = +100\%$ are presented in Figure 6.24.

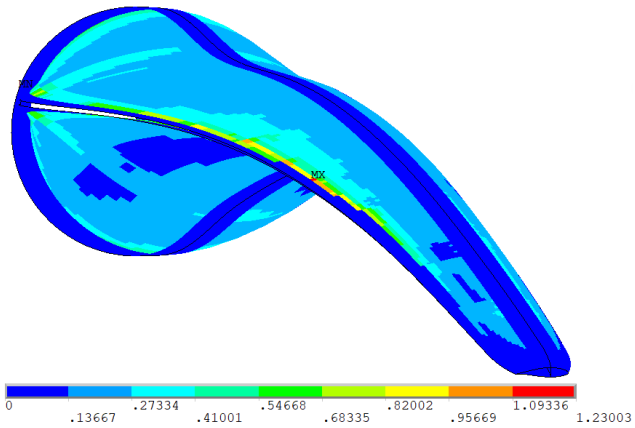

(a) Envelope plot for shear crimping for $G_{23} = -50\%$.

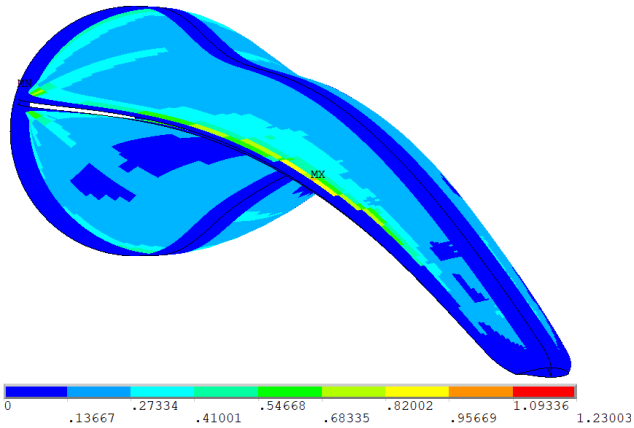

(b) Envelope plot for shear crimping for $G_{23} = +100\%$.

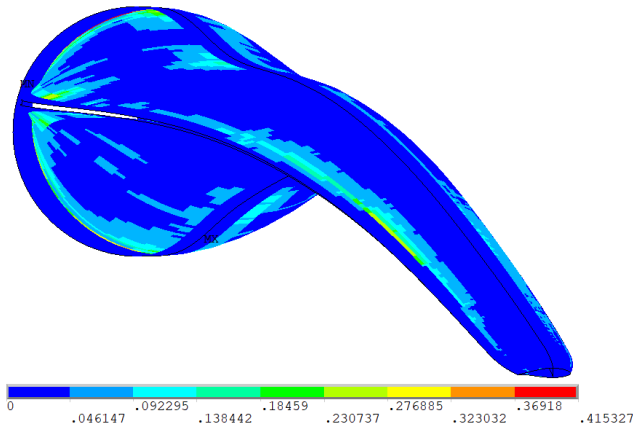

(c) Envelope plot for core failure for $G_{23} = -50\%$.

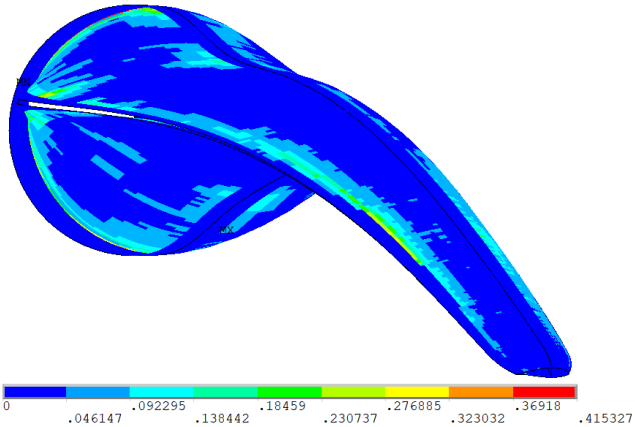

(d) Envelope plot for core failure for $G_{23} = +100\%$.

Figure 6.24: Envelope plot of shear crimping and core failure for $G_{23} = -50\%$ and $G_{23} = +100\%$. The envelope plots are shown on the underformed structure. Note that the color bar is kept constant across variations for each failure criterion. Only SHELL181 elements are plotted.

The insensitivity of the failure criteria to variations in G_{23} is evident in the envelope plots for shear crimping and core failure. The overall distribution remains almost identical when the transverse shear stiffness varies between $G_{23} = -50\%$ and $G_{23} = +100$.

Little overall effect on magnitude and distribution is observed by varying G_{23} as evident in the envelope plots in Figure 6.25. The maximum failure index moves closer to the root. The active failure criterion is mostly maximum strain with shear crimping at the transition from laminate to sandwich panels in the root and along the trailing edge.

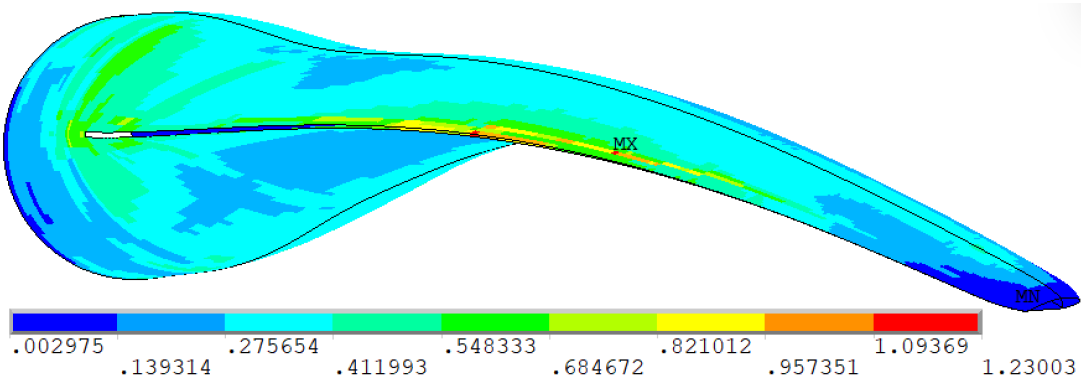

(a) Envelope plot for $G_{23} = -50\%$.

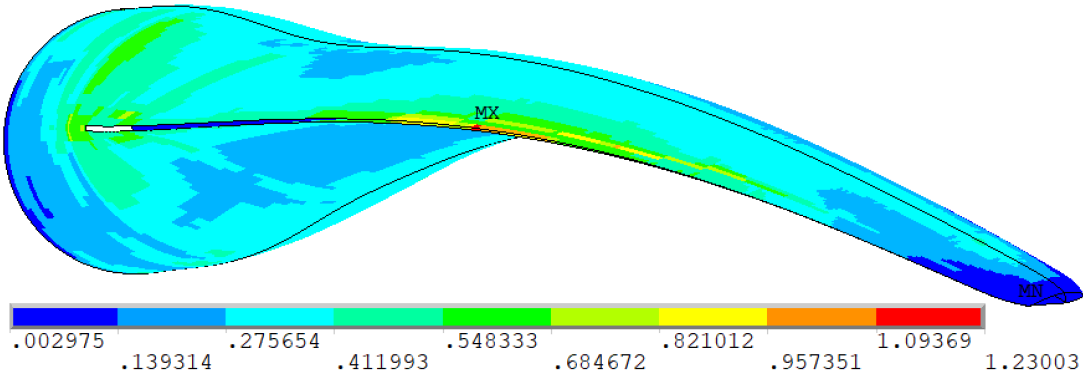

(b) Envelope plot for $G_{23} = +100\%$.

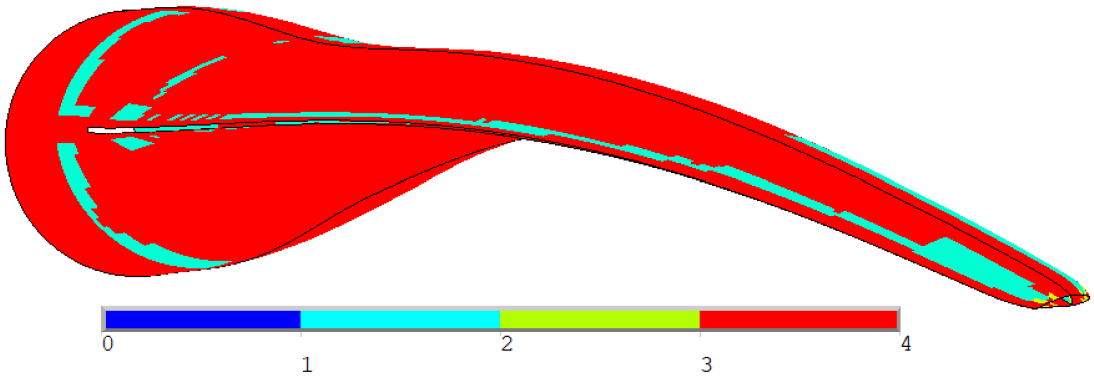

(c) Active failure mode for $G_{23} = -50\%$.

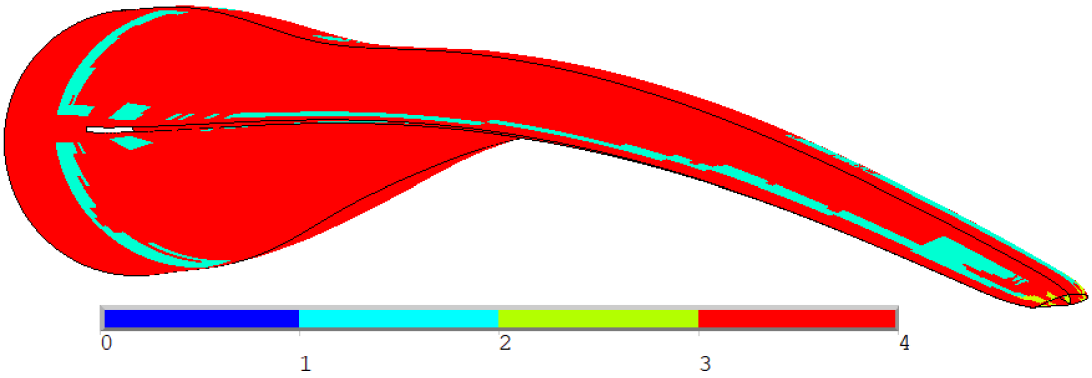

(d) Active failure mode for $G_{23} = +100\%$.

Figure 6.25: Envelope plot and corresponding failure mode for the $G_{23} = -50\%$ and $G_{23} = +100\%$ configurations. The envelope plot depicts the failure mode related to the maximum failure index in the envelope plot: 1 [Blue] = face sheet wrinkling, 2 [Turquoise] = shear crimping, 3 [Green] = core failure, 4 [Red] = max strain. Note that the color bar for the envelope plots is kept constant across variations.

6.6 Comparison of Parameters

The effect of each parameter is compared by considering each load case separately in heat maps. The normalized analysis metrics, i.e., the maximum failure indices across all elements and the buckling load factor $\gamma^{N_{max}}$, are plotted against the variations of each parameter. This provides a visual overview for comparing across parameters. The same color bar is used to compare across heat maps. The analysis metrics are normalized with the baseline analysis using equation 6.1.

$$f_{norm} = \frac{f_{metric} - f_{base}}{f_{base}} \cdot 100 \tag{6.1}$$

Here, f_{norm} is the normalized analysis metric, f_{base} is the baseline result. The edgewise (LCs 1 and 7), flapwise (LCs 4 and 10), and mixed load cases (LCs 5 and 6) are presented in Tables 6.8 and 6.9.

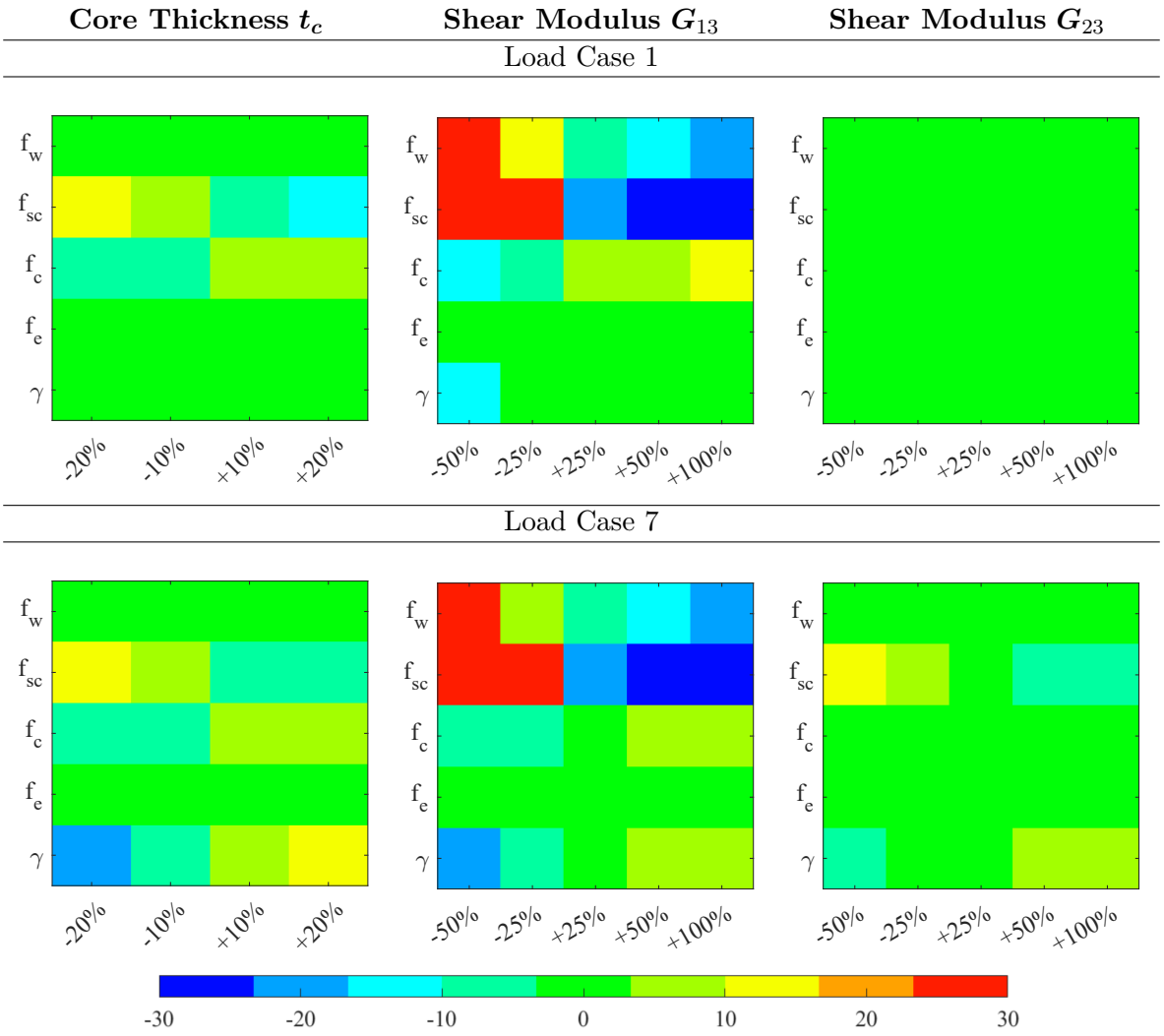

Table 6.8: Heat maps of normalized analysis metrics for edgewise load cases. The color represents percentage change according to equation (6.1).

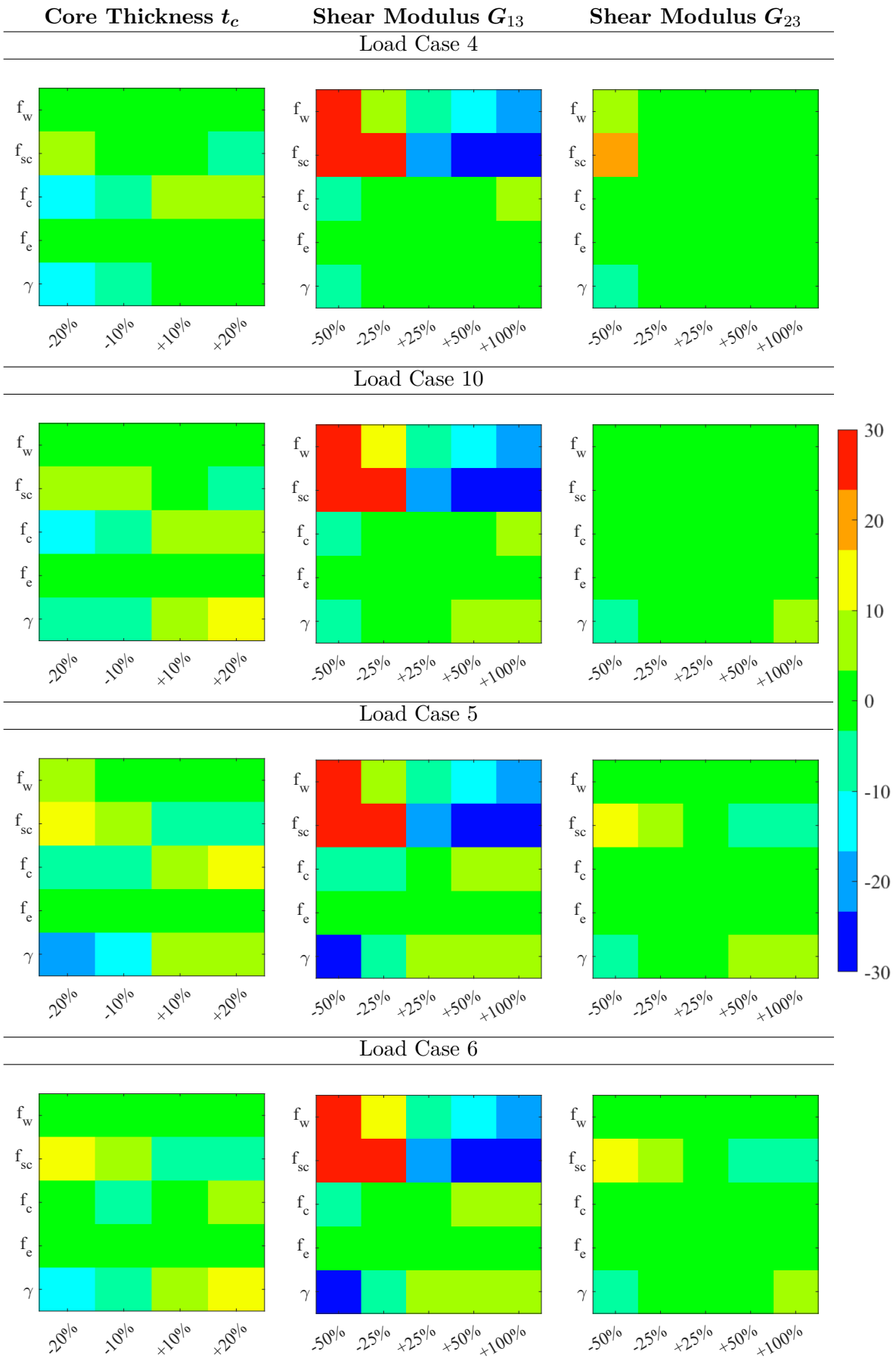

Table 6.9: Heat maps of normalized analysis metrics for the flapwise and mixed load cases. The color represents percentage change according to equation (6.1).

6.7 Discussion of the Parametric Study

This chapter presented a univariate parametric study on the Gurit98m WTB model. The effect of varying structural parameters related to the core material on the composite failure and buckling behavior was investigated. Six load cases were applied to asses the response of the blade under different loading conditions. The chosen parameters were core thickness t_C and the core transverse shear moduli G_{13} and G_{23}. The effect of varying the parameters was compared with a baseline analysis. The buckling behavior was quantified in the $\gamma^{N_{max}}$ and the mode shape of the most critical load case. Failure was assessed using face sheet wrinkling, shear crimping, core failure, and maximum strain failure criteria.

The non-linear buckling analysis of the baseline configuration showed an increased γ^n with increased loading across all load cases. The Gurit98m model was originally designed considering linear buckling. Following the DNV guidelines, the buckling load factor must be larger than 1.96 for a linear buckling analysis, while a non-linear analysis only requires $\gamma^{N_{max}} > 1.65$, as described in Section 2.4. The reduction in required safety factor and the increased $\gamma^{N_{max}}$ indicate a potential for significant weight reduction if non-linear buckling were used in the design process. Load Case 6 consistently emerged as the most critical with respect to buckling failure, exhibiting a mode shape localized along the trailing edge across all parameter variations. All LCs loaded toward the trailing edge have a significantly lower $\gamma^{N_{max}}$ compared to LC 1, which is loaded towards the LE. This suggests that the leading edge is generally less susceptible to buckling. Placing the LE and TE under compression can be simplified to shells under axial compression, where the LE has a larger curvature than the TE shells. This aligns with the findings in [Kettner, 2020, Ch. 2], where a positive correlation is observed between the curvature and γ^n. The envelope plots show that the highest failure indices are concentrated along the trailing edge, particularly in the mid-span region where the structural layup transitions from laminate to sandwich. See Figures 6.15, 6.20, 6.25. Additionally, elevated failure indices are observed near the root region of the trailing edge, in the area where the solid elements that provide added stiffness to the trailing edge come to an end. The increased failure indices in this region may be explained by a stress concentration arising due to the difference in stiffness when the blade is subjected to loading toward the trailing edge.

Effect of Core Thickness t_C
A general trend of proportionality between $\gamma^{N_{max}}$ and t_C was observed. LC 1 yielded the largest $\gamma^{N_{max}}$ for all variations, with a low sensitivity. A $\pm 20\%$ change in t_C altered $\gamma^{N_{max}}$ by only -1.98% to $+0.07\%$. The variation $t_C = +20\%$ yielded a mode shape corresponding to the 3$^{\text{rd}}$ mode shape in the baseline analysis for LC 6. This may be attributed to an enhanced ability of the TE shells near the root to resist buckling. A low sensitivity to t_C is observed for face sheet wrinkling. This aligns with equation (2.27), as the geometry of the core material is not included in calculating the wrinkling stress σ_w. An inverse proportionality is observed between t_C and the $max\,(f_{sc})$ for all load cases, owing to the linear dependence of the allowable shear-crimp force resultant N_{sc} on t_C, see equation (2.24). The $max\,(f_{cf})$ increased locally with increasing t_C in the transition between the laminate and sandwich layup at the root. A possible explanation is a stress concentration forming due to an increased stress gradient. However, as the core becomes thinner, the transverse shear stress increases, and the failure index increases from $t_C = -10\% \rightarrow -20\%$. The thickness of the core material generally has a low influence on the $max(f_e)$, because the face sheets carry most of the in-plane loading, regardless of the thickness of the core.

Effect of Shear Modulus G_{13}
The buckling load factor $\gamma^{N_{max}}$ exhibits low sensitivity to variations in G_{13} over the interval $G_{13} = -25\% \rightarrow +100\%$. The variation $G_{13} = -50\%$ revealed a significant decrease in $\gamma^{N_{max}}$ for all load cases except for the flapwise load cases, LC 4 and LC 10. This is likely because flapwise bending is primarily carried by the spar caps, unaffected by changes in core shear stiffness. The considerable decrease in

$\gamma^{N_{max}}$ is accompanied by a pronounced localization of the 1st mode shape in LC 6. Increasing G_{13} yielded lower $max\,(f_w)$ and $max\,(f_{sc})$. A greater influence of G_{13} on $max(f_{sc})$ compared to $max(f_w)$ is observed, which is consistent with equations (2.24) and (2.27), where the transverse shear modulus appears to the first power in the shear crimping expression and to the one-third power in the face sheet wrinkling expression. The transition from a laminate to sandwich layup in the root experiences a significant increase in f_{cf} with increasing G_{13}. This is also evident in Figure 6.20d. The variation of G_{13} minimally influenced $max(f_e)$. The significant sensitivity G_{13} has on shear crimping is evident for the active failure modes in Figure 6.20c and 6.20d, where the active failure mode goes from shear crimping dominated to primarily maximum strain with increasing G_{13}.

Effect of Shear Modulus G_{23}
G_{23} represents the transverse shear stiffness in the hoop direction. A low influence is observed for the $\gamma^{N_{max}}$ and mode shapes for all variations of G_{23}. This is also the case for the failure indices, which are nearly unaffected by the reduction of G_{23}. An exception is observed for LCs inducing compression in the trailing edge, i.e., 5, 6, and 7 for shear crimping.

Relative Parameter Importance and Recommendations
The heat maps in Table 6.8 and Table 6.9 confirm that G_{13} is the dominant core parameter, followed by thickness t_C. G_{23} has limited influence for the load cases considered. Designers seeking to replace balsa with PET foam as core material in WTBs should prioritize enhancing the transverse shear modulus in the wind turbine blade's spanwise direction before increasing the core thickness. Enhancing the transverse shear stiffness G_{13} by using higher-density foams or increasing the core thickness would, however, increase the weight of the blade. The most favorable stiffness-to-weight trade-off is achieved by selectively enhancing G_{13} while allowing a modest reduction in G_{23}.

Parametric Study - Limitations
As discussed in Section 2.2.3, the assumptions of the eigenvalue buckling analysis based on linear perturbation become more accurate as the analysis approaches the stability point, thereby improving the accuracy of the approximated buckling load. This, however, requires a large number of load steps to ensure numerical stability of the non-linear buckling analysis presented in Chapter 3. The computational costs associated with increasing the number of load steps made loading the blade to the stability point infeasible. Consequently, the structure was subjected to the full loading defined by each load case to assess its response under the prescribed extreme conditions. However, this approach may not yield accurate results, as loading the structure beyond FPF can misrepresent its actual performance [Jones, 1999, p. 251]. The parametric study included only six of the twelve available load cases. Only LC 1 loads the structure towards the leading edge for the considered load cases. To adequately assess the performance of the leading edge, it is necessary to incorporate all twelve load cases.

Shear crimping and max strain yielded the most dominant failure modes for all variations. While the maximum strain failure criteria is sufficient in assessing fiber failure, other criteria should be applied for determining inter-fiber failure, such as the quadratic or physical failure criteria, presented in Section 2.3.2, [DNV-GL, 2015] [Puck and Schürmann, 2002]. DNV recommends either Puck's action plane or LaRC03 failure criteria [DNV-GL, 2015, p. 33]. Additionally, according to ACP, the shear crimping factors k_C and k_F should be determined experimentally to accuracy asses shear crimping failure for the specific material and application [ANSYS, 2024a, p. 416].
Accurate failure assessment in the trailing edge, leading edge, and connection from the shear web to the outer shells requires detailed models, which the Gurit98m does not include [Hermansen et al., 2025, p. 5]. Moreover, although the core thickness variations do not result in significant changes in geometry, the feasibility of details such as ply drops and transitions from laminate to sandwich layup is not accounted for in the varied configurations. This may limit the accuracy of localized failure predictions in the transitional regions.

7 | Discussion

Discussion of the verification and parametric study results is provided in Section 5.5 and 6.7, respectively. This chapter considers the implications of the non-linear buckling analysis with integrated laminate failure criteria and the implemented post-processing of sandwich failure criteria in a broader context. Additionally, potential improvements and directions for future work are addressed.

Broader Context
Post-processing of sandwich and laminate failure criteria accompanying a non-linear buckling analysis in ANSYS represents a step toward enabling the transition from balsa wood to recyclable polyethylene terephthalate (PET) foam for sandwich structures in wind turbine blades. The developed numerical framework is well-suited for the detailed design phase, offering an accurate assessment of buckling and first ply failure in large composite structures. Compared to progressive damage models, its relatively low computational demand enhances its accessibility for industrial applications, where extensive simulation capabilities may be constrained. Moreover, the developed analysis tool holds potential for core material manufacturers, like Gurit, in designing materials tailored explicitly to wind turbine blades.

The parametric study demonstrated that core thickness and spanwise transverse shear stiffness significantly influence structural performance with respect to buckling and sandwich failure. Different variations of the structural parameters demonstrated a shift in the dominant failure mode from laminate to sandwich failure. This highlights the importance of incorporating sandwich failure criteria in WTB design, as the influence of these parameters was minimal when considering laminate failure alone. Although this study focused exclusively on transverse shear stiffness and core thickness, the developed framework may also be extended to investigate additional parameters and regions of interest, further supporting material, and blade design advancements.

Improvement and Future Work
Despite the strengths of the developed analysis tool, areas of improvement have been identified. This section addresses potential enhancements to the APDL-based non-linear buckling analysis and the Fortran Post-Processing (FPP) implementation.

The non-linearity factors were introduced to identify the onset and location of local buckling within the structure by measuring non-linear bending across all elements. By highlighting regions where local buckling initiates, these factors provide insight into areas that have experienced a loss of stiffness, leading to stress redistribution. This can lead to elevated stresses in other parts of the structure, potentially resulting in composite failure. While FPF may indicate which regions where loading exceeds material limits, the non-linearity factors can help identify regions that should be prioritized when reinforcing the structure.

Initially, the non-linearity factors were intended to serve as stopping criteria for the Newton–Raphson based analysis, described in Chapter 3. To this end, the factors are computed at each load step and compared to a user-defined critical non-linearity factor. However, as demonstrated by [Tønnesen and

Christoffersen, 2025], the values of the non-linearity factors are highly sensitive to the truncation number, which introduces unreliability. Consequently, the truncation number must be selected carefully based on preliminary analyses for the specific application [Tønnesen and Christoffersen, 2025]. A more robust application could involve post-processing the non-linearity factors across substeps, thereby reducing the method's sensitivity to the truncation number and number of load steps at the beginning of the analysis.

The Newtown-Raphson based analysis employs constant load increments, defined by $\alpha^n = \frac{n}{N_{max}}$. This approach requires many load steps to sufficiently approximate the buckling load factor γ^n near the stability point. Implementing adaptive load stepping would significantly reduce the computational cost of the developed analysis tool by applying progressively smaller step sizes as the analysis reaches closer to the stability point. The load factor for load stepping α^{n+1} could be dynamically adjusted based on the approximated buckling from the previous load step λ_1^n.

Discrepancies in face sheet wrinkling predictions between FPP and ACP were observed, likely originating from differences in stress evaluation methodologies. In the FPP routine, face sheet stresses are computed by averaging nodal values from the top, bottom, and mid-plane of all laminae, using the `ETABLE` command, which returns element-averaged nodal data [ANSYS, 2024b, p. 688–689], [ANSYS, 2024c, p. 52]. Alternative approaches to stress evaluation may be explored to improve fidelity, such as averaging integration point values or using the maximum integration point value. Ultimately, the choice of method should be guided by comparison with experimental data.

The current analysis method does not include transverse normal stress σ_3 as part of calculating the core failure criterion described in 2.3.3. Although σ_3 is not part of FSDT used to formulate the four-node linear shell element SHELL181, interlaminar normal stresses can be post-processed [ANSYS, 2024a, p. 387- 388]. Retrieving interlaminar stresses can also facilitate the implementation of adhesive failure criteria, see [ANSYS, 2024a, p. 417]. Moreover, fatigue is not included in the current analysis method. Due to the dynamic nature of the operational loads acting on WTBs, this is an important failure mode to consider. This is evident in the design guidelines [DNV-GL, 2015, p. 35].

8 | Conclusion

The overall aim of the thesis is encapsulated in the problem statement, reprinted for convenience:

How can composite failure criteria be implemented to accompany a non-linear buckling analysis in identifying the key structural parameters relevant to replace balsa wood with PET foam as the core material in Gurit98m?

The implementation of composite failure criteria accompanying a non-linear buckling analysis is motivated by the accurate assessment of failure when replacing balsa wood with PET foam. Identifying key structural parameters is motivated by facilitating advancements in PET foam as a core material. This requires identifying the material parameters that most effectively enhance the failure resistance of wind turbine blades.

To facilitate the accurate assessment of failure in WTBs, the structural layout of wind turbine blades, buckling, and composite failure was researched. This research identified face sheet wrinkling, shear crimping, and core failure as the most relevant sandwich failure criteria. The analysis method developed in [Tønnesen and Christoffersen, 2025] was expanded to accommodate multiple load cases and export element stresses, force resultants, and laminate failure indices. The selected sandwich failure criteria were implemented in Fortran as a post-processing routine. The routine identifies sandwich elements and conducts constitutive modeling of the top and bottom face sheets and the core, based on FSDT. Care was taken to ensure numerical accuracy, including consideration of round-off errors associated with double-precision arithmetic.

The implementation was verified against multiple reference solutions: an analytical FSDT-based MATLAB model with sandwich failure criteria, AAU's in-house software MUST, and the commercial FEA tool ACP. A series of five verification examples, comprising three layup configurations and four loading scenarios, confirmed the implementation's accuracy. Identical results were achieved for the two simplest cases across all analysis tools. Strong agreement with MUST was observed in all cases. Minor discrepancies with ACP were observed. The source of the discrepancy was investigated. The discrepancy in face sheet wrinkling was thought to stem from the determination of the stress acting on the face sheets, while shear crimping deviated due to the round of errors associated with small numbers.

A univariate parametric study was conducted to identify key structural parameters for effectively replacing balsa wood with PET foam in the Gurit98m WTB model. Six representative load cases were analyzed while systematically varying the core thickness and transverse shear moduli G_{13} and G_{23}. The results showed that G_{13} had the most pronounced impact on the buckling load factors and failure indices, followed by core thickness. Conversely, G_{23} exhibited negligible influence. Additionally, the structural parameters had an inconsequential effect on the laminate failure criteria.

In conclusion, this thesis has demonstrated that implementing composite sandwich failure criteria with a non-linear buckling analysis provides a framework for assessing structural performance relevant for replacing balsa wood with PET foam in wind turbine blades. The implementation enables evaluation

of buckling and sandwich failure behavior in large composite structures. The univariate parametric study identified the transverse shear modulus in the spanwise direction (G_{13}) as the most influential structural parameter, followed by core thickness. These findings provide recommendations for future material design and underscore the importance of incorporating sandwich failure criteria in wind turbine blade design.

Bibliography

ANSYS. Comparing strain/stress and failure plots in ansys acp — lesson 4, a. URL bit.ly/43HaaN3. Last accessed: 03-05-2025.

ANSYS. Acp user's guide, 07 2024a. URL https://ansyshelp.ansys.com/public/account/secured?returnurl=/Views/Secured/corp/v242/en/acp_ug/acp_ug.html. Last accessed: 11-03-2025.

ANSYS. Command reference, 07 2024b. URL https://ansyshelp.ansys.com/account/secured?returnurl=/Views/Secured/prod_page.html?pn=Mechanical%20APDL&prodver=24.2&lang=en. Last accessed: 15-10-2024.

ANSYS. Element reference, 07 2024c. URL https://ansyshelp.ansys.com/account/secured?returnurl=/Views/Secured/prod_page.html?pn=Mechanical%20APDL&prodver=24.2&lang=en. Last accessed: 15-10-2024.

ANSYS. Structural analysis guide, 07 2024d. URL https://ansyshelp.ansys.com/public/account/secured?returnurl=/Views/Secured/corp/v251/en/ans_str/Hlp_G_StrTOC.html. Last accessed: 15-04-2025.

ANSYS. Theory reference, 07 2024e. URL https://ansyshelp.ansys.com/account/secured?returnurl=/Views/Secured/prod_page.html?pn=Mechanical%20APDL&prodver=24.2&lang=en. Last accessed: 15-10-2024.

ANSYS. Composites theory reference, 01 2025. URL https://ansyshelp.ansys.com/account/secured?returnurl=/Views/Secured/corp/v251/en/acp_comp_thry/acp_comp_thry.html. Last accessed: 11-03-2025.

ANSYS, 2025b. URL https://www.ansys.com/. Last accessed: 25-05-2025.

Arkema. Breakthrough in wind turbine blade recycling: Zebra project demonstrates closed-loop system, 2024. URL https://www.arkema.com/global/en/media/newslist/news/global/innovation/2024/20241003-zebra-wind-turbine-blade-recycling/. Last accessed: 18-02-2025.

K.J. Bathe. *Finite element procedures.* Prentice Hall, Englewood Cliffs, 1996. ISBN 0-13-301458-4.

Z. P. Bazant and L. Cedolin. *Stability of structures : elastic, inelastic, fracture, and damage theories.* Oxford University Press, New York, N.Y, 1991. ISBN 0195055292.

BECAS. Beam cross section analysis software. URL https://becas.dtu.dk/. Last accessed: 25-02-2025.

J. P. Blasques and M. Stolpe. Multi-material topology optimization of laminated composite beam cross sections. *Composite Structures*, 94(11):3278–3289, 2012. ISSN 0263-8223. doi: https://doi.org/10.

1016/j.compstruct.2012.05.002. URL https://www.sciencedirect.com/science/article/pii/S0263822312002085.

B. H. Coburn and P. M. Weaver. Buckling analysis, design and optimisation of variable-stiffness sandwich panels. *International Journal of Solids and Structures*, 96:217–228, 2016. ISSN 0020-7683. doi: https://doi.org/10.1016/j.ijsolstr.2016.06.007. URL https://www.sciencedirect.com/science/article/pii/S002076831630124X.

R. D. Cook, D. S. Malkus, M. E. Plesha, and R. J. Witt. *Concepts and Applications of Finite Element Analysis*. John Wiley & Sons, Inc., 4th edition, 2002.

F. B. I Dalmases. A green paradox: Deforesting the amazon for wind energy in the global north, 2021. URL https://bit.ly/3H9k950. Last accessed: 18-02-2025.

DecomBlades. URL https://decomblades.dk/?lang=da. Last accessed: 18-02-2025.

DNV-GL. Dnvgl-st-0376: Rotor blades for wind turbines. Technical report, DNV GL Group AS, 2015.

DNV-GL. Dnvgl-st-0437: Loads and site conditions for wind turbines. Technical report, DNV GL Group AS, 2016.

ESA. Structural materials handbook, 1994. ISSN 0379 - 0459. URL https://apc.u-paris.fr/APC_CS/Labo/Espace_Qualite/tch/normes/ESA/PSS%2003%20203%20Vol.1%20Structural.pdf. Last accessed: 17-03-2025.

A. Fathi. Mechanical properties of strand pet foams at different length scales. Last accessed: 06-03-2025, 2018. URL https://epub.uni-bayreuth.de/id/eprint/4286/2/190304_Dissertation_Amir%20Fathi.pdf.

Forest Trends. Timber legality risk dashboard: Peru, 2021. URL https://www.forest-trends.org/idat_countries/peru/. Last accessed: 18-02-2025.

V. Giavotto, M. Borri, P. Mantegazza, G. Ghiringhelli, V. Carmaschi, G.C. Maffioli, and F. Mussi. Anisotropic beam theory and applications. *Computers & Structures*, 16(1):403–413, 1983. ISSN 0045-7949. doi: https://doi.org/10.1016/0045-7949(83)90179-7. URL https://www.sciencedirect.com/science/article/pii/0045794983901797.

B. J. Goodno and J. M. Gere. *Mechanics of Materials*. Cengage Learning, Boston, Mass; Australia, 9. edition, si edition. edition, 2016. ISBN 9781337093354.

Grammarly Inc. How does grammarly work? URL https://support.grammarly.com/hc/en-us. Last accessed: 25-05-2025.

Gurit. Gurit wind energy handbook - 2. aerodynamics and loads, a. URL https://www.gurit.com/wind-energy/. Last accessed: 20-09-24.

Gurit. Gurit wind energy handbook - 3. structural design, b. URL https://www.gurit.com/wind-energy/. Last accessed: 20-09-24.

Gurit. Gurit wind energy handbook - 5. materials, c. URL https://www.academia.edu/30002923/WE_Handbook_5_Gurit_Composite_Materials_for_Wind_Turbine_Blades_Gurit_Materials_for_Wind_Turbine_Blades. Last accessed: 02-01-25.

Gurit. Gurit® balsaflex™ balsa wood core material, d. URL https://www.gurit.com/wp-content/uploads/bsk-pdf-manager/2022/08/balsaflex.pdf. Last accessed: 19-02-2025.

Gurit. Gurit kerdyn™ structural foam core recycled and recyclable, e. URL https://www.gurit.com/wp-content/uploads/bsk-pdf-manager/2024/06/PDS-Kerdyn-14-0524.pdf. Last accessed: 19-02-2025.

Gurit. Product overview: Core materials, f. URL https://www.gurit.com/wp-content/uploads/2024/04/Core-brochure_v21_web.pdf. Last accessed: 20-02-2025.

Gurit. Official website, g. URL https://www.gurit.com/. Last accessed: 20-02-2025.

Gurit. Guide to composites, h. URL https://www.gurit.com/wp-content/uploads/2022/12/guide-to-composites-1.pdf. Last accessed: 19-02-2025.

M. O. L. Hansen. *Aerodynamics of Wind Turbines*. James & James, 35-37 Williams Road, London NW1 3ER, UK, 2000. ISBN 1902916069.

S. M. Hermansen, Gregor Borstnar, and T. Buhl. Github repo: GuritBladeModels. https://github.com/sebhermansen/GuritBladeModels, 2024.

S. M. Hermansen, G. Borstnar, T. Buhl, and E. Lund. The g98m: A detailed open-source modern offshore wind turbine blade structural model with optimization applications, 2025. ISSN 1615-1488. URL https://doi.org/10.1007/s00158-025-04025-8. Last accessed: 11-05-2025.

IRT Jules Verne. Irt jules verne launches 'zebra project' to develop 100% recyclable composite wind turbine blades with industrial partners, 2020a. URL https://shorturl.at/NVWxR. Last accessed: 18-02-2025.

IRT Jules Verne. Zebra project achieves key milestone with production of the first prototype of its recyclable wind turbine blade, 2022b. URL https://shorturl.at/FeqEh. Last accessed: 18-02-2025.

IRT Jules Verne. Zebra consortium unveils second recyclable wind turbine blade, advances sustainability in wind energy, 2023c. URL https://shorturl.at/IJaWo. Last accessed: 18-02-2025.

A. Jensen. Siemens gamesa's danish blade plant celebrates 20-year anniversary, July 2022. URL bit.ly/4mzW3AH. Last accessed: 28-05-2025.

R. M. Jones. *Mechanics of composite materials*. Taylor & Francis, Philadelphia, Pennsylvania, second edition. edition, 1999. ISBN 1-4987-1106-5.

R. M. Jones. *Buckling of Bars, Plates, and Shells*. Bull Ridge Publishing, Blacksburg, Virginia, 2006. ISBN 978-0-9787223-0-2.

T. Kettner. Stability analysis of wind turbine blades for preliminary design. Master's thesis, Hamburg University of Technology, 2020.

R. P. Ley, W. Lin, and U. Mbanefo. Facesheet wrinkling in sandwich structures. Technical report, NASA, 1999. URL https://ntrs.nasa.gov/citations/19990017863. Last accessed: 17-03-2025.

E. Lindgaard. Analysis and design optimization of laminated composite structures, May 2024. PhD course at Aalborg University. Notes on buckling analysis and design optimization of composite structures.

E. Lindgaard and E. Lund. Nonlinear buckling optimization of composite structures. *Computer methods in applied mechanics and engineering*, 199(37):2319–2330, 2010. ISSN 0045-7825.

E. Lindgaard and E. Lund. A unified approach to nonlinear buckling optimization of composite structures. *Computers & structures*, 89(3):357–370, 2011a. ISSN 0045-7949.

E. Lindgaard and E. Lund. Optimization formulations for the maximum nonlinear buckling load of composite structures. 2011b. ISSN 1615147X.

E. Lindgaard, E. Lund, and K. Rasmussen. Nonlinear buckling optimization of composite structures considering "worst" shape imperfections. *International journal of solids and structures*, 47(22): 3186–3202, 2010. ISSN 0020-7683.

LM Wind Power. From a plastic bottle to a wind turbine blade, April 2021. URL https://www.lmwindpower.com/en/stories-and-press/stories/sustainability/from-a-plastic-bottle-to-a-wind-turbine-blade. Last accessed: 18-02-2025.

E. Lund, J. Jakobsen, and J. Kepler. Mechanics of composite materials and structures, 2024. Course material for the Mechanics of Composite Materials and Structures course for DMS2 at Aalborg University.

S. Midgley, M. Blyth, N. Howcroft, D. Midgley, and A. Brown. Balsa: biology, production and economics in papua new guinea. Technical report, Australian Centre for International Agricultural Research, 2010. URL https://www.aciar.gov.au/publication/technical-publications/balsa-biology-production-and-economics-papua-new-guinea. Last accessed: 18-02-2025.

C. Mittelstedt. *Theory of Plates and Shells*. Springer Berlin Heidelberg, Berlin, Heidelberg, 1st ed. 2023. edition, 2023. ISBN 9783662668054.

K. Niu and R. Talreja. Modeling of wrinkling in sandwich panels under compression. *Journal of engineering mechanics*, 125(8):875–883, 1999. ISSN 0733-9399.

L. C. T. Overgaard and E. Lund. Structural collapse of a wind turbine blade. part b: Progressive interlaminar failure models. *Composites. Part A, Applied science and manufacturing*, 41(2):271–283, 2010. ISSN 1359-835X.

L. C. T. Overgaard, E. Lund, and P. P. Camanho. A methodology for the structural analysis of composite wind turbine blades under geometric and material induced instabilities. *Computers & structures*, 88(19):1092–1109, 2010a. ISSN 0045-7949.

L. C. T. Overgaard, E. Lund, and O. T. Thomsen. Structural collapse of a wind turbine blade. part a: Static test and equivalent single layered models. *Composites. Part A, Applied science and manufacturing*, 41(2):257–270, 2010b. ISSN 1359-835X.

A. Puck and H. Schürmann. Failure analysis of frp laminates by means of physically based phenomenological models. *Composites Science and Technology*, 62(12):1633–1662, 2002. ISSN 0266-3538. doi: https://doi.org/10.1016/S0266-3538(01)00208-1. URL https://www.sciencedirect.com/science/article/pii/S0266353801002081.

E. Sabzalieva and A. Valentini. Chatgpt and artificial intelligence in higher education, 2023. URL https://unesdoc.unesco.org/ark:/48223/pf0000385146/PDF/385146eng.pdf.multi. Last accessed: 02-01-2025.

SANY Renewable Energy. Sany re launched the world's longest onshore wind turbine blade, 2024. URL https://en.sanyre.com.cn/html/en/Media/CompanyNews/1761958102199984130.html. Last accessed: 18-02-2025.

Siemens Gamesa Renewable Energy. Sg 14-236, a. URL https://www.siemensgamesa.com/global/en/home/products-and-services/offshore/wind-turbine-sg-14-236-dd.html. Last accessed: 18-02-2025.

Siemens Gamesa Renewable Energy. A big step towards full circularity, b. URL https://bit.ly/43dTAnT. Last accessed: 20-02-2025.

J. Singer, J. Arbocz, and T. Weller. *Buckling experiments : experimental methods in buckling of thin-walled structures.*, volume 2. John Wiley & Sons, Inc., Chichester, 2002. ISBN 9780471974505.

R. T. Sullins, G. W. Smith, and E. E. Spier. Manual for structural stability analysis of plates and shells. Technical report, NASA, 1969.

J. M. T. Thompson and G. W. Hunt. *A general theory of elastic stability*. Wiley-Interscience, London, 1973. ISBN 0471859915.

S. F. Tønnesen and M. K. Christoffersen. Non-linear buckling analysis of large composite structures. Technical report, Aalborg University, 2025.

Vestas. V236-15.0 mw™. URL `https://bit.ly/3Fie9X9`. Last accessed: 18-02-2025.

J. Vinson. Optimum design of composite honeycomb sandwich panels subjected to uniaxial compression. *AIAA Journal*, 24:1690–1696, 1986. URL `https://api.semanticscholar.org/CorpusID:119938707`.

World Bank. Strengthening forest law enforcement and governance addressing a systemic constraint to sustainable development, 2006. URL `http://documents1.worldbank.org/curated/en/330441468161667685/pdf/366380REVISED010Forest0Law01PUBLIC1.pdf`. Last accessed: 19-02-2025.

D. Zenkert. *An Introduction to Sandwich Structures*. -, 2nd edition, 2005. URL `https://www.diva-portal.org/smash/get/diva2:1366182/FULLTEXT01.pdf`. Last accessed: 20-02-2025.

A. R. Zunino, M. N., and S. T. Fenton. Gone with the wind: China's balsa wood consumption is exposing flaws in peru's forest regulations and enforcement regime. Technical report, Forest Trends, 2022. URL `https://www.forest-trends.org/publications/gone-with-the-wind-balsa/`. Last accessed: 18-02-2025.

A | Digital Appendix

The digital appendix includes the non-linear buckling analysis developed in APDL, along with the relevant `.f90` fortran source files that were created or modified from the original FPP framework provided by Professor Erik Lund. The appendix also contains the verification models and boundary condition input files described in Chapter 5, as well as the Gurit98m model in APDL code, with boundary condition files corresponding to load cases: 1, 4, 5, 6, 7, and 10. The Gurit98m boundary condition files have been modified to be compatible with the non-linear buckling analysis in APDL. Scripts developed in MATLAB and APDL for the sole purpose of visualizing results and data are not included. Further details can be found in the accompanying `README.txt` file. An overview of the digital appendix contents is shown in Figure A.1.

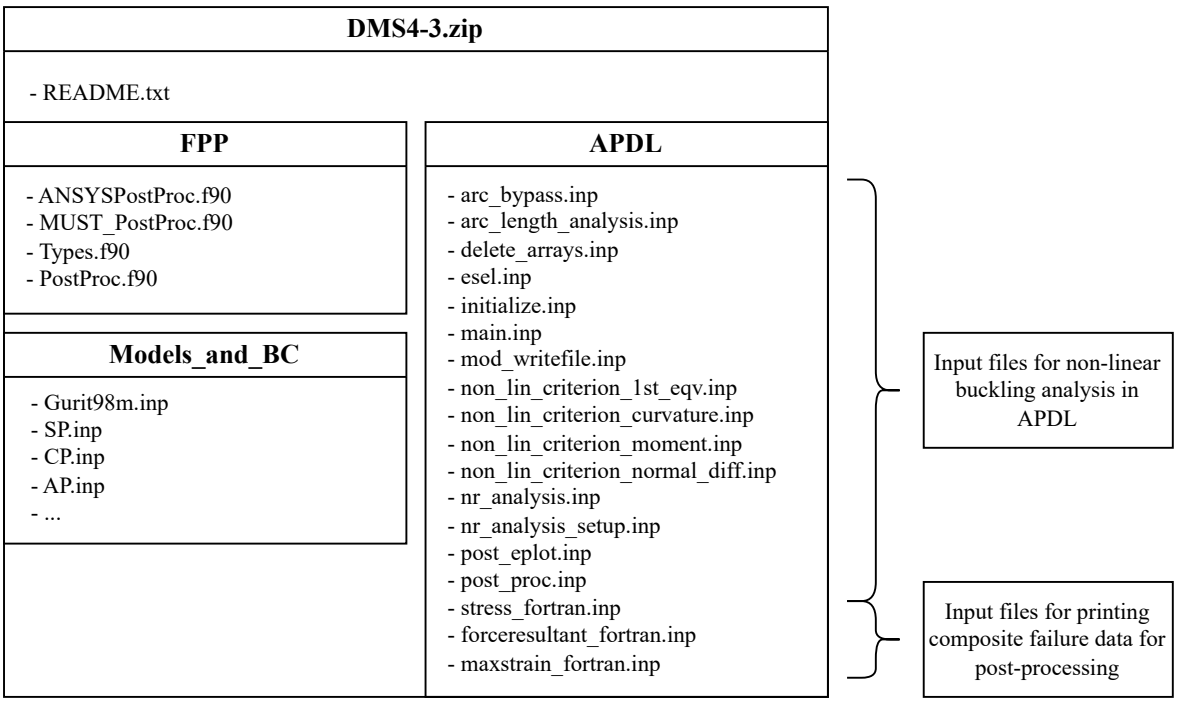

Figure A.1: Digital appendix overview.

B | Classical Sandwich Theory

As stated in Section 2.1.1, the response of sandwich structures can be analyzed using the ESL theory CST. The face sheets are assumed to be much stiffer than the core, which means that the in-plane stresses in the core are negligible [Lund et al., 2024, Prt. 9]. The face sheets are assumed to be thin compared to the core. Consequently, the faces are in plane stress, i.e., the transverse stresses are negligible. Figure B.1 illustrates the effect of the assumptions and approximations on the stress field. The example features a beam with one pinned support and one roller support at each end, subjected to a distributed load q. The face sheets and core are both isotropic and homogeneous.

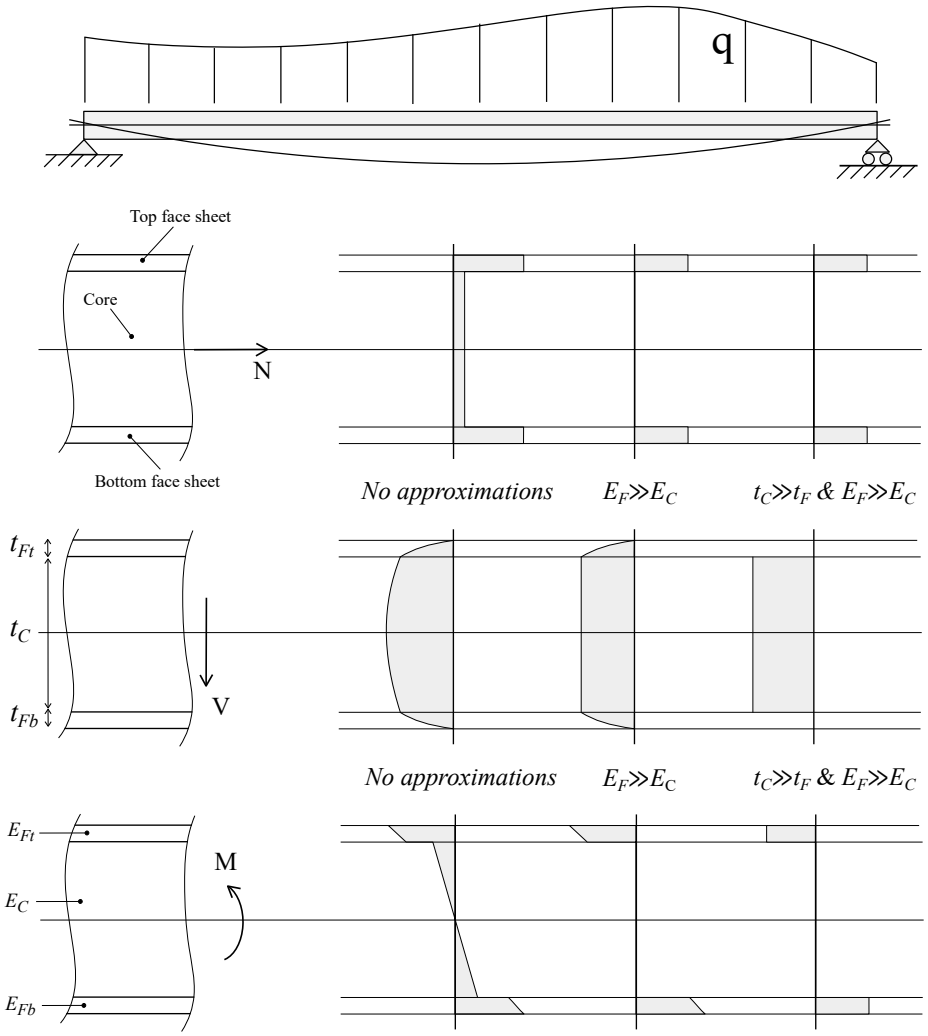

Figure B.1: Graphical representation of the simplifying approximations in classical sandwich theory. Figure is inspired by figure in [Lund et al., 2024, Prt.9 p. 48] and Figure 3.4 in [Zenkert, 2005].

C | Filter and Truncation

Depending on the specific problem and the size of the initial load step, the result may be of a small magnitude. While numerical noise typically causes slight variations, the relative change can become significant when the response is small. This may result in an erroneously significant non-linearity factor for a response that should remain linear. In this case, Numerical noise refers to unintended fluctuations caused by numerical precision or round-off errors [Tønnesen and Christoffersen, 2025]. One way to address this issue is to apply truncation to the results before calculating the non-linearity factors.

Truncation in APDL is achieved by using the modulus function: `MOD` [ANSYS, 2024b, p. 1724].

$$MOD(X,Y) = X - Y \cdot \left\lfloor \frac{X}{Y} \right\rfloor \tag{C.1}$$

Here, $\lfloor\ \rfloor$ denotes a floor function, which returns the nearest integer less than or equal to the input. Consequently, when $Y = 1$, equation (C.1) yields the decimal portion of X. This value can then be used to truncate results based on a user-defined truncation number χ_{TN}, achieved with equation (C.2) [Tønnesen and Christoffersen, 2025, p. 23].

$$X_{truncated} = X - \frac{MOD(X \cdot 10^{\chi_{TN}},1)}{10^{\chi_{TN}}} \tag{C.2}$$

Truncating results can introduce certain issues. If the magnitude of the reference result χ^{ref} is smaller than $10^{-\chi_{TN}}$, the truncation yields 0. This yields division by zero in equation (2.16). Additionally, because truncation disregards decimal values beyond the specified truncation number, minor changes in input can produce abrupt changes in output when $\chi^n \approx 10^{-\chi_{TN}}$. This is addressed by introducing a magnitude filter, where only large enough results are evaluated [Tønnesen and Christoffersen, 2025]. When the result $\chi^{ref} \leq 10^{-\chi_{TN}+1}$, the element is classified as linear, i.e., $\chi_{GNL} = 1$.

D | Puck's Action Plane Failure Criterion

Puck's action plane failure criterion distinguishes between the methods for assessing FF and IFF. FF is dominated by loading in the direction of the fibers. This means that for a UD lamina, interaction between stresses can be neglected, meaning the classical failure criteria are sufficient to asses FF [Puck and Schürmann, 2002]. Consequently, the max stress criterion is used for calculating FF with Puck's failure criteria in APDL [ANSYS, 2024e, p. 23]. Puck's criteria assume the matrix fractures like a brittle material [Puck and Schürmann, 2002]. IFF, based on a modified Mohr's fracture hypothesis for transversely isotropic materials, states that only the normal and shear stresses on the fiber fracture plane, or action plane, cause fracture [Puck and Schürmann, 2002, p. 1644]. In addition to the strength parameters seen in Figure 2.9, four additional inclination parameters are required relating to IFF [ANSYS, 2024a, Puck and Schürmann, 2002]. Puck's action plane failure criterion consists of three IFF modes with the fracture plane parallel to the fiber direction. The three IFF failure modes with associated forces are visualized in Figure D.1.

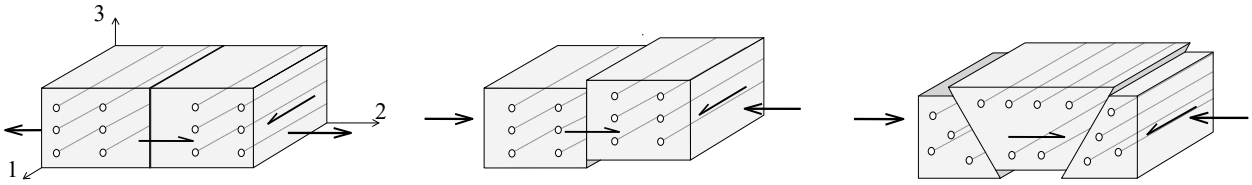

(a) Mode A *(b) Mode B* *(c) Mode C*

Figure D.1: Puck's action plane failure criterion's three IFF failure modes on a lamina under in-plane loading. Figure inspired by [ANSYS, 2024e, p. 400].

Modes A and B feature a fracture plane perpendicular to σ_2, related to the coordinate system in D.1a. Mode A is caused by tensile and/or shear stress acting in the fracture plane. The fracture surfaces tend to separate from each other, as the normal stress σ_2 lies perpendicular to the fracture plane, and the load is transferred to the adjacent material in the vicinity of the crack [Puck and Schürmann, 2002]. In mode B, a shear-dominated failure occurs, together with an associated compressive load as seen in Figure D.1b. An inclined fracture plane is observed in mode C, i.e., $\theta_{FP} \neq 0$. This is caused by the combined shear and normal stresses acting on the fracture plane [Puck and Schürmann, 2002, p. 1640]. For pure compression, the fracture plane angle was found to be $|\theta_{FP}| \approx 53° \pm 3°$. For relatively thick laminates with large fracture plane angles of at least $\theta_{FP} \approx \pm 35°$ to $\pm 45°$, forces acting in the thickness direction cause a wedge effect, which may lead to laminate delamination [Puck and Schürmann, 2002, p. 1641]. Puck's action plane failure envelope can be seen in Figure D.2.

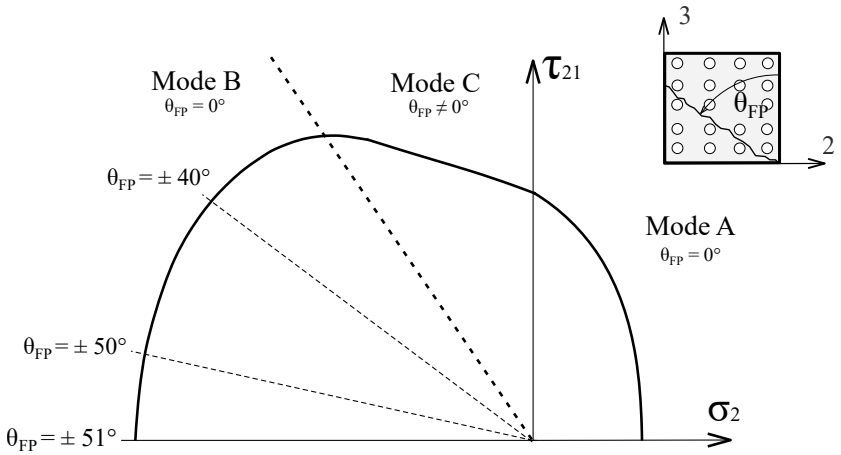

Figure D.2: Puck's action plane failure envelope for IFF, inspired by Figure 5.6 in [ANSYS, 2024e, p. 400].

E | Verification Figures

Failure indices distribution for the SP model for face sheet wrinkling and shear crimping are presented in the following Figures.

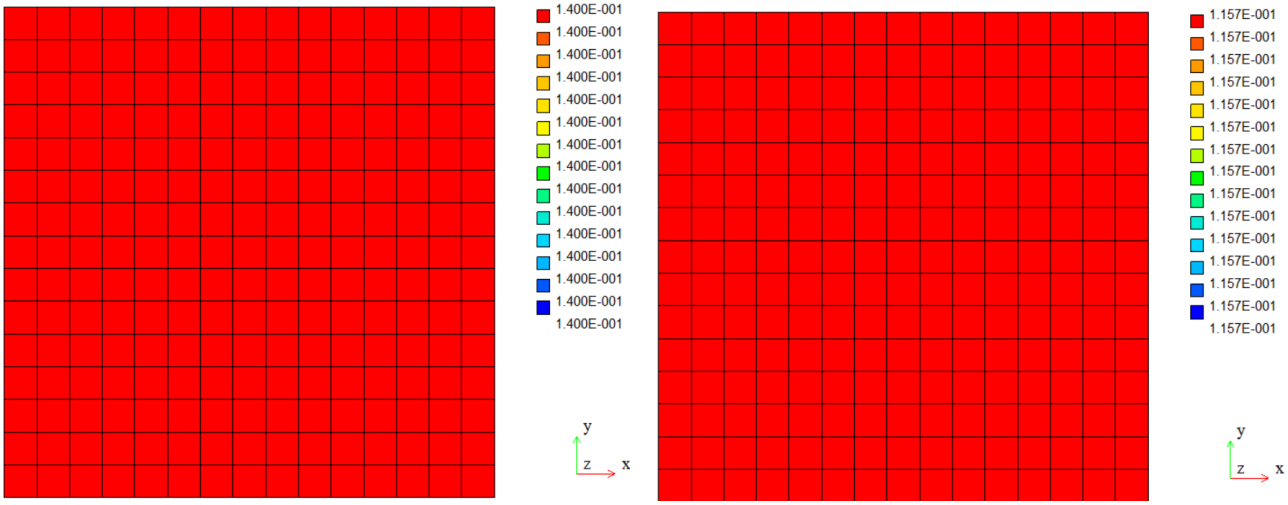

(a) Face sheet wrinkling. *(b) Shear crimping.*

Figure E.1: Face sheet wrinkling and shear crimping failure indices for SP subjected to uniaxial compression

F | Investigation of Cross Ply Discrepancies

This chapter investigates the discrepancies observed in the failure indices calculated by ACP and FPP in the analysis of the cross ply under biaxial loading.

The difference in distribution of shear crimping between ACP and FPP is investigated. The force resultants calculated with a middle offset for the center element are presented in Table F.1.

	N_x	N_y	N_{xy}	M_x	M_y	M_{xy}	Q_x	Q_y
ACP	-100.00	-100.00	$-1.3859 \cdot 10^{-9}$	0.0000	$-7.8160 \cdot 10^{-14}$	$4.1359 \cdot 10^{-25}$	0.000	0.000
FPP	-100.00	-100.00	$-1.6411 \cdot 10^{-14}$	-	-	-	-	-

Table F.1: Force resultants extracted from ACP and FPP. The "-" indicates these force resultants are not extracted from APDL.

Determining the principal orientation with equation (4.3), will yield $\theta_p = 45°$ if $N_{xy} \neq 0$. Determining the orientation of the $\xi\eta$-coordinate system using the procedure described in Section 4.1 produces $\theta_p = 0°$ because $N_x = N_y$ and $|N_{xy}| < 10^{-8}$. Overwriting the procedure and manually setting $\theta_p = 45°$ in FPP results in $f_{sc} = 0.2222$. This equates to the lowest IRF in Figure 5.7a.

The discrepancy in face sheet wrinkling is investigated by comparing the stress through the thickness, principal stresses, and constitutive modeling relating to face sheet wrinkling. The stress through the thickness is verified by comparing ACP and FPP to the analytical solution in MATLAB. The stress is extracted from ACP using the *Sampling Points* tool. The stress calculated by ACP, FPP, and MATLAB is plotted in Figure F.1. The stress is also tabulated in Table F.2 to present the stress more accurately.

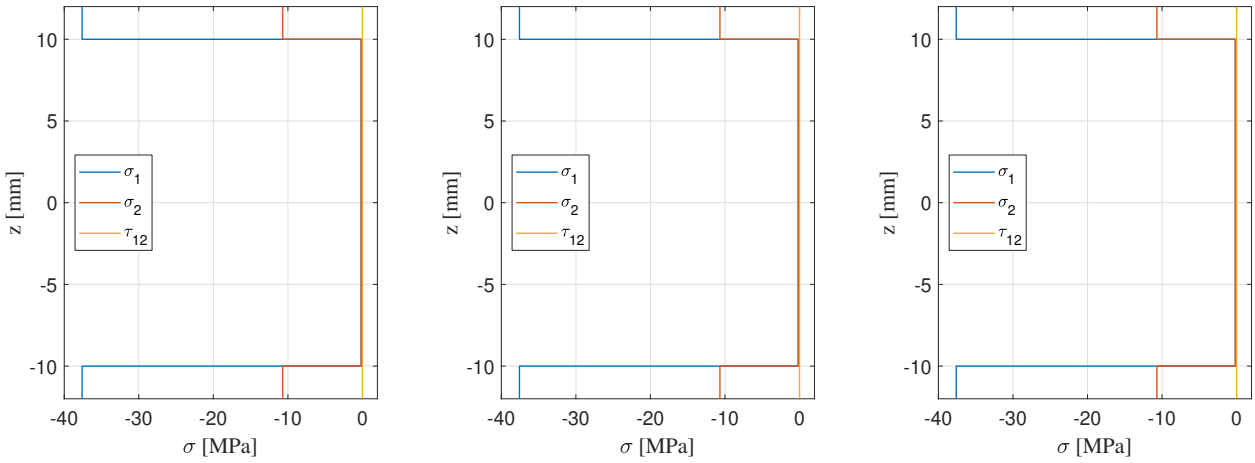

(a) In-plane stress in material directions extracted from ACP, plotted through the thickness.

(b) In-plane stress in material directions extracted from FPP, plotted through the thickness.

(c) In-plane stress in material directions calculated using MATLAB, plotted through the thickness.

Figure F.1: In-plane stress in the material coordinate system of element one through the thickness.

		Top Face Sheet	**Core**	**Bottom Face Sheet**
ACP	σ_1	-37.6077	-0.17003	-37.6077
	σ_2	-10.6920	-0.17003	-10.6920
	τ_{12}	$\pm 3.10296 \cdot 10^{-14}$	$-3.10296 \cdot 10^{-16}$	$\pm 3.10296 \cdot 10^{-14}$
FPP	σ_1	-37.6077	-0.17003	-37.6077
	σ_2	-10.6920	-0.17003	-10.6920
	τ_{12}	$\pm 1.09697 \cdot 10^{-15}$	$9.53891 \cdot 10^{-18}$	$\pm 1.09697 \cdot 10^{-15}$
MATLAB	σ_1	-37.6077	-0.17003	-37.6077
	σ_2	-10.6920	-0.17003	-10.6920
	τ_{12}	0.00000	0.00000	0.00000

Table F.2: Layer stress components σ_1, σ_2, and τ_{12} at the top position of the top face sheet, core, and bottom face sheet from ACP, FPP, and MATLAB. Only one position in each ply group is tabulated because the stress components are constants through the thickness of each ply group. Extracted for the center element. The $\pm$ indicates that the shear stress for the 0° layers is negative, while the stress for the 90° layers is positive.

In FPP and MATLAB, the stress applied to the face sheets is calculated using equation (4.1). Intermediate stress calculations cannot be obtained in ACP, so this comparison cannot be made. The face sheet stresses calculated in FPP and MATLAB are presented in Table F.3.

The subsequent calculation involves determining the principal stress of the face sheets. The magnitude of the principal stress for each layer can be extracted in ACP with the *Sampling Points* tool. The principal stresses are tabulated in Table F.4.

A difference is observed between ACP and FPP because the stress is described with different coordinate systems. A comparison can only be made if the direction of the principal stresses is known.

	FPP			MATLAB		
	σ_x	σ_y	τ_{xy}	σ_x	σ_y	τ_{xy}
Ft, Fb	-24.1498	-24.1498	0.00000	-24.1498	-24.1498	0.00000

Table F.3: In-plane stress components σ_x, σ_y, and τ_{xy} in top and bottom face sheets (Ft, Fb) from FPP and MATLAB.

	ACP		FPP		MATLAB	
	σ_{1p}	σ_{2p}	σ_{1p}	σ_{2p}	σ_{1p}	σ_{2p}
Ft, Fb	-10.6920	-37.6077	-24.1498	-24.1498	-24.1498	-24.1498

Table F.4: Comparison of principal stresses σ_{1p} and σ_{2p} in the top and bottom face sheets (Ft, Fb) from ACP, FPP, and MATLAB. The stress in ACP is based on $\{\sigma_{123}\}$, whereas FPP and MATLAB are based on $\{\sigma_{xyz}\}$.

The principal stress orientation is visualized using the Vector Principal Stress tool in Figure F.2.

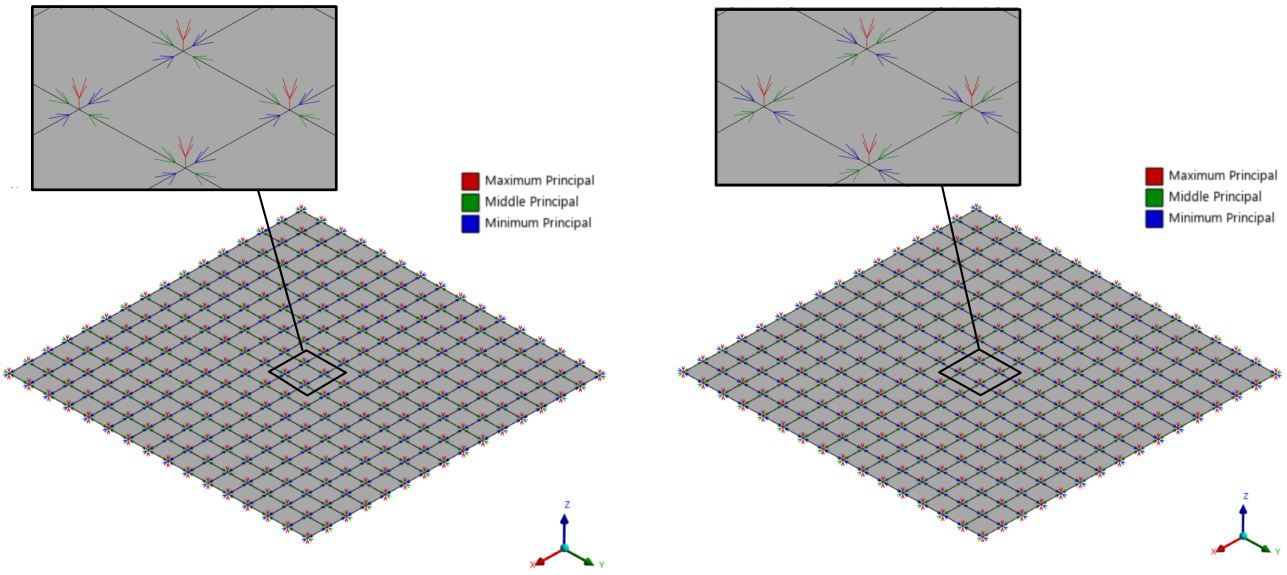

(a) Layer 1 *(b) Layer 2*

Figure F.2: Principal directions for CP in layer one and layer two for LC 2.

The principal orientation is observed along the global X and Y-directions, which coincide with the element coordinate systems for the verification analyses. Describing the principal stresses in the element coordinate system and averaging with the number of layers gives $\sigma_{1p}^{avg} = (-37.6076 \cdot 2 - 10.6920 \cdot 2)/4 = -24.1498$. Consequently, identical stress results are calculated in ACP, FPP, and MATLAB. The $\xi\eta$-system coincides with the element coordinate system for a biaxial load case, as is evident from equation (4.3). Consequently, $\theta_{\xi 1}$ calculated in FPP and MATLAB is 0° for layers one and four together with the core and 90° for layers two and three. The engineering constants in the $\xi\eta$-coordinate system are compared between ACP and FPP by modeling only the face sheet in ACP and extracting the laminate engineering constants. These are identical, as presented in Table F.5.

	$E_{F,\xi}$	$E_{F,\eta}$	$\nu_{F,\xi\eta}$	$\nu_{F,\eta\xi}$	$G_{C,\xi\zeta}$	$G_{C,\eta\zeta}$
FPP	23669.3	23669.3	0.1072	0.1072	39	36
ACP	23669.3	23669.3	0.1072	0.1072	-	-

Table F.5: Laminate engineering constants in $\xi\eta$-coordinate system from FPP and ACP. The subscripts F and C refer to face sheet and core respectively.

An alternative approach for determining face sheet stresses, in contrast to averaging the lamina face sheet stresses as described in Chapter 4, is: "*IRF (Inverse Reserve Factor) calculation is based on the worse value of all integration points, to show the most conservative case*" [ANSYS, a]. This quote was given in connection with lesson four in the *Analyzing Layered Composites Using Ansys ACP* course. A new analysis is carried out to see if the integration points within each element exhibit varying stress values, as this may explain the discrepancies in failure indices, particularly the intermediate value for face sheet wrinkling and shear crimping.

The stresses at the integration point can be retrieved in APDL by specifying "`ERESX,NO`". The `ERESX` command specifies the extrapolation of integration point results, where `NO` defines the nodal values by copying the results from the integration points [ANSYS, 2024b, p. 658]. To ensure the nodal values are only gathered from the integration point for the element of interest, the element is selected with the `ESEL` command before retrieving its nodal values. This process is repeated for all layers for the given element. The center element's nodal/integration point stresses are shown in Table F.6. The stresses are consistent for all elements through the sandwich plate. Moreover, the same stress values are observed for all face sheet laminae in the material coordinate system. Therefore, only layers one and five are presented for the center element.

		Layer 1	**layer 5 (Core)**
Averaged (FPP)	σ_1	-37.6077	-0.17003
	σ_2	-10.6920	-0.17003
	τ_{12}	$\pm 4.7430 \cdot 10^{-15}$	$4.6323 \cdot 10^{-17}$
Integration point	σ_1	-37.6077	-0.17003
	σ_2	-10.6920	-0.17003
	τ_{12}	$\pm 4.7430 \cdot 10^{-15}$	$4.6323 \cdot 10^{-17}$

Table F.6: Stress components σ_1, σ_2, and τ_{12} at the top position of the top face sheet and core for the center element, from the integration points and the averaged element centroidal values. All values are in the same order of magnitude. The $\pm$ indicates that the shear stress for the $0°$ layers is positive, while the stress for the $90°$ layers is negative.

The term "worse value" is ambiguous; however, if the failure index is calculated directly from the stress state of an integration point, different results are obtained. The stress state would correspond to the stress presented in Figure F.1 and Table F.2, this results in the principal stresses extracted from ACP in Table F.4. Through the thickness, the direction of maximum compression is $\{\theta_{\xi 1}\} = \{0°, 90°, 90°, 0°\}$. Consequently, the elastic constants are shown in Table F.5. With this assumption, the failure index is $f_w = 0.1597$, which is still different from ACP's result of $IRF_w = 0.1711$.

G | Parametric Study Figures

G.1 Parametric Study: t_C

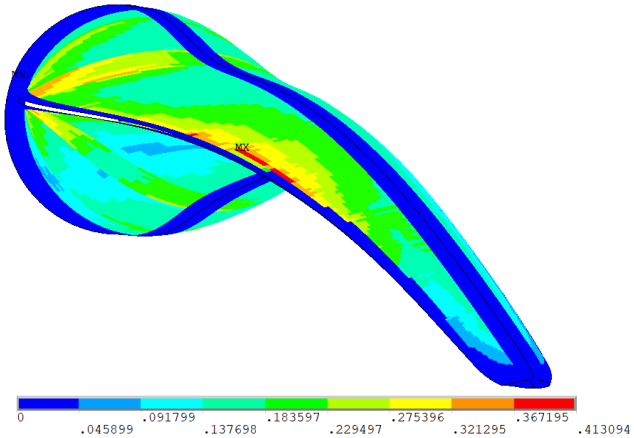

(a) Envelope plot for face sheet wrinkling with $t_C = -20\%$.

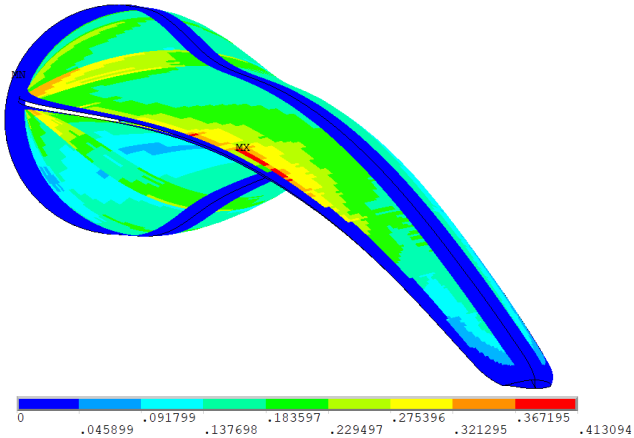

(b) Envelope plot for face sheet wrinkling with $t_C = +20\%$.

Figure G.1: Envelope plot for face sheet wrinkling for varying core failure. Underformed structure. Only SHELL181 elements are plotted.

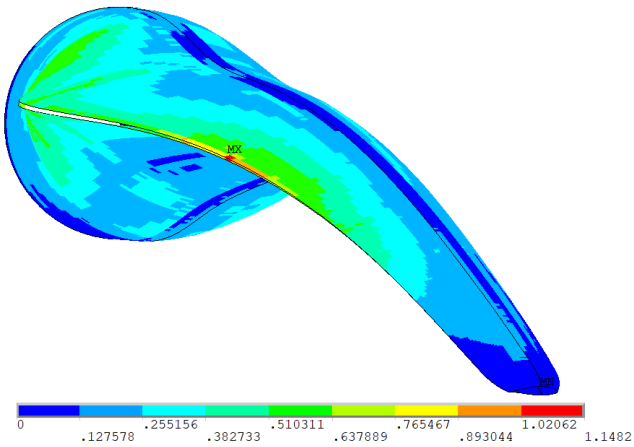

(a) Envelope plot for maximum strain with $t_C = -20\%$.

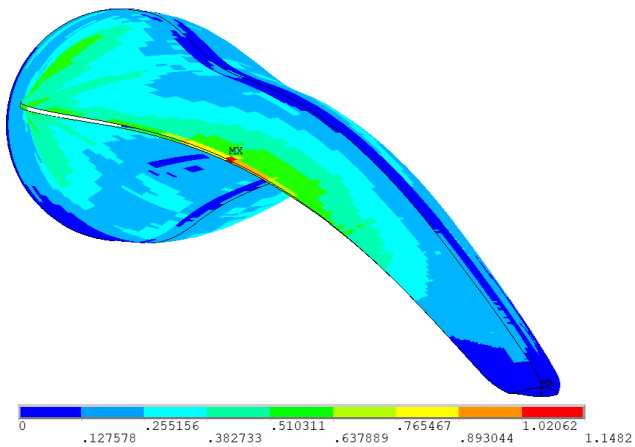

(b) Envelope plot for maximum strain with $t_C = +20\%$.

Figure G.2: Envelope plot for maximum strain for varying core failure. Underformed structure. Only SHELL181 elements are plotted.

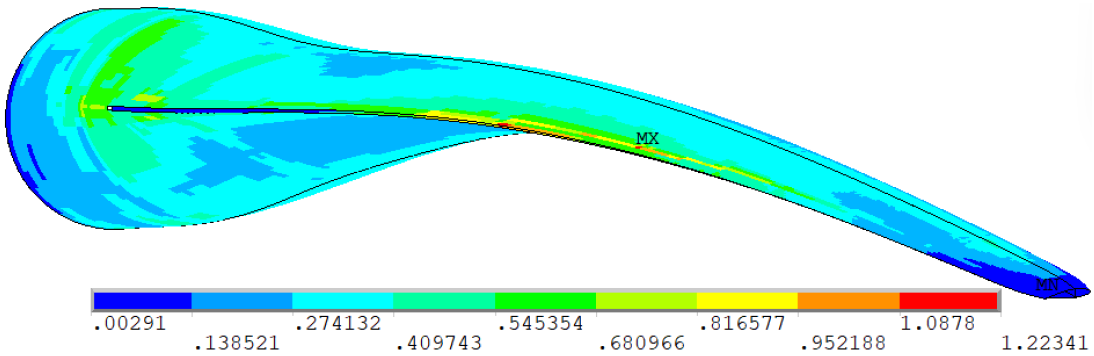

(a) t_C Envelope plot: −10%.

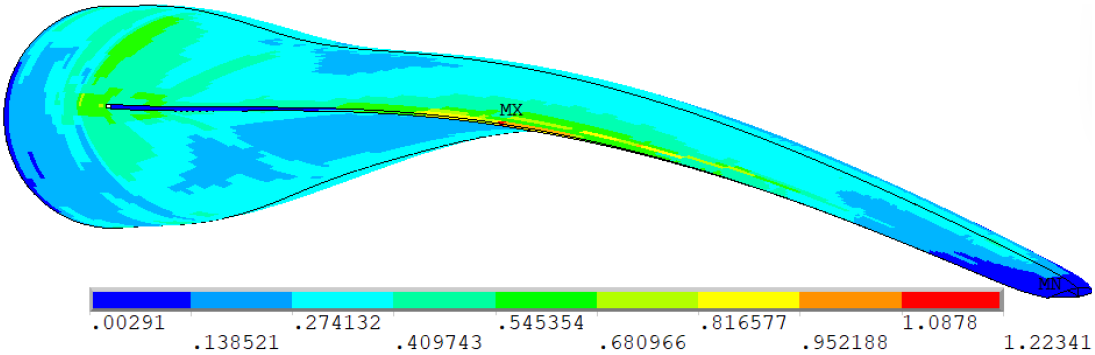

(b) t_C Envelope plot: +10%.

Figure G.3: Envelope plot for t_C analysis.

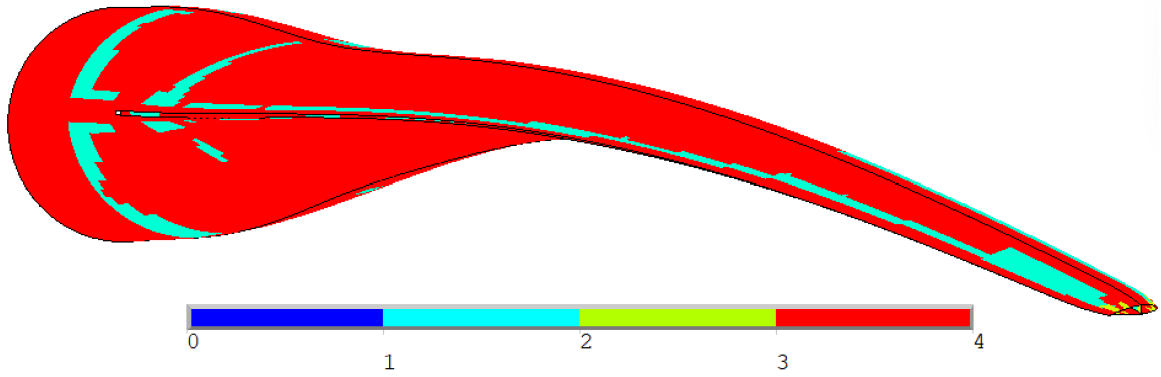

(a) t_C failure mode: −10%.

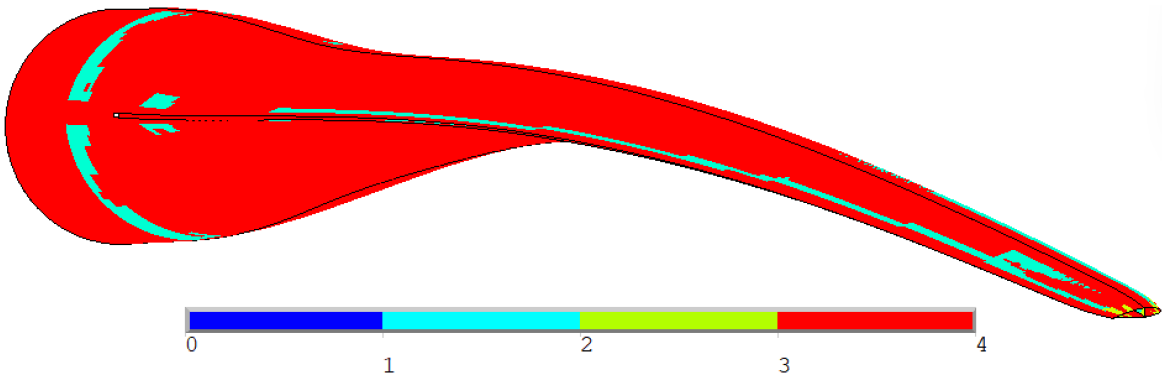

(b) t_C Failure Mode: +10%.

Figure G.4: Active failure mode for t_C analysis. 1 [Blue] = face sheet wrinkling, 2 [Turquoise] = shear crimping, 3 [Green] = core failure, 4 [Red] = max strain.

G.2 Parametric Study: G_{13}

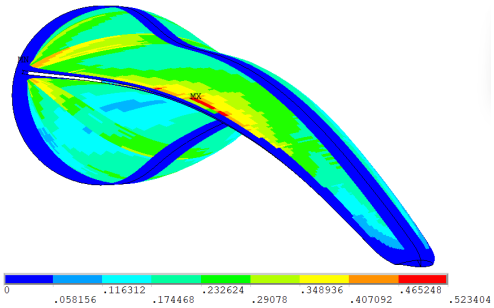

(a) Envelope plot for face sheet wrinkling with $G_{13} = -50\%$.

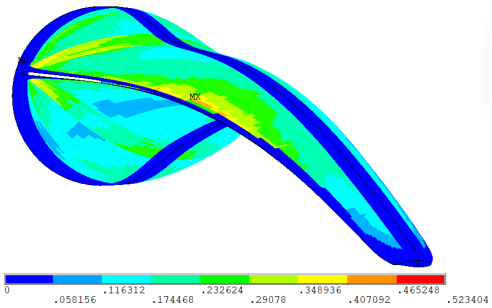

(b) Envelope plot for face sheet wrinkling with $G_{13} = -25\%$.

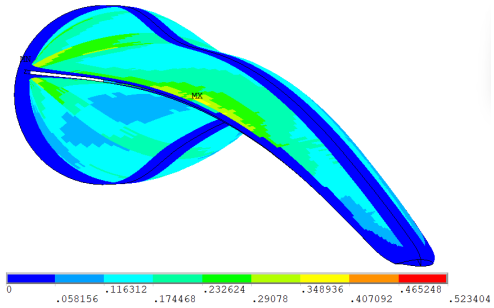

(c) Envelope plot for face sheet wrinkling with $G_{13} = +25\%$.

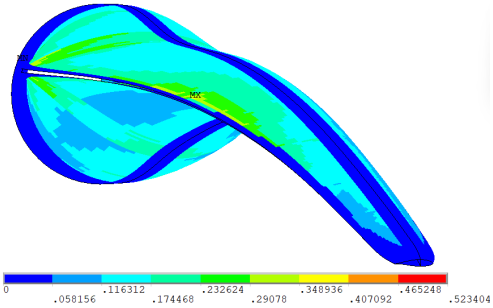

(d) Envelope plot for face sheet wrinkling with $G_{13} = +50\%$.

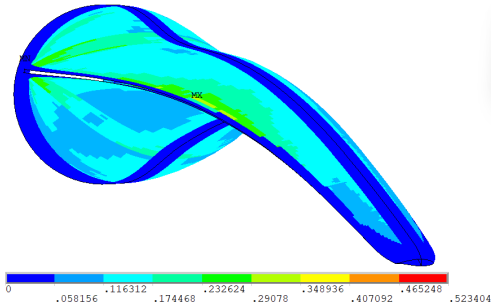

(e) Envelope plot for face sheet wrinkling with $G_{13} = +100\%$.

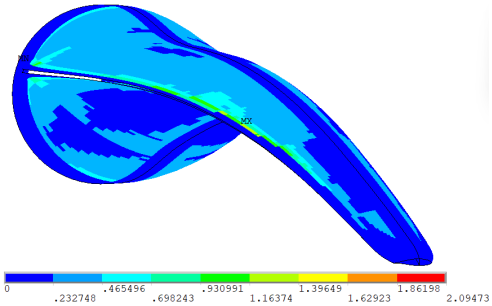

(f) Envelope plot for shear crimping with $G_{13} = -25\%$.

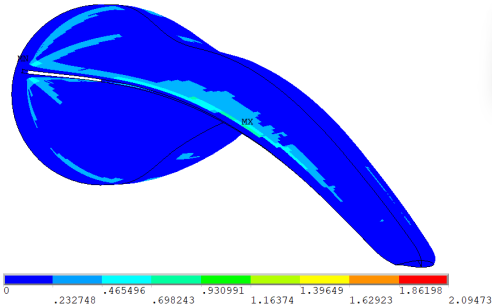

(g) Envelope plot for shear crimping with $G_{13} = +25\%$.

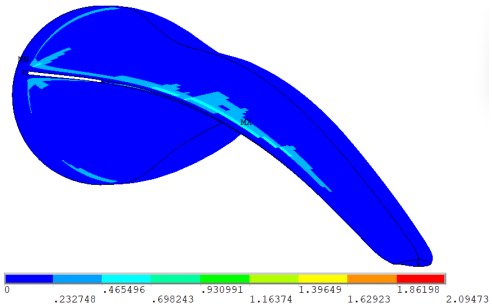

(h) Envelope plot for shear crimping with $G_{13} = +50\%$.

Figure G.5: Envelope plot for face sheet wrinkling and shear crimping. Underformed structure. Only SHELL181 elements are plotted.

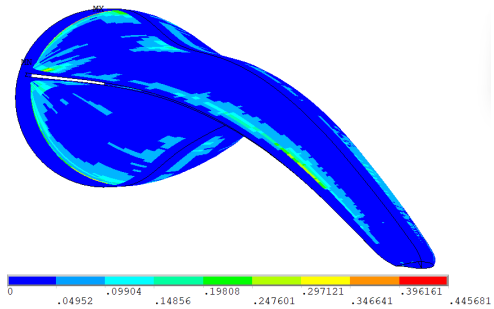

(a) Envelope plot for core failure with $G_{13} = -25\%$.

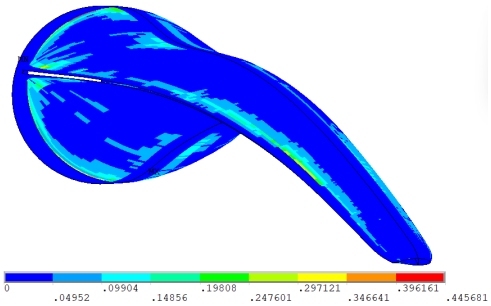

(b) Envelope plot for core failure with $G_{13} = +25\%$.

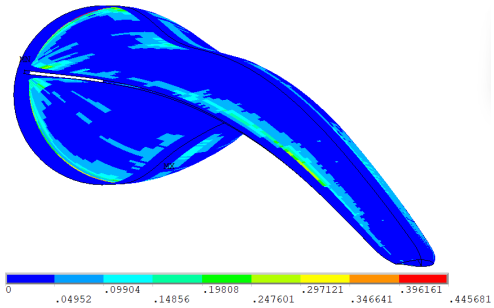

(c) Envelope plot for core failure with $G_{13} = +50\%$.

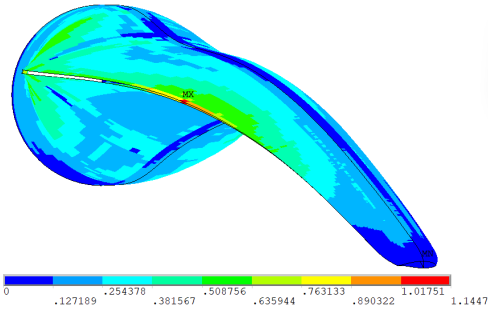

(d) Envelope plot for max strain with $G_{13} = -50\%$.

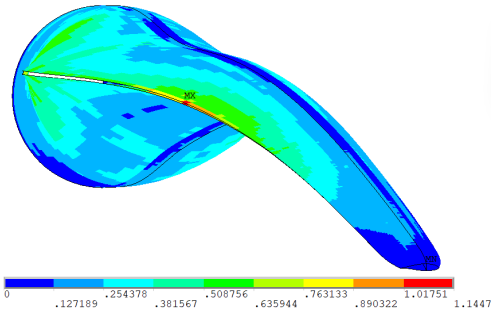

(e) Envelope plot for max strain with $G_{13} = -25\%$.

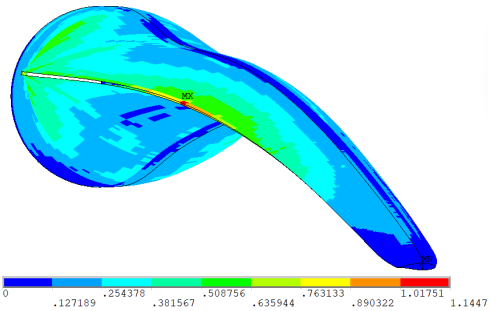

(f) Envelope plot for max strain with $G_{13} = +25\%$.

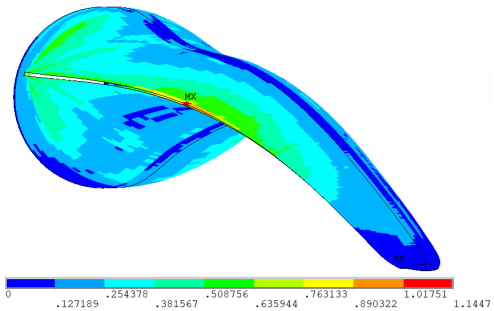

(g) Envelope plot for max strain with $G_{13} = +50\%$.

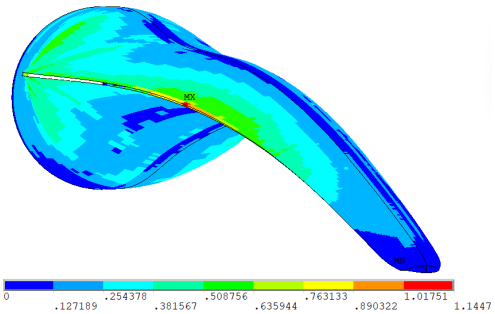

(h) Envelope plot for max strain with $G_{13} = +100\%$.

Figure G.6: Envelope plot for core failure and maximum strain. Underformed structure. Only SHELL181 elements are plotted.

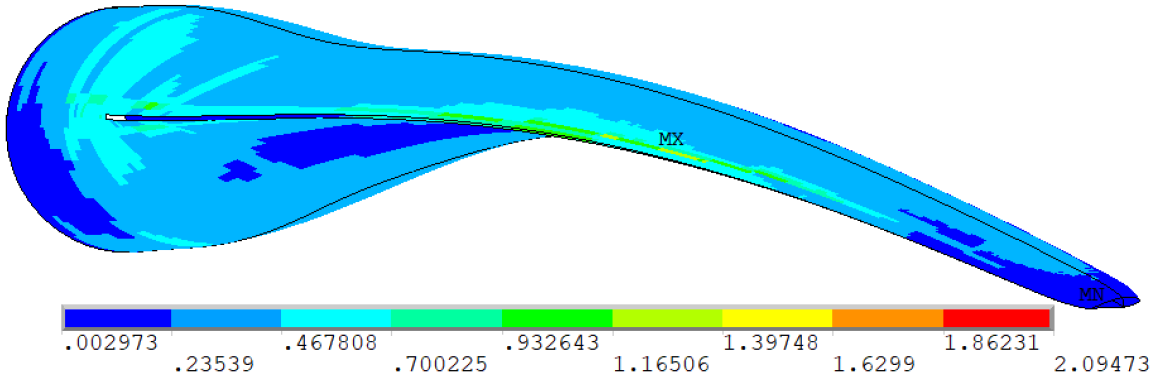

(a) G_{13} Envelope plot: −25%.

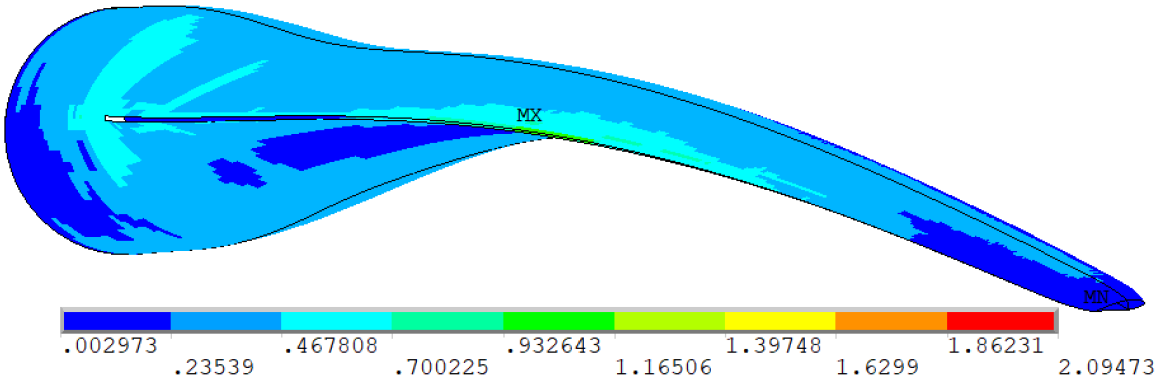

(b) G_{13} Envelope plot: +25%.

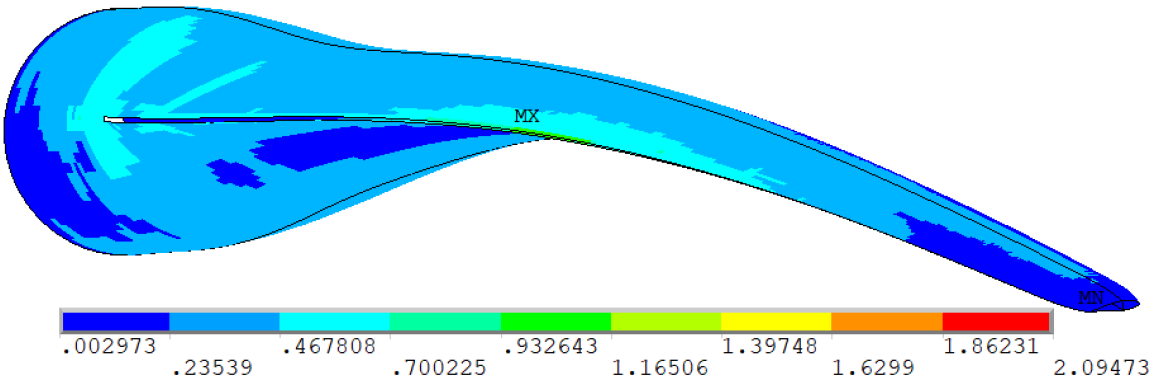

(c) G_{13} Envelope plot: +50%.

Figure G.7: Envelope plot for G_{13} analysis.

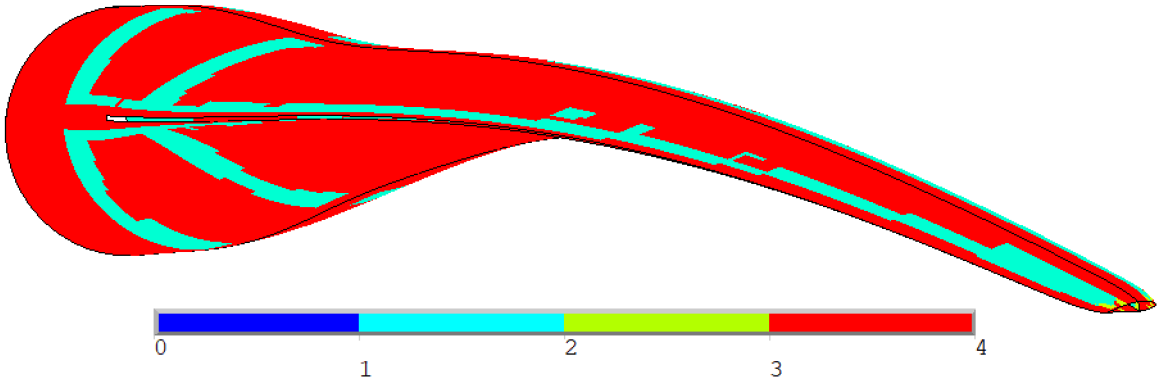

(a) G_{13} failure mode: −25%.

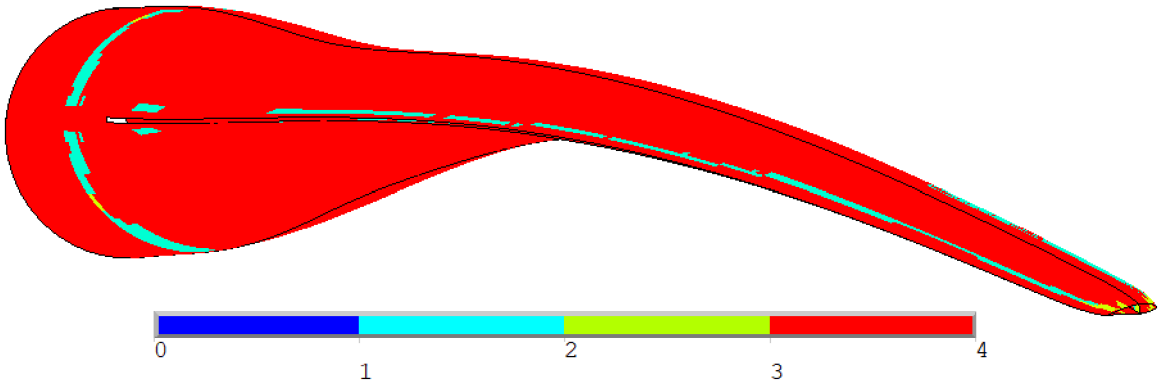

(b) G_{13} failure mode: +25%.

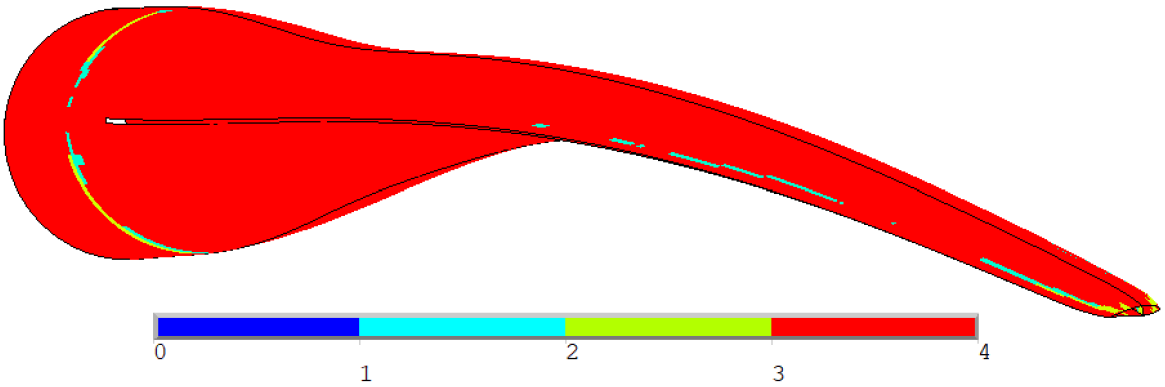

(c) G_{13} Failure Mode: +50%.

Figure G.8: Active failure mode for G_{13} analysis. 1 [Blue] = face sheet wrinkling, 2 [Turquoise] = shear crimping, 3 [Green] = core failure, 4 [Red] = max strain.

G.3 Parametric Study: G_{23}

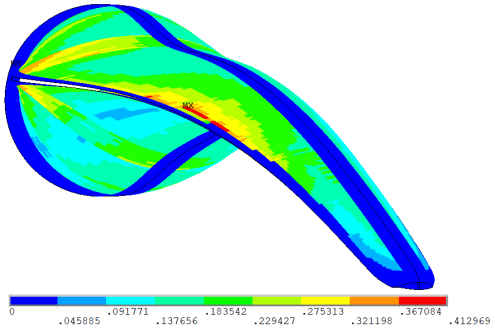

(a) Envelope plot for face sheet wrinkling with $G_{23} = -50\%$.

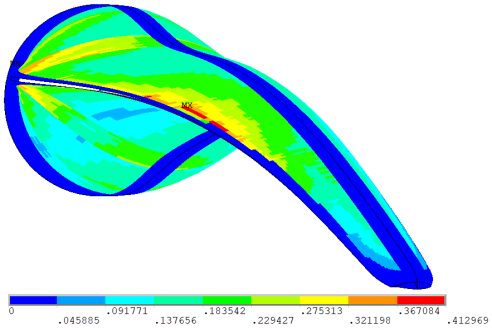

(b) Envelope plot for face sheet wrinkling with $G_{23} = -25\%$.

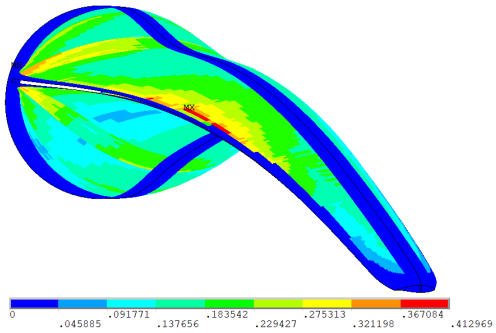

(c) Envelope plot for face sheet wrinkling with $G_{23} = +25\%$.

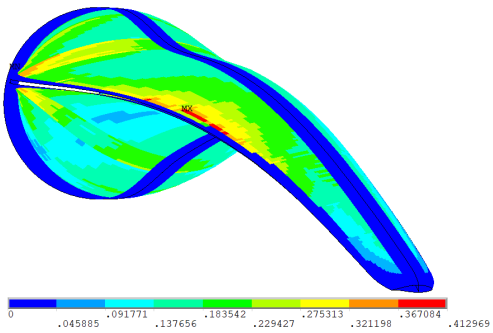

(d) Envelope plot for face sheet wrinkling with $G_{23} = +50\%$.

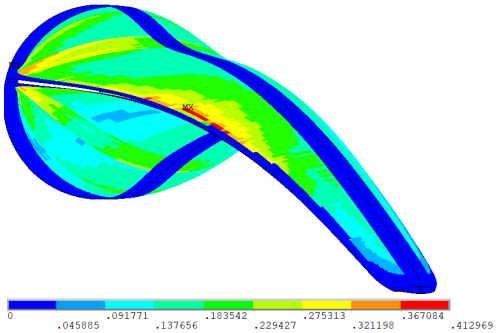

(e) Envelope plot for face sheet wrinkling with $G_{23} = +100\%$.

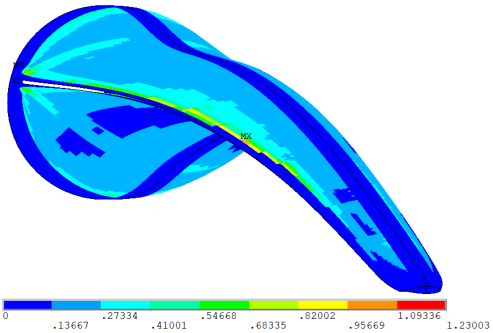

(f) Envelope plot for shear crimping with $G_{23} = -25\%$.

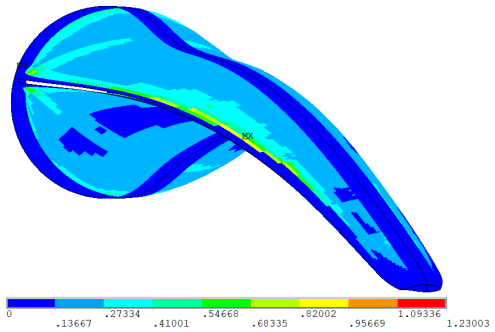

(g) Envelope plot for shear crimping with $G_{23} = +25\%$.

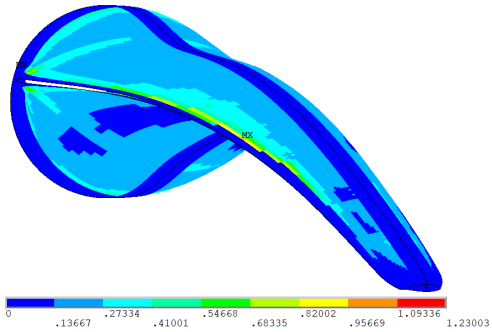

(h) Envelope plot for shear crimping with $G_{23} = +50\%$.

Figure G.9: Envelope plot for face sheet wrinkling and shear crimping. Underformed structure. Only SHELL181 elements are plotted.

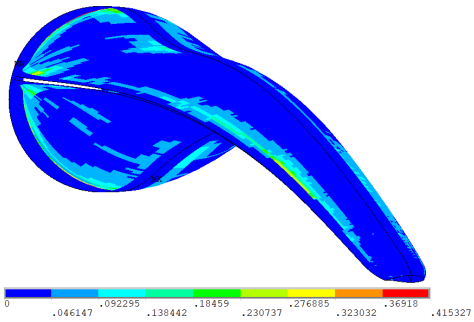

(a) Envelope plot for core failure with $G_{23} = -25\%$.

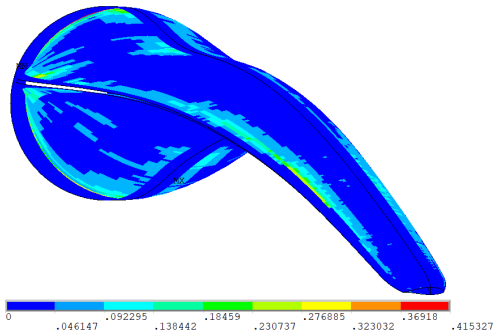

(b) Envelope plot for core failure with $G_{23} = +25\%$.

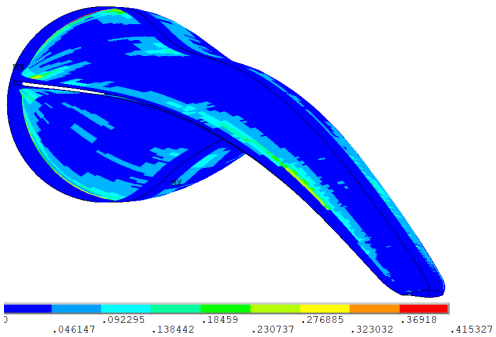

(c) Envelope plot for core failure with $G_{23} = +50\%$.

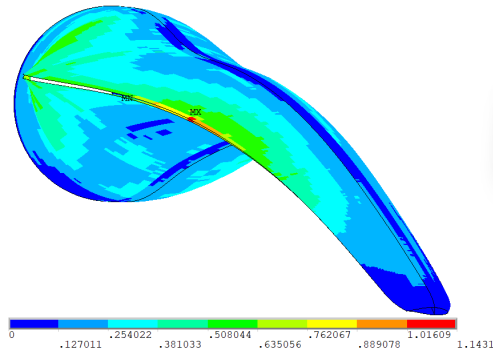

(d) Envelope plot for max strain with $G_{23} = -50\%$.

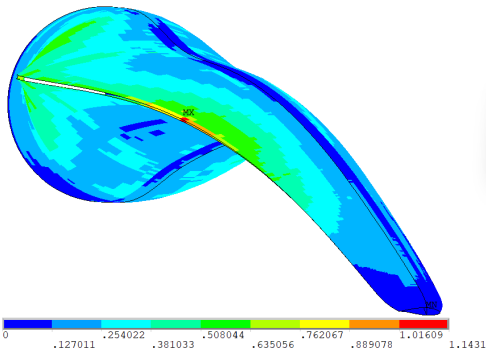

(e) Envelope plot for max strain with $G_{23} = -25\%$.

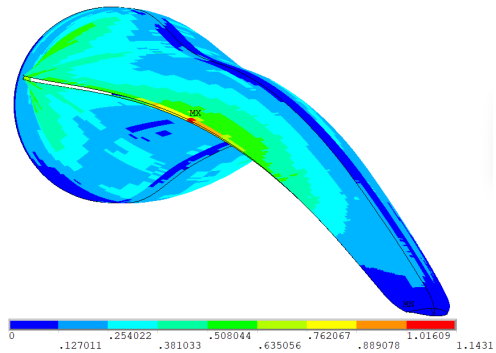

(f) Envelope plot for max strain with $G_{23} = +25\%$.

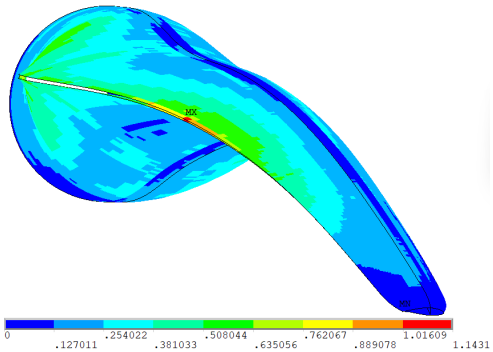

(g) Envelope plot for max strain with $G_{23} = +50\%$.

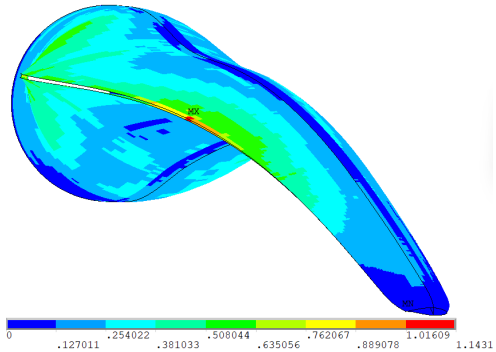

(h) Envelope plot for maximum strain with $G_{23} = +100\%$.

Figure G.10: Envelope plot for core failure and maximum strain. Underformed structure. Only SHELL181 elements are plotted.

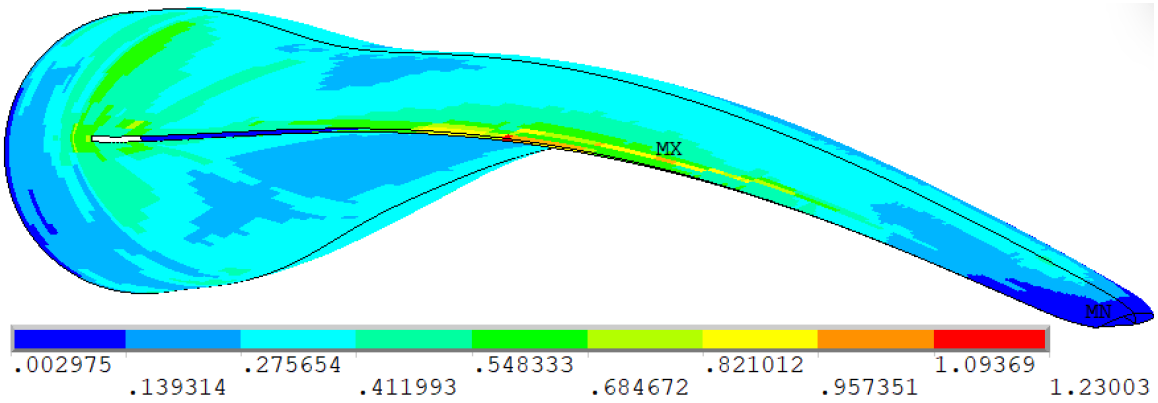

(a) G_{23} Envelope plot: −25%.

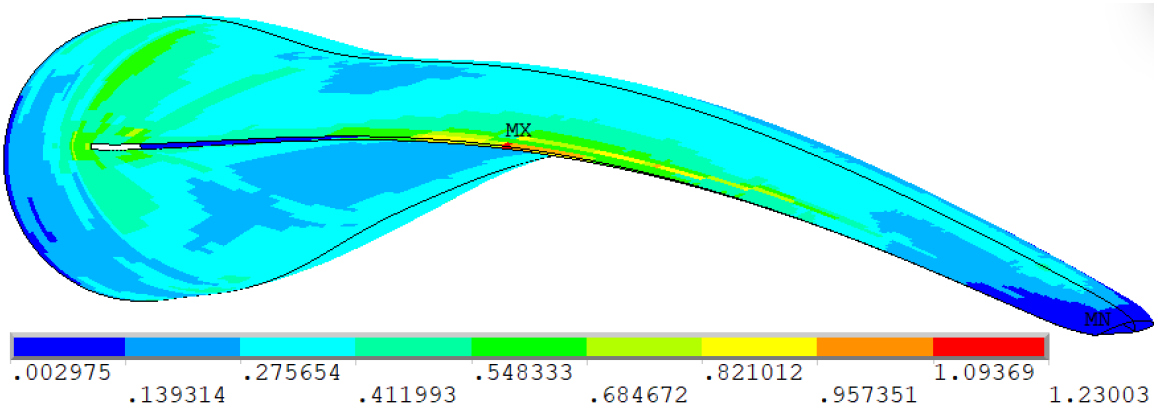

(b) G_{23} Envelope plot: +25%.

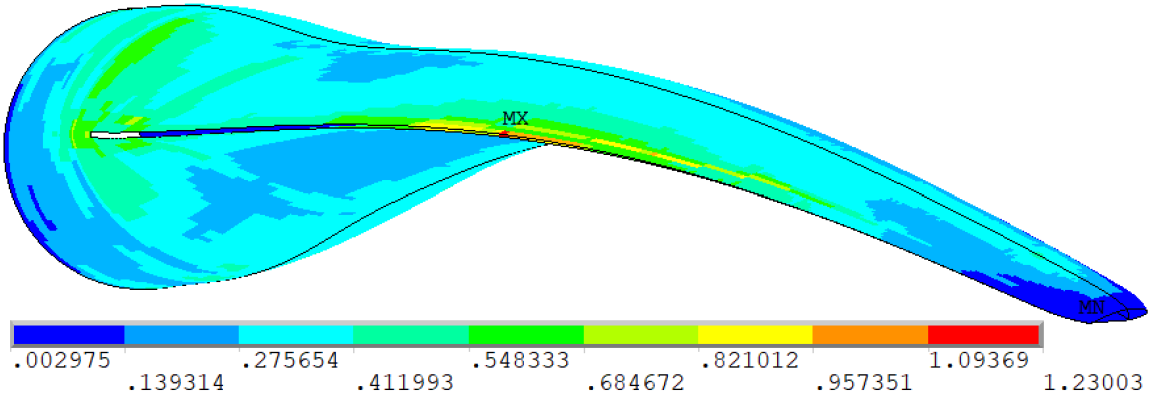

(c) G_{23} Envelope plot: +50%.

Figure G.11: Envelope plot for G_{23} analysis.

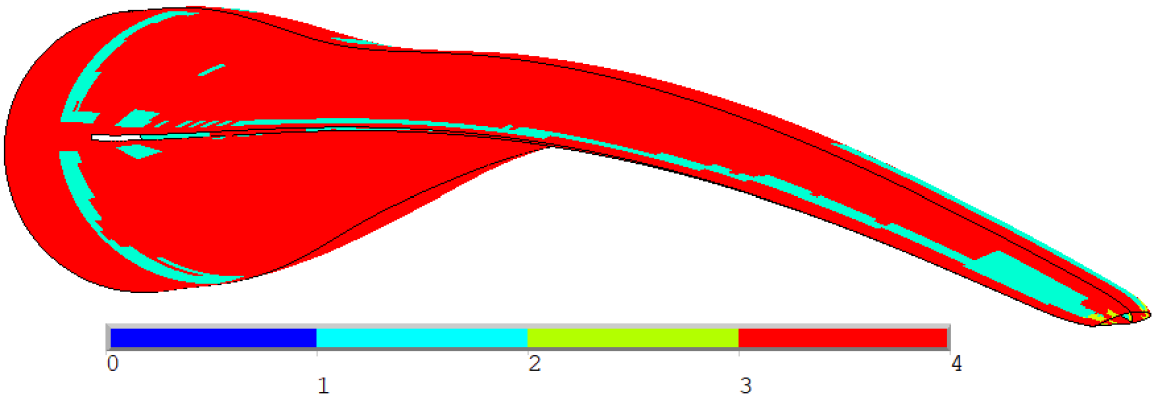

(a) G_{23} failure mode: −25%.

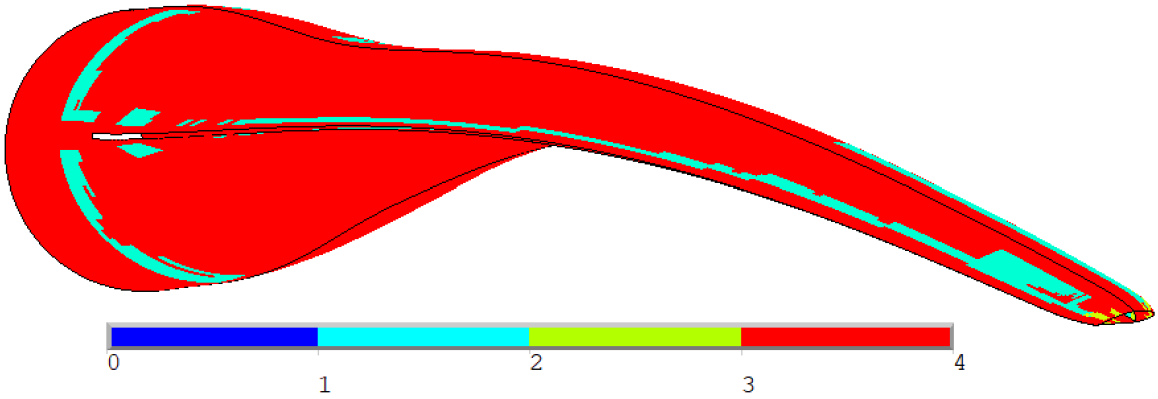

(b) G_{23} failure mode: +25%.

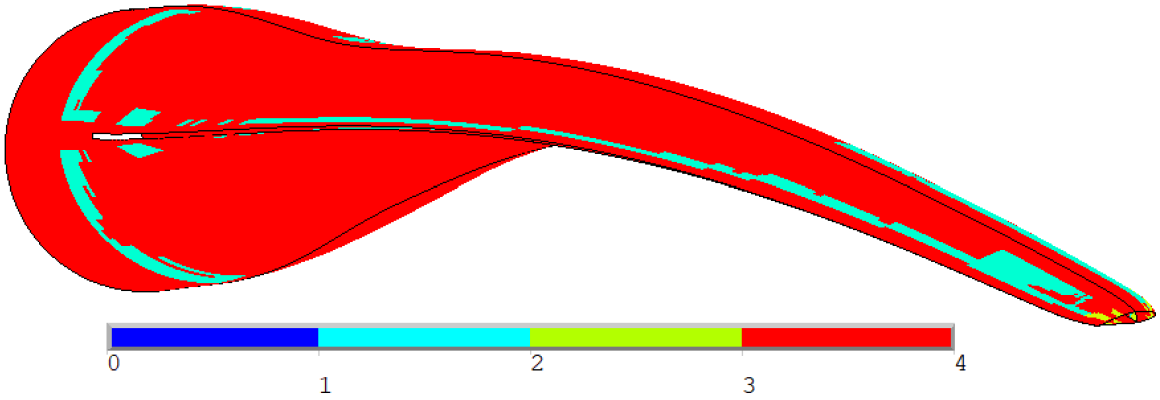

(c) G_{23} Failure Mode: +50%.

Figure G.12: Active failure mode for G_{23} analysis. 1 [Blue] = face sheet wrinkling, 2 [Turquoise] = shear crimping, 3 [Green] = core failure, 4 [Red] = max strain.